Realia et naturalia

DISSERTATIONES
PHYSICAE
UNIVERSITATIS
TARTUENSIS
84

LIIS REBANE

Measurement of the $W \to \tau\nu$ cross section and a search for a doubly charged Higgs boson decaying to τ-leptons with the CMS detector

TARTU ÜLIKOOL · UNIVERSITAS TARTUENSIS · 1632

DISSERTATIONES PHYSICAE UNIVERSITATIS TARTUENSIS
84

DISSERTATIONES PHYSICAE UNIVERSITATIS TARTUENSIS
84

LIIS REBANE

Measurement of the $W \to \tau\nu$ cross section and a search for a doubly charged Higgs boson decaying to τ-leptons with the CMS detector

UNIVERSITY OF TARTU
PRESS
1632

This study was carried out at the National Institute of Chemical Physics and Biophysics and the University of Tartu.

The Dissertation was admitted on October 19, 2012, in partial fulfillment of the requirements for the degree of Doctor of Philosophy in physics, and allowed for defense by the Council of the Institute of Physics, University of Tartu.

Supervisors: Prof. Alessandro Strumia,
National Institute of Chemical Physics and Biophysics,
Tallinn, Estonia

Prof. Martti Raidal,
University of Tartu,
Tartu, Estonia

Opponents: Dr. Oxana Smirnova,
Lund University,
Lund, Sweden

Prof. Rein-Karl Loide,
Tallinn University of Technology,
Tallinn, Estonia

Defense: December 19, 2012, University of Tartu, Estonia

ISSN 1406-0647
ISBN 978-9949-32-185-8 (print)
ISBN 978-9949-32-186-5 (pdf)

University of Tartu Press
www.tyk.ee
Order No. 570

Contents

List of Related Publications

This thesis consists of a theoretical introduction and a review of the results obtained in the three research publications [I–III] that are included at the end of the thesis, and two CMS Physics Analysis Summaries [IV-V]:

I A. Hektor, M. Kadastik, M. Müntel, M. Raidal and L.Rebane. Testing neutrino masses in little Higgs models via discovery of doubly charged Higgs at LHC. Nucl.Phys.B787:198-210 (2007). Copyright (2007), with permission from Elsevier.

II M. Kadastik, M. Raidal and L. Rebane. Direct determination of neutrino mass parameters at future colliders. Phys.RevD77:115023 (2008). Copyright (2008) by the American Physical Society.

III CMS Collaboration. A search for a doubly charged Higgs boson in pp collisions at $\sqrt{s} = 7$ TeV. EPJ C (accepted for publication). arXiv:1207.2666 [hep-ex] (2012).

IV CMS Collaboration. Obsevation of $W \to \tau\nu$ production in pp collisions at $\sqrt{s} = 7$ TeV. CMS Physics Analysis Summary EWK-11-002 (2011)

V CMS Collaboration. Measurement of the $W \to \tau\nu$ cross–section in pp collisions at $\sqrt{s} = 7$ TeV. CMS Physics Analysis Summary EWK-11-019 (2011)

Author's Contribution

In publication I, the dissertant performed the Monte Carlo simulation based analysis of the signal and background processes

In publication II, the dissertant performed the calculations and error estimation.

In publication III, the dissertant performed the analysis of the doubly charged Higgs boson decaying to τ-leptons.

Acknowledgements

First of all, I would like to thank my parents and Grandparents. Aitäh Anne ja Volli, memm ja mamma, et olete alati olemas olnud! Especial thanks to Lidia for offering her good company to Arthur during the most intense periods of thesis-writing. Finally, I want to thank my small family – thank you, Benedict and Paul-Arthur, for always being there, always cheering me up and always being an inspiration!

I thank my supervisor Alessandro Strumia for his help and I owe much gratitude to my supervisor and group leader Martti Raidal for sharing his scientific intuition, creating a good working atmosphere and always providing his guidance, help and support.

I must greatly acknowledge Mario Kadastik for convincing me to join the particle physics group at NICPB, for his patient tutoring and assistance with all the technical details that came with this decision and for continuous fruitful collaboration – thank you! I also warmly thank my good colleagues and friends: Andi Hektor, Kristjan Kannike, Ilja Livenson, Mait Müntel and Antonio Racioppi for helpful discussions and good atmosphere at work. Kristjan additionally needs recognition for language editing assistance.

Next I would like to thank my colleagues at CERN. Especial thanks to Christian Veelken for his continuous help, supervision and good collaboration. Working with him has been a wonderful experience. I have great memories of working with Souvik Das – thank you for sharing your knowledge, your office and your good mood! Next I would like to thank Abdollah Mohammadi for the fruitful collaboration and interesting discussions – it was very nice to work together! I greatly appreciate the help and guidance of Giuseppe Bagliesi, Monica Vazquez Acosta and Nicola De Filippis – thank you!

Finally I would like to thank all the people who have made the years of my Ph.D. studies special – my colleagues, professors and friends, thanks for all!

I greatly appreciate my colleagues in the CERN accelerator departments for the excellent performance of the LHC machine. I thank the technical and administrative staff at CERN and other CMS institutes. My work was financially supported by the Estonian Science Foundation, by the Estonian Government and by the FP6 of the European Union.

Chapter 1

Theoretical Foundations

Through human history scientists and philosophers have tried to develop a complete theory, that would describe all processes that occur in nature. The search for elementary constituents of matter, which would allow a high diversity of constructions to be explained by different combinations of simple building blocks, was already a concern in Ancient Greek, where Democritos introduced the concept of an *atom* (uncuttable). However, back then philosophical rather than scientific approach was used in the attempts to understand nature.

During the 17th century scientific understanding made an important step forward, as Galileo Galilei was one of the first thinkers to clearly state that the laws of nature are mathematical. During this period a proper relationship between mathematics, theoretical physics and experiments was created, setting a fundamental basis for the modern science. A rapid development followed, lead by scientists like Newton, which established scientific models for a wide variety of natural phenomena.

By the end of the 19th century the existing scientific understanding, that covered mechanics, electromagnetism and thermodynamics, was believed to be nearly complete, besides a few effects that the existing theories still failed to explain. These effects or "clouds of physics", as described by Kelvin, were the failure to explain the black body radiation by the classical thermodynamics and the failure of the Michelson-Morley experiment to detect an ether wind. Solving these problems was believed to complete physics. Instead, these "two clouds" were the starting point of the early 20th century revolution in theoretical physics from which the theory of relativity and quantum mechanics emerged.

Today our scientific understanding of the world is based on four fundamental interactions: electromagnetic, strong, and weak interaction, and gravitation. The first three have been combined to a single theory, the Standard Model of particle physics, that is extremely successful in describing elementary particles and their interactions. The Standard Model has been experimentally verified to a high level of accuracy over the past decades. However, there are theoretical motivations and experimental indications that it is not a complete theory, but needs to be extended. The ongoing investigation of the limitations of the Standard Model can lead us to new major branches of physics

and generally towards a deeper understanding of nature.

1.1 The Standard Model of Particle Physics

The Standard Model (SM) was developed throughout the twentieth century, and is accepted as the current description of elementary particle physics, describing matter and its interactions at the fundamental level. The SM is based on quantum field theory, which combines quantum mechanics with special relativity.

1.1.1 Lagrange Formulation

The principle of stationary action is one of the most fundamental concepts in physics. Given the Lagrange density $\mathcal{L}$ of a system as a function of the fields φ_i and their derivatives $\partial_\mu \varphi_i$, the action S for the evolution between two states is given by

$$S = \int \mathrm{d}t\, \mathrm{d}\mathbf{r}\, \mathcal{L}(\varphi_i(t, \mathbf{r}), \partial_\mu \varphi_i(t, \mathbf{r})). \tag{1.1}$$

Requiring the action to be minimal and applying the calculus of variation $\delta S = 0$, leads the Euler-Lagrange equations, which correspond to the equation of motion for the fields,

$$\partial_\mu \frac{\partial \mathcal{L}}{\partial(\partial_\mu \varphi_i)} - \frac{\partial \mathcal{L}}{\partial \varphi_i} = 0. \tag{1.2}$$

Common Lagrange Densities

The Lagrange density function for a free particle consists of a kinetic term and a mass term. For a spin 1/2 particle it has a form

$$\mathcal{L} = i\bar{\psi}\gamma^\mu \partial_\mu \psi - m\bar{\psi}\psi, \tag{1.3}$$

where ψ is a four-component Dirac spinor, γ^μ are Dirac's γ-matrices and $\bar{\psi} = \psi^\dagger \gamma^0$.

A free scalar particle with spin 0 is described by the Lagrange density:

$$\mathcal{L} = \frac{1}{2}(\partial_\mu \varphi)^2 - \frac{1}{2} m^2 \bar{\varphi}\varphi, \tag{1.4}$$

and a vector field A with spin 1 by:

$$\mathcal{L} = -\frac{1}{4} F^{\mu\nu} F_{\mu\nu} + \frac{1}{2} m^2 A^\mu A_\mu, \tag{1.5}$$

where $F^{\mu\nu} = \partial^\mu A^\nu - \partial^\nu A^\mu$.

1.1.2 Symmetries

The concept of symmetry has played a major role in the development of modern physics. The symmetry of the system can be global or local, depending on whether or not the respective transformation depends on the space-time coordinates. Additionally, a classical level symmetry exhibited by the Lagrangian can be broken after quantization. Such type of symmetry breaking is called an anomaly.

In the framework of quantum field theory a physical particle is described by an irreducible representation of the symmetry group. The Poincaré group is the global symmetry of any relativistic field theory. It includes the following transformations:

- Translations on space-time that form an Abelian Lie group
- 3-dimensional rotations in space that form a non-Abelian Lie group
- Boosts or transformations connecting two uniformly moving bodies

Rotations and boosts make up the Lorentz group.

The full Poincaré group transformation can be written in a form

$$x^\mu \to x^{\nu\prime} = \Lambda^\nu_\mu x^\mu + a^\nu, \tag{1.6}$$

where Λ is the Lorentz transformation and a is the space-time translation.

Elementary particles, as the representations of Poincaré group are usually specified by their four-momentum and the intrinsic quantum numbers, including spin, parity and charge conjugation.

Local Gauge Invariance

Local gauge symmetries describe the interactions between particles in the SM. In the quantum field formulation a local gauge transformation of the complex phase has a form:

$$\psi(\mathbf{x}) \to \psi'(\mathbf{x}) = e^{i\alpha(\mathbf{x})}\psi(\mathbf{x}). \tag{1.7}$$

The derivative term in the Lagrangian is, however, not invariant under such transformation:

$$\partial_\mu\psi'(\mathbf{x}) = \partial_\mu\left(e^{i\alpha(\mathbf{x})}\cdot\psi(\mathbf{x})\right) = e^{i\alpha(\mathbf{x})}i\psi(\mathbf{x})\partial_\mu\alpha(\mathbf{x}) + e^{i\alpha(\mathbf{x})}\partial_\mu\psi(\mathbf{x}) \tag{1.8}$$

The invariance can be established by replacing the derivative ∂_μ with a covariant derivative D_μ, such that

$$\partial_\mu \to D_\mu = \partial_\mu + ieA_\mu, \tag{1.9}$$

where e is a coupling constant and A_μ is a vector field that transforms as

$$A_\mu(\mathbf{x}) \to A'_\mu(\mathbf{x}) = A_\mu(\mathbf{x}) - \frac{1}{e}\partial_\mu\alpha(\mathbf{x}). \tag{1.10}$$

The introduced vector field has to be massless, as the mass term in the Lagrangian

$$\frac{1}{2}m^2 A^\mu A_\mu \tag{1.11}$$

is not invariant.

Gauge invariance for non-Abelian groups was introduced by Yang and Mills [1]. A generic symmetry transformation for a non-Abelian group with generators t_a, satisfying the Lie algebra,

$$[t_a, t_b] = iC_{abc}t_c, \tag{1.12}$$

where C_{abc} are the structure constants of the group, can be written as:

$$U(x) = \exp\left[i\sum_a \alpha^a(\mathbf{x})t^a\right], \tag{1.13}$$

where $\alpha^a(\mathbf{x})$ are continuous, real parameters and t^a are the generators of the symmetry group.

Introducing one gauge field A^a_μ for each generator t^a, a covariant derivative that ensures the invariance of the Lagrangian, has the form

$$D_\mu = \partial_\mu - igt^a A^a_\mu, \tag{1.14}$$

where g is a coupling constant. The introduced gauge fields then transform as follows:

$$A_\mu(\mathbf{x})^a \rightarrow A_\mu(\mathbf{x})^{a\prime} = A^a_\mu - \frac{1}{g}\partial_\mu\alpha^a + C_{abc}\alpha^b A^c_\mu. \tag{1.15}$$

The mass term for gauge bosons is still not gauge invariant.

1.1.3 The SM Particles and Their Interactions

Known elementary particles can be categorized according to their spin into fermions with half-integer spin and bosons with integer spin. Fermions are further divided into leptons, which do not interact via strong force and quarks which undergo strong interactions. Both quarks and leptons have three generations, which differ only in the masses, but undergo the same symmetry transformations. Each generation of quarks and leptons comprises two particles of different flavor, that form doublets of weak isospin. In addition, each fermion has an associated anti-particle with the same mass but opposite quantum numbers. This yields in total 2×12 fermions, as summarized in Table 1.1.

The number and properties of fermions are determined by experiments. The only theoretical constraints from the SM are that fermions must belong to the representation of the symmetry group, and the representations must lead to the cancellation of quantum anomalies [2]. These constraints are satisfied for the known fermions.

	1st generation		2nd generation		3rd generation	
	flavor	mass	flavor	mass	flavor	mass
leptons	ν_e	< 2 eV	ν_μ	< 2 eV	ν_τ	< 2 eV
	e	512 keV	μ	105.6 MeV	τ	1.777 GeV
quarks	u	≈ 2.5 MeV	c	1.27 GeV	t	172 GeV
	d	≈ 5 MeV	s	101 MeV	b	4.2 GeV

Table 1.1: Fermionic particle content of the SM.

Particles that are charged under a certain symmetry group can interact with each other. The interactions are mediated by the spin 1 gauge bosons that are associated to the symmetry groups. The symmetry group of the SM is given by

$$U(1)_{\mathrm{Y}} \otimes SU(2)_{\mathrm{L}} \otimes SU(3)_{\mathrm{C}}, \tag{1.16}$$

where the subscripts C, L and Y denote color, left-handed chirality and weak hypercharge, respectively. The gauge group uniquely determines the interactions and the number of gauge bosons that correspond to the generators of the group: four gauge bosons, $W^{\pm}$, Z and γ, corresponding to three generators of $SU(2)_{\mathrm{L}}$ and one generator of $U(1)_{\mathrm{Y}}$ and eight gluons of the $SU(3)_{\mathrm{C}}$ symmetry group that mediate the strong interactions between quarks. The symmetry group fixes the number and properties of the vector gauge bosons, leaving three coupling constants of $SU(3)_{\mathrm{C}}$, $SU(2)_{\mathrm{L}}$ and $U(1)_{\mathrm{Y}}$ groups as independent unknown parameters, that need to be determined from the experiment. Gauge bosons along with their masses and symmetry groups are summarized in Table 1.2.

Only the left chiral components of the fundamental fermions are affected by the $SU(2)_{\mathrm{L}}$ symmetry transformations and form doublets of weak isospin at each particle generation. Additionally all quarks carry color charge of $SU(3)_{\mathrm{C}}$ group and all fermions, besides neutrinos, carry electric charge. The quantum numbers of fermions are summarized in Table 1.3.

1.1.4 Electroweak interactions

The first hint about the theory of weak interactions came from the electron energy spectrum, measured from the neutron β-decay, which seemed to indicate a violation of energy, as no third particle was observed. As an explanation to the situation Fermi proposed a light neutral particle (a neutrino), which only interacts through the weak interaction that mediates the β-decay. In 1933 Fermi presented a theory, which explained β-decay as a direct interaction of four fermions at one vertex [3]. After the parity violation was experimentally observed [4], a weak theory in terms of V-A (vectorial-axial)

boson	mass	electric charge	symmetry group
γ	$< 10^{-18}$ eV* 0 eV†	0	$U(1)_{\rm Y} \otimes SU(2)_{\rm L}$
Z	91.188 GeV	0	$U(1)_{\rm Y} \otimes SU(2)_{\rm L}$
$W^\pm$	80.40 GeV	± 1	$U(1)_{\rm Y} \otimes SU(2)_{\rm L}$
g	< 20 MeV* 0 eV†	0	$SU(3)_{\rm C}$

* Experimental limit.
† Theoretical value.

Table 1.2: The SM gauge bosons.

particles			el. charge	weak isospin	color
$\begin{pmatrix} \nu_e \\ e \end{pmatrix}_{\rm L}$	$\begin{pmatrix} \nu_\mu \\ \mu \end{pmatrix}_{\rm L}$	$\begin{pmatrix} \nu_\tau \\ \tau \end{pmatrix}_{\rm L}$	0 -1	$+1/2$ $-1/2$	–
$\begin{pmatrix} u \\ d \end{pmatrix}_{\rm L}$	$\begin{pmatrix} c \\ s \end{pmatrix}_{\rm L}$	$\begin{pmatrix} t \\ b \end{pmatrix}_{\rm L}$	$+2/3$ $-1/3$	$+1/2$ $-1/2$	r,g,b
e_R	μ_R	τ_R	-1	0	–
u_R	c_R	t_R	2/3	0	r,g,b
d_R	s_R	b_R	-1/3	0	r,g,b

Table 1.3: Quantum numbers of the SM fermions

structure was developed [5, 6]. The remaining fundamental drawback of the V-A theory was its divergent behavior at high energies.

The modern description of electroweak interactions, which is based on the quantum field theory, was formulated by Glashow, Salam and Weinberg in 1960s [7, 8, 9]. They suggested the unification of electromagnetic and weak interactions under a $SU(2)_{\mathrm{L}} \otimes U(1)_{\mathrm{Y}}$ gauge group. The unification became the basis of the SM.

The symmetry group $SU(2)_{\mathrm{L}}$ is called weak isospin. The elements of the group act in a nontrivial way only on the left-handed chiral components of the fermion fields. The group has three generators I_a, which satisfy the angular momentum commutation relations

$$[I_a, I_b] = i\varepsilon_{abc} I_c, \tag{1.17}$$

where ε_{abc} is the totally antisymmetric tensor. In the two-dimensional representation the generators are given by Pauli matrices σ_1, σ_2 and σ_3. $U(1)_Y$ grop has one generator Y.

Introducing the covariant derivative requires four gauge bosons: (W^1, W^2, W^3), corresponding to three generators of $SU(2)$ and B^0, corresponding to the $U(1)$ transformation. The derivative then transforms as

$$\partial_\mu \to D_\mu = \partial_\mu - i\frac{g}{2}\vec{\sigma}\cdot\vec{W}_\mu - i\frac{g'}{2}YB^0_\mu. \tag{1.18}$$

All of the introduced gauge bosons are massless, since adding the mass term would spoil the gauge invariance.

1.1.5 Spontaneous Symmetry Breaking and the Higgs Mechanism

In the SM the physically observable W, Z and γ bosons are produced by the spontaneous symmetry breaking from $SU(2)_{\mathrm{L}} \otimes U(1)_{\mathrm{Y}}$ to $U(1)_{\mathrm{EM}}$, caused by the Higgs mechanism [10, 11, 12]. The three weak gauge bosons $W^\pm$ and Z are massive, while the photon is massless. The necessary longitudinal degrees of freedom can be obtained by introducing the Higgs field, which is a Lorentz scalar and complex $SU(2)_{\mathrm{L}}$ doublet

$$\varphi = \begin{pmatrix} \varphi_1 + i\varphi_2 \\ \varphi_3 + i\varphi_4 \end{pmatrix}. \tag{1.19}$$

The Lagrangian of the Higgs field reads

$$\mathcal{L} = (D_\mu\varphi)^\dagger(D^\mu\varphi) - V(\varphi), \tag{1.20}$$

where the Higgs boson self-interaction potential $V(\varphi)$ has the form

$$V(\varphi) = \mu^2\varphi^\dagger\varphi + \lambda(\varphi^\dagger\varphi)^2. \tag{1.21}$$

Such a Lagrangian is invariant under the local gauge transformations. Positive λ ensures that the potential is bounded from below. For $\mu^2 \geq 0$ the minimum of the potential V is at $\varphi = 0$. The choice $\mu^2 < 0$ realizes the spontaneous symmetry breaking

$$SU(2)_{\mathrm{L}} \times U(1)_{\mathrm{Y}} \rightarrow U(1)_{\mathrm{EM}}, \tag{1.22}$$

where $U(1)_{\mathrm{EM}}$ is the symmetry group of electromagnetic interactions, associated with the conservation of electric charge.

The Higgs potential then has a minimum at

$$\varphi^{\dagger}\varphi = -\frac{\mu^2}{2\lambda} \equiv \frac{v^2}{2}, \tag{1.23}$$

which represents an infinite number of solutions with different phases of the Higgs field. The minimum of the potential corresponds to the vacuum.

Without loss of generality we can fix the value of φ in the ground state and choose

$$\langle 0|\varphi|0\rangle = \frac{1}{\sqrt{2}} \begin{pmatrix} 0 \\ v \end{pmatrix}. \tag{1.24}$$

Writing the Higgs field in the exponential form and choosing the unitary gauge yields:

$$\varphi(\mathbf{x}) = \frac{1}{\sqrt{2}} \begin{pmatrix} 0 \\ v + h(\mathbf{x}) \end{pmatrix}, \tag{1.25}$$

with one physical electrically neutral Higgs field $h(\mathbf{x})$ and vacuum expectation value v.

The kinetic term of the Higgs Lagrangian can be expanded as

$$\begin{aligned} (D_\mu\varphi)^{\dagger}(D^\mu\varphi) &= \frac{g^2v^2}{8}(W_{1\mu} + iW_{2\mu})(W_1^\mu - iW_2^\mu) && (1.26)\\ &+ \frac{v^2}{8}(gW_3^\mu - g'B^\mu)(gW_{3\mu} - g'B_\mu) + && (1.27)\\ &+ \frac{1}{2}\partial_\mu h \partial^\mu h + ... && (1.28) \end{aligned}$$

The charged weak interaction mass eigenstates can be read from the first term in the Lagrangian 1.26 as

$$W^\mu \equiv \frac{W_1^\mu - iW_2^\mu}{\sqrt{2}}, \tag{1.29}$$

with the mass $M_W = \frac{1}{2}gv$.

The second term in the Lagrangian 1.26 is a mixture of the neutral gauge fields W_3^μ and B^μ. Performing a rotation in the W_3^μ-B^μ plane yields the orthogonal mass eigenstates Z and γ:

$$\begin{pmatrix} \gamma \\ Z \end{pmatrix} = \begin{pmatrix} \cos\theta_W & \sin\theta_W \\ -\sin\theta_W & \cos\theta_W \end{pmatrix} \begin{pmatrix} B \\ W_3 \end{pmatrix}, \tag{1.30}$$

where θ_W is the weak mixing angle, which satisfies the relation

$$\tan\theta_W = \frac{g'}{g}. \tag{1.31}$$

In such a framework the photon remains massless, while the Z boson acquires a mass of

$$m_Z = \frac{gv}{2\cos\theta_W} = \frac{m_W}{\cos\theta_W}. \tag{1.32}$$

The remaining symmetry group $U(1)_{EM}$ is different from $U(1)_Y$, since the electric charge is a linear combination of hypercharge and weak isospin: $Q = \frac{Y}{2} + I_3$.

In principle, the Higgs sector of the SM could be extended by including other Higgs multiplets, all of which have vacuum expectation values, which contribute to the generation of gauge boson masses through the Higgs mechanism. For an arbitrary number of such Higgs multiplets Φ_k, we can define a parameter ρ, which is given by

$$\rho = \frac{\sum_k (I^k(I^k+1) - I_3^k)v_k^2}{2\sum_k I_3^k v_k^2}, \tag{1.33}$$

where I^k is the weak isospin of the Higgs multiplet Φ_k and I_3^k is the third component of the weak isospin of the component of Φ_k, which has a vacuum expectation value v_k. The relation implies that $\rho = 1$ for any number of Higgs doublets.

In the SM, a ρ parameter is given by

$$\rho = \frac{m_W^2}{m_Z^2\cos^2\theta_W} = 1 \tag{1.34}$$

The experimental test of this parameter is an important check of the structure of the Higgs sector. Currently the theoretical expectation of the SM is in perfect agreement with the experimental value $\rho = 0.9998^{+0.0008}_{-0.0005}$. Therefore, the experimental data leave open only the possibility of other Higgs doublets, besides the standard one, which generate the masses of the W and Z bosons through the Higgs mechanism.

1.1.6 Strong interactions

The theory of strong interactions based on the local symmetry group $SU(3)_{\mathrm{C}}$ is called quantum chromodynamics (QCD). $SU(3)_{\mathrm{C}}$ gauge group has eight generators, giving rise to eight massless vector bosons, the gluons. Among the fermions only the quarks carry color charge. Strong interactions can be studied separately from the electroweak interactions, because the symmetry under $SU(3)_C$ is unbroken and there is no mixing between the $SU(2)_{\mathrm{L}} \times U(1)_{\mathrm{Y}}$ and $SU(3)_{\mathrm{C}}$ sectors.

The dynamics of quarks and gluons is described by the QCD Lagrangian

$$\mathcal{L}_{QCD} = \bar{\psi}_i(i\gamma^\mu(D_\mu)_{ij} - m_i\delta_{ij})\psi_j - \frac{1}{4}G^a_{\mu\nu}G^{\mu\nu}_a, \tag{1.35}$$

here ψ_i are the quark fields and $G^a_{\mu\nu}$ represent the set of eight gauge invariant gluonic field strength tensors, given by

$$G_{\mu\nu} = \partial^\mu G^\nu_a - \partial^\nu G^\mu_a - g_s f_{abc} G^\mu_b G^\nu_c, \tag{1.36}$$

where G^a_μ are the gluon fields.

The nonabelian character of the color symmetry implies that gluons are self-interacting. Moreover, the QCD coupling constant g_s is not small and the theory cannot be solved in a perturbative way in the low-energy domain. At high energies, however, the renormalized coupling constant becomes small, allowing a perturbative treatment.

An important property of QCD is the color confinement: all free particles must be in color singlet state. Individual quarks or gluons that are produced in particle collisions must undergo further strong interactions and reach a color singlet state. The transition from colored quarks or gluons to a set of colorless hadrons is called hadronization.

1.2 Neutrino Masses

By definition, only three left-handed massless neutrinos are included in the SM. The experimental observation of neutrino oscillations [13, 14, 15, 16], however, indicates non-zero neutrino mass differences and makes clear that neutrinos do have masses at least of $\mathcal{O}(0.01)$ eV. Also, the weak interaction eigenstates – the electron neutrino ν_e, muon neutrino ν_μ and tau neutrino ν_τ do not coincide with their mass eigenstates ν_1, ν_2 and ν_3 and the neutrino mass matrix is diagonalized by the unitary leptonic mixing matrix U by

$$m_\nu = U^* m_\nu U^\dagger, \tag{1.37}$$

where the diagonalized neutrino mass matrix m^D_ν is given by

$$m^D_\nu = \begin{pmatrix} m_1 & 0 & 0 \\ 0 & m_2 & 0 \\ 0 & 0 & m_3 \end{pmatrix}. \tag{1.38}$$

The masses of ν_1 and ν_2 differ by $\Delta m^2_{21} = (7.59 \pm 0.21) \times 10^{-5}$ eV^2 and $m_1 < m_2$ [17]. The third eigenstate ν_3 is separated from the first two by splitting $\Delta m^2_{32} = (2.43 \pm 0.13) \times 10^{-3}$ eV^2 [17] and can be heavier or lighter than ν_1 and ν_2. The two possibilities are illustrated in Figure 1.1 and are called normal and inverted spectrum, respectively. If the lowest neutrino mass is large in comparison to the measured mass differences, then the neutrino masses are nearly degenerate, $m_1 \approx m_2 \approx m_3$.

The origin of the measured neutrino mass is unknown and it is generally believed that massive neutrinos are a low-energy manifestation of physics beyond the SM.

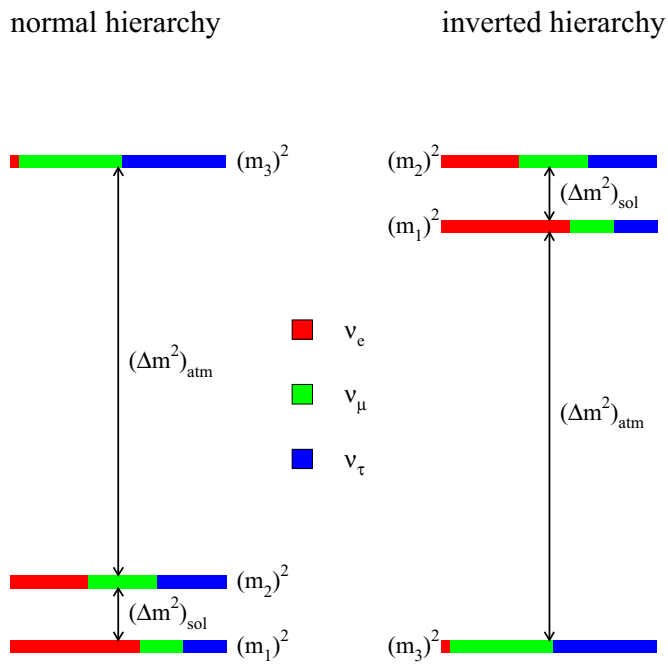

Figure 1.1: Illustration of two possible neutrino mass hierarchies that fit the current neutrino data. The color indicates the fraction of each distinct flavor ν_α ($\alpha = e, \mu, \tau$) contained in each mass eigenstate ν_i ($i = 1, 2, 3$).

1.2.1 Dirac masses

In the minimally extended SM the Dirac neutrino mass can be generated by the same Higgs mechanism that gives masses to quarks and charged leptons by additionally introducing three right-handed neutrino fields. Right-handed neutrino fields are invariant under all symmetries of the SM and are thus called sterile; their only interaction is gravitational.

The neutrino mass term in the Lagrangian then reads

$$\mathcal{L}_{m_\nu} = -m_{ij}\overline{\nu_L}^i \nu_R^j. \tag{1.39}$$

Such neutrino masses are proportional to the Higgs vacuum expectation value v, just as the masses of other fermions. Since the neutrino masses are much smaller, extraordinarily small Higgs-neutrino Yukawa couplings are needed, that is not explained by the theory.

1.2.2 Majorana masses

Chiral fermion fields ψ_L and ψ_R are two-component spinors and the smallest irreducible representations of the Lorentz group from which a general fermion field, represented by a four-component spinor, can be composed as

$$\psi = \psi_L + \psi_R. \tag{1.40}$$

Majorana proposed that massive neutrinos can be fully described by a two-component spinor [18] by assuming that ψ_L and ψ_R are not independent, but

$$\psi_R = \mathcal{C}\overline{\psi_L}^T = \psi_L^C, \tag{1.41}$$

where $\mathcal{C}$ is the charge conjugation matrix and ψ_L^C denotes the charge conjugated field. Using this convention the Majorana field can be written as

$$\psi = \psi_L + \psi_L^C, \tag{1.42}$$

which implies the equality of particle and antiparticle. Neutrinos are the only fermions in the SM that do not have electric charge and can therefore be Majorana particles.

The Majorana mass term involves only the neutrino left-handed chiral field ν_L, which is present in the SM

$$\mathcal{L}_{m_\nu} = -\frac{1}{2} m_{ij} \overline{\nu_L}^{Ci} \nu_L^j. \tag{1.43}$$

It violates the lepton number and breaks the SM symmetry as $\overline{\nu_L}^C \nu_L$ has the third component of weak isospin $I_3 = 1$ and hypercharge $Y = -2$. The SM does not contain any weak isospin triplets.

The lowest dimensional non-renormalizable term that could generate a Majorana mass term with the SM fields and respecting the SM symmetries is the dimension five operator

$$\frac{g}{\mathcal{M}} \bar{\ell}_i \varphi \bar{\ell}_j \varphi, \tag{1.44}$$

where g is a dimensionless coupling constant and $\mathcal{M}$ is a constant with mass dimension. As a consequence of electroweak symmetry breaking a Majorana mass term is generated for ν_L, corresponding to the Majorana mass

$$m = \frac{g v^2}{\mathcal{M}}. \tag{1.45}$$

The smallness of neutrino masses comes from the heavy mass scale $\mathcal{M}$ and the heavier the mass scale, the lighter are the neutrino masses. There are three beyond the SM tree-level realizations of the non-renormalizable operator (1.44) called the "seesaw mechanism" that are classified by the heavy particles involved:

- Type I – massive right-handed neutrinos,
- Type II – scalar triplet,
- Type III – fermion triplet.

1.2.3 Neutrino Mixing

For three flavors of Majorana neutrinos the leptonic mixing matrix U depends on three mixing angles and three phases and can be parametrized as

$$U = \begin{pmatrix} 1 & 0 & 0 \\ 0 & c_{23} & s_{23} \\ 0 & -s_{23} & c_{23} \end{pmatrix} \begin{pmatrix} c_{13} & 0 & s_{13}e^{-i\delta} \\ 0 & 1 & 0 \\ -s_{13}e^{i\delta} & 0 & c_{13} \end{pmatrix} \begin{pmatrix} c_{12} & s_{12} & 0 \\ -s_{12} & c_{12} & 0 \\ 0 & 0 & 1 \end{pmatrix} \begin{pmatrix} e^{i\alpha_1} & 0 & 0 \\ 0 & e^{i\alpha_2} & 0 \\ 0 & 0 & 1 \end{pmatrix}, \tag{1.46}$$

where $c_{ij} \equiv \cos\theta_{ij}$, $s_{ij} \equiv \sin\theta_{ij}$, θ_{ij} are the three mixing angles ($0 \leq \theta_{ij} \leq \pi/2$), δ is the Dirac CP violating phase and α_1,α_2 are the two physical Majorana CP violating phases. The CP violating phases satisfy $0 \leq \delta, \alpha_1, \alpha_2 < 2\pi$.

Chapter 2

The LHC and the CMS experiment

2.1 General Description of the LHC

The Large Hadron Collider (LHC) [19] is the world's largest particle collider. It is located at CERN, the European Laboratory for Particle Physics [20], at the border between Switzerland and France near Geneva. The LHC is situated about 100 m below the surface in the 27 km long circular tunnel, that formerly hosted the Large Electron-Positron collider (LEP, 1989-2000).

The LHC particle collider is composed of a ring of 1232 dipole magnets that store two counter-rotating hadron beams (either protons or lead ions) that collide at four interaction points, where the four particle detectors are situated: ALICE (A Large Ion Collider Experiment [21]), ATLAS (A Toroidal LHC ApparatuS [22]), CMS (Compact Muon Solenoid [23]) and LHCb (Large Hadron Collider beauty [24]). ALICE is specialized to the study of heavy ion collisions, and LHCb to the study of b-quark physics. ATLAS and CMS are large complementary general-purpose experiments, designed to probe a broad range of physics phenomena. They are accompanied by two smaller detectors – LHCf (Large Hadron Collider forward [25]) and TOTEM (TOTal Elastic and diffractive cross section Measurement [26]), respectively. The position of LHC particle accelerator and its main experiments is illustrated in Figure 2.1.

The LHC is designed to achieve proton-proton collisions with a center-of-mass energy of $\sqrt{s} = 14$ TeV and a peak luminosity of $\mathcal{L} = 10^{34}$ cm^{-2}s^{-1}. For a gaussian beam distribution, the instantaneous luminosity (number of collisions per unit time and transverse section of the beams) is defined as:

$$\mathcal{L} = \frac{1}{4\pi \cdot m_0 c^2} \cdot \frac{f k_B N_p^2}{\epsilon_n \beta^*} F, \tag{2.1}$$

where f is the revolution frequency which is geometrically fixed by design, k_B is the number of bunches per beam, N_p is a number of protons per bunch, ϵ_n – the normalized transverse emittance – is a beam property related to the area occupied by the particles of the beam, β^* is the β function at the collision point that characterizes the width of

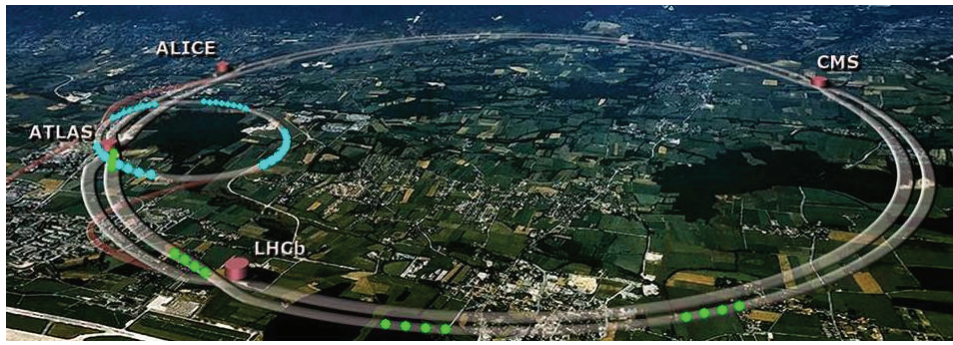

Figure 2.1: LHC particle accelerator.

the beam and F is the geometric luminosity reduction factor due to the crossing angle at the interaction point.

In order to bend the beams onto their circular orbit, a magnetic field of 8.4 Tesla is provided by superconducting magnets at a current of around 11 700 A operating at cryogenic temperatures of 1.9 K. Before entering the main LHC ring, the beams pass an injector chain. The protons are injected into the LHC at the energy of 450 GeV, accelerated to their nominal energy, and stored up to 20 hours.

The construction of the LHC particle collider with its experiments has been finished and the first beams circulated in 2008. The physics program started with collisions at modest energies in 2009. The LHC operated at $\sqrt{s} = 7$ TeV in 2010 and 2011, collecting pp-collisions with an integrated luminosity of more than 5 fb^{-1}. This enables a large range of physics analyses at previously untested energies.

2.2 The CMS experiment

The Compact Muon Solenoid (CMS) detector is one of the two large multi-purpose experiments at the LHC. It has an intense solenoidal magnetic field of 3.8 T, an excellent muon detection system and with its diameter of 15 m, a length of 21 m, and a weight of about 14 000 t, CMS is a compact detector compared to ATLAS.

CMS has a cylindrical coordinate system, based on (x, y, z) or (r, ϕ, η), where z is the direction along the beam pipe, x points to the centre of the LHC from the origin, $r = \sqrt{x^2 + y^2}$ is the radius in the transverse pane, ϕ is the azimuthal angle and $\eta = -\ln \tan \frac{\theta}{2}$ is the pseudorapidity that is commonly used instead of the polar angle θ. In order to detect the particles in the widest possible range, CMS covers the full azimuthal angle $-\pi < \phi < \pi$ and the polar angle up to $|\eta| < 5$.

CMS consists of several sub-detectors. Starting from the centre, the first sub-detector is the tracking system, the purpose of which is precise and efficient measurement of the trajectories of charged particles. In the strong magnetic field of the

surrounding solenoid, the transverse momenta of charged particles can be measured from the radius of curvature of the track by:

$$p_T = qrB, \tag{2.2}$$

where p_T is the transverse momentum, q is the particle charge, r is the radius of curvature of the track, and $B = 3.8$ T is the strength of the magnetic field. In addition the tracker provides the information about the secondary vertices and impact parameters [27]. The tracker is composed of the silicon pixel detector that is closest to the beam spot and the silicon microstrip detector. The tracker covers the pseudorapidity range of $|\eta| < 2.5$.

Moving further outwards, the scintillating electromagnetic calorimeter (ECAL) [28] , measures the energy and position of photons and electrons and contributes to the measurement of the energy in hadronic showers. It is composed of lead tungstate ($PbWO_4$) crystals that are characterized by high density, hermeticity and homogeneity, which allows a fine granularity, fast response and compact size. ECAL covers the pseudorapidity range up to $|\eta| < 3.0$ and consists of two structures: the barrel ECAL in the pseudorapidity range $|\eta| < 1.479$ and two ECAL endcaps, covering the pseudorapidity range $1.479 < |\eta| < 3.0$.

The subsequent hadron calorimeter (HCAL) detects hadronic showers and plays a major role in the reconstruction of missing transverse energy [29]. It is a sampling calorimeter, which consists of plastic scintillator tiles with embedded wavelength-shifting fibers and brass absorber. It completely surrounds the ECAL, and covers a pseudorapidity range up to $|\eta| < 5.2$.

The outermost layer of the CMS experiment consists of the muon detection system [30]. It was one of the main design objectives of the CMS to obtain high precision muon measurements. Muons are heavier than electrons and do not exhibit strong interactions, so they can traverse through the calorimeter and magnet with minimal interaction with the detector, while the big amount of material between the interaction point and the muon detector absorbs nearly all other particles. CMS uses three types of gaseous particle detectors for muon identification: Drift Tubes, Cathode Strip Chambers and Resistive Plate Chambers. Muon detectors cover the pseudorapidity interval $|\eta| < 2.4$ with no acceptance gaps.

Figure 2.2 shows the trajectories of photons, electrons, hadrons, muons and neutrinos created in a proton-proton collision and traveling through the sub-detectors of CMS. Photons only leave a signal in the ECAL, where their energy is absorbed and measured. Electrons are first measured as charged particles in the tracker and then absorbed in the electronic calorimeter. Charged and neutral hadrons are able to reach the hadronic calorimeter, where they deposit their energy in a cascade process. Muons pass the inner detectors nearly unaffected and are identified in the muon spectrometer. The neutrinos do not interact with matter and escape direct detection. A drawing of the complete CMS detector, illustrating both its scale and complexity is shown in Figure 2.3

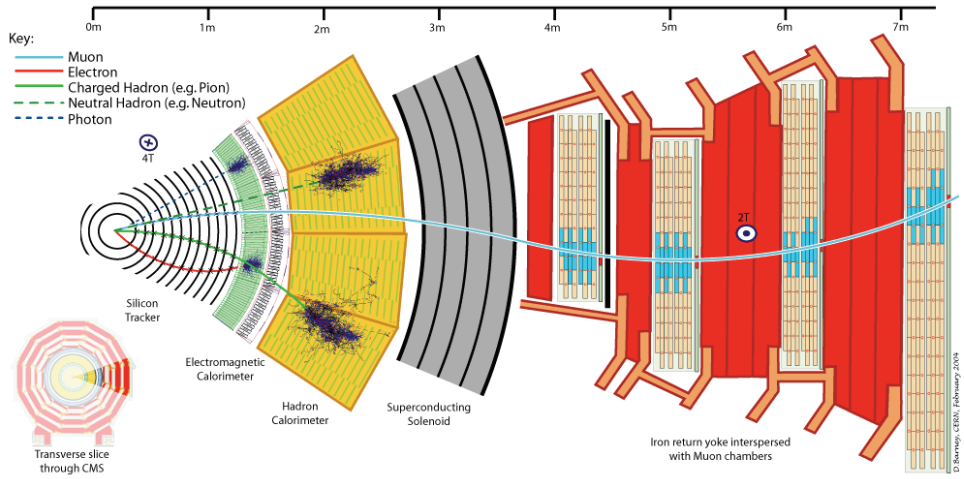

Figure 2.2: Slice of the CMS detector.

2.2.1 Data Acquisition System and Trigger

A very high production rate of collisions is observed at the LHC, handling the bunch crossing rate of up to 40 MHz. The maximum allowed data rate the Data Acquisition System (DAQ) can cope with is about 100 GB per second. The trigger system is the initial stage of the physics event selection that reduces the amount of data to a processable and storable size. The CMS trigger system consists of two steps: Level-1 (L1) Trigger [31] that reduces the rate to approximately 100 kHz and High-Level Trigger (HLT) [32] that further decreases the rate to $\mathcal{O}(100)$ events per second. In both stages challenging decisions need to be made in order to discard majority of data while keeping the few interesting collisions that are analyzed further.

The L1 Trigger has to take decision to keep or discard data from a particular bunch crossing within 3.2 μs. This is not sufficient to read data from the whole detector. Thus L1 Trigger uses data only from calorimeters and muon system, but not the tracker that is too slow for this purpose.

If the event passed L1 Trigger selection, the whole detector data is read out and processed by the HLT that runs a more sophisticated algorithm, resulting in a reconstructed event. HLT is divided into three levels: L2, L2.5 and L3. At L2 only the full information of the muon system and of the calorimeters is used, performing reconstruction of more complex physics objects such as iterative cone jets and super-clusters. At L2.5 the information from the tracker is read out. At L3 the full event information is available and tracks are reconstructed.

Based on the physics priorities, there are different sets of selection criteria both for L1 an HLT that define events of interest – they are called trigger paths. The set of

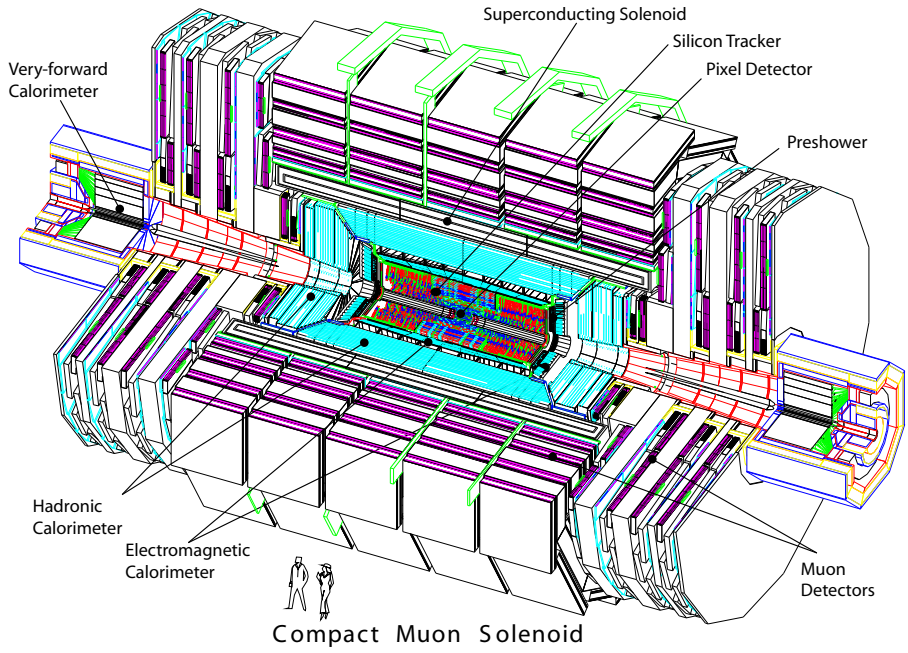

Figure 2.3: Drawing of the CMS detector.

trigger paths that is checked at a given time is called a trigger menu. Based on different HLT paths, triggered data is classified into various datasets for further analysis.

Chapter 3

Event Simulation and Reconstruction

3.1 Event Simulation

Computer simulations interface theory and experiment in high energy physics, providing comparison of theoretical expectations to experimental output from the detector. Simulating the involved physical processes directly is difficult. Instead, the Monte Carlo technique is used [33] that performs a large number of simulated experiments based on random number generation.

3.1.1 Monte Carlo Event Generation

Event generation consists of several stages. The structure of the colliding protons is described by Parton Distribution Functions (PDF) that define the probability density function of partons (quarks or gluons). The collision occurs between individual partons, with the PDFs determining the energy of the process. The production cross sections for different processes that emerge from the collision are given by the matrix element and are calculated from Feynman diagrams in quantum field theory. Matrix element calculators, such as POWHEG [34], ALPGEN [35] or MADGRAPH [36] are capable of calculating next-to-leading-order (NLO) corrections to matrix elements and provide parton level events as input to further event simulation.

In addition to the two partons that create the scattering process, the colored remnants of protons that participate in the collision form collections of colorless hadrons due to QCD confinement. These interactions represent the so called underlying event. The process of hadronization is modeled phenomenologically with the Lund String Model [37] that treats gluons as field lines, which are attracted to each other and form a narrow string of strong color field. This string fragmentation model explains many features of hadronization quite well and is used by general event generators such as PYTHIA [38]. Some of the particle decays are modeled by distinct simulation packages like TAUOLA

[39] that covers tau decays.

An additional effect to be considered are the luminosity dependent pile-up collisions, where multiple protons in a single bunch crossing interact. The pile-up contribution is simulated separately by adding minimum bias events on the events in the nominal samples.

3.1.2 Detector Simulation

The Monte Carlo event generation only models the physics of the particle collision. The interaction of generated particles with the CMS detector is evaluated by a separate toolkit GEANT4 [40]. The detector simulation step takes as input the generated particles, propagates them through the matter and models physics processes that happen during this passage. Subsequently detectors electronic response is simulated and pile-up events are superimposed in order to generate the dataset, which is as close as possible to the data recorded by the CMS detector.

3.2 Reconstruction

The raw output data from the detector is not directly usable in the physics analysis. It contains objects like hits in the tracker or energy deposits in the calorimeters that must be reconstructed to the high-level objects, such as tracks, vertices, jets, leptons and missing transverse energy (E_T^{miss}). In order to realistically compare experimental data with theoretical predictions, the same reconstruction algorithm is applied to data and the output of the Monte Carlo simulation chain.

3.2.1 Tracks

Tracks of charged particles are fundamental objects that are used for further reconstruction of many physics objects, including event vertex, leptons, jets and E_T^{miss}. Tracks are reconstructed using the information from the tracker sub-detector (see Section 2.2) that has fine resolution and allows to measure the momentum of charged particles with great precision. An identified track is parametrized by its transverse impact parameter d_0 that characterizes the distance to the beam axis in the x-y plane, the position on the z-axis, transverse momentum (p_T), and its direction described by ϕ and η. Full track reconstruction is possible in the range of about 0.1 GeV to 1 TeV. The upper bound corresponds to the situation where the track is reconstructed as a straight line, because its bending in the magnetic field is too small to be measured.

Track reconstruction is an iterative process that consists of several steps [41]. At first the initial track candidates (seeds) are generated by grouping a few hits in the pixel and microstrip detectors. Next new hits that are found in the tracker are progressively added to the seed trajectory according to the equation of motion of a charged particle in the magnetic field. The process continues until no further compatible hits are found

and a fit is performed to obtain estimates for the track parameters. Multiple iterations of this process are needed in order to remove the ambiguities resulting from hits being assigned to multiple tracks.

3.2.2 Vertex Reconstruction

An event is identified by an existence of at least one primary vertex, possibly accompanied by additional secondary vertices. There are various algorithms that are used for different types of vertex reconstruction. Most algorithms include two steps: the vertex finding that groups the tracks together and forms vertex candidates and the vertex fitting that calculates the vertex parameters with increased precision.

The primary vertex indicates the point where particles collide, which can be different from the nominal interaction point. It is reconstructed using the tracks that come directly from the interaction. Such tracks are preselected based on the transverse impact parameter (d_0) that describes their distance to the beam. Next the selected tracks, that pass basic track quality criteria, are clustered along the z-coordinate and a primary vertex candidate fit is performed for each of the clusters [42].

3.2.3 Luminosity

Luminosity is measured with the forward hadronic calorimeter that is situated in pseudorapidity range $3 < |\eta| < 5$ close to the beam pipe. The real-time instantaneous luminosity is computed online by two methods. The first method computes the mean number of interactions per bunch crossing based on the average fraction of empty towers. The second method relies on the linear relationship between luminosity and average transverse energy per tower.

The absolute normalization of the luminosity is determined by the Van der Meer method [43] that scans the colliding beams in the transverse plane to determine their overlapping region.

3.2.4 Particle-Flow Algorithm

The particle-flow (PF) reconstruction algorithm [44] uses the information from all subdetectors, aiming to provide a global event description at the level of individually reconstructed particles.

Firstly, all tracks and energy clusters are reconstructed in each sub-detector. Next, all the candidates are associated in an optimal combination to one or more of these sub-detector signals, if they are compatible with the physics properties of each particle, and reconstructed in the event. The final set of particles (charged hadrons, neutral hadrons, photons, electrons and muons) is used to derive composite physics objects such as jets, tau-jets and missing transverse energy.

3.2.5 Jet Reconstruction

Colored quarks and gluons undergo hadronization, producing collimated streams of charged and neutral particles. There are several ways to group the tracks and calorimeter energy to composite physics objects, called jets.

The PF-jets are reconstructed from the list of identified particles and as the PF algorithm allows to precisely measure charged hadrons and photons inside jets, the measurement precision of the jet momentum and spatial resolution, are expected to be improved.

3.2.6 Tau Reconstruction

τ-leptons are the heaviest of leptons and are of great importance for many new physics searches. They can decay either to light leptons or to hadrons (charged mesons generally accompanied by neutral pions). Hadronic tau decays or tau-jets (τ_{had}) leave similar signature to the detector as QCD-jets and an efficient method is needed to discriminate them from the large QCD-jet background. The PF algorithm that uses the information both from the tracker and the calorimeters provides the best results.

Tau reconstruction starts with the reconstruction of a jet. Next a leading track is defined within $\Delta R < 0.1$ around the jet axis and required to have $p_T > 5$ GeV. Subsequently, various tau identification algorithms can be used to identify a final sample of τ_{had} candidates. In the analyses that are summarized in this thesis, the hadron plus strips [45] (HPS) algorithm is used.

The HPS algorithm is optimized for reconstruction of neutral pions within the decay. Their identification is enhanced by clustering the PF electrons and photons into "strips" along the bending plane to take account of possible broadening of calorimeter signatures due to photon conversions. The HPS tau identification algorithm identifies decay modes with one charged hadron and up to two strips, or three charged hadrons without reconstructed strips. An additional requirement is imposed on the four-vector sum of combinations of strips and hadrons, that have to be compatible with the π^0, ρ or a_1 masses. All charged hadrons and photons that can not be associated to a reconstructed tau decay are taken into account when estimating the tau isolation.

3.2.7 Missing Transverse Energy

In hadron collider, such as the LHC, an inelastic collision event is the collision of two partons. The energy of a parton is an unknown fraction of the proton energy, thus the partonic collision energy of each event is not fixed. As particles can exit undetected through the beam pipe, the longitudinal energy of an event is not a well-measured quantity. On the other hand, as the incoming particles have negligible transverse momenta, the net transverse energy of an event needs to be balanced due to the conservation laws. The missing transverse energy (E_T^{miss}) quantifies the amount of energy that escapes undetected. E_T^{miss} can arise due to the limited coverage of the detector, the presence of

neutrinos or the presence of new unknown weakly interacting particles. The PF based E_T^{miss} in the event is defined as the negative vectorial momentum sum of all particle candidates reconstructed by the PF algorithm.

Chapter 4

Measurement of the $W \to \tau\nu$ Cross Section

4.1 Introduction

The production of W-bosons and their subsequent decay into τ-leptons at LHC is very well predicted by theory. The main theoretical uncertainty comes from the parton distribution functions. Experimental measurement of the W-boson cross section provides a comparison between the current theoretical models and simulation tools to the signature of the CMS detector.

The decay of W-bosons provides a dominant source for tau leptons in the Standard Model, exceeding the production rate of $Z \to \tau^+\tau^-$ [46] events by nearly an order of magnitude. However, the experimental signature of a single tau-jet plus undetected neutrinos is more challenging, requiring a good understanding of hadronic tau identification and missing transverse energy.

Tau leptons are an important probe for many new physics processes at the LHC. Among others, experimental signatures that involve decays to tau leptons are crucial for searches for light Higgs bosons, Supersymmetry or extra dimensions [47]. The study of $W^\pm \to \tau^\pm\nu$ production in the $\tau^\pm_{\rm had}\nu$ final state is an important contribution to tau–physics studies at the LHC. Besides testing the Standard Model, $W^\pm \to \tau^\pm\nu$ is an important background process to several searches for new physics. In particular it is the main irreducible background to the search for charged Higgs bosons in the $\tau^\pm\nu$ final state.

4.2 W-boson Production and Decays

In proton-proton collisions W-bosons are mainly produced via the weak Drell-Yan process consisting of the quark-anti-quark annihilation:

$$u + \bar{d} \;\; \to \;\; W^+, \tag{4.1}$$

$$\bar{u} + d \;\rightarrow\; W^-,$$

where u and d denote the up and down quarks, respectively. The actual weak eigenstate d' that is associated with the weak interaction is a combination of the down and the strange quark, quantified by the Cabibbo mixing angle $\eta_C = 13.4°$.

In addition to three valence quarks, protons contain virtual quark-antiquark pairs known as sea quarks, that are formed from the gluons of the protons color field and are generally less energetic. W-boson production in proton-proton collisions requires at least one sea anti-quark. Due to the presence of two valence u quarks in the proton, there is an overall excess of W^+ over W^- bosons.

Theoretical prediction of the W boson production cross section is determined from the parton-parton cross section, where the interaction probabilities are affected by the momentum distribution of the patrons within the proton, described by parton distribution functions. W-boson production cross section has been calculated to NNLO in perturbative QCD and to NLO in electroweak vertices.

W bosons are unstable particles that decay to a pair of quarks or to a charged lepton and a neutrino. The partial decay width for the single leptonic decay channel can be found as

$$\Gamma(W \to \ell\bar{\nu}_\ell) = \frac{G_F}{\sqrt{2}} \frac{M_W^3}{6\pi} = 0.23\,\text{GeV}, \tag{4.2}$$

where G_F is the Fermi constant and M_W is the mass of a W-boson. An assumption is made that the mass of a lepton is negligible in comparison to the W-boson mass. In this limit lepton universality holds – the coupling is the same for every fermion. Branching fractions to the quark–antiquark final state are enhanced by a factor of three due to three different color charges.

4.3 Trigger

$W \to \tau\nu$ candidate events are triggered requiring the presence of a single tau–jet plus missing transverse energy (E_T^{miss}). Two versions of this "cross–channel" trigger with different E_T^{miss} thresholds (20 and 25 GeV) were used during the 2010 data–taking period, due to the need to keep the trigger rate in bandwidth restrictions, when the instantaneous luminosity delivered by the LHC increased.

Both versions of the $\tau_{\text{had}} + E_T^{\text{miss}}$ trigger are seeded by a Level 1 (L1) tau object that is reconstructed based on calorimeter information. In order to increase the trigger efficiency, jets not passing the tau object selection at L1, but passing a higher E_T threshold, are also considered as seeds. Events passing the L1 seed conditions are processed by the High Level Trigger (HLT), which evaluates a refined trigger decision in multiple stages. In the first stage (L2), the tau–jet candidate is reconstructed again, still purely based on calorimeter information, but on the full detector read–out. Tau–jet candidates are required to have $E_T > 20$ GeV and $|\eta| < 3.0$ and to satisfy a calorimeter based isolation criterion: $\sum E_T < 5$ GeV , computed by summing energy deposits in

the ECAL within an annulus of outer (inner) radius $\delta R = 0.50$ (0.15) around the tau direction. The missing transverse energy in the event is computed by summing energy deposits in calorimeters and is required to exceed the E_T^{miss} threshold of the trigger. In the next stage (L2.5), tracks are reconstructed from hits in the Pixel detector, and a track of $p_T > 15$ GeV matching the direction of the tau–jet candidate within $\delta R = 0.20$ is required. The final trigger decision of the last (L3) stage is based on track based tau isolation: there must be no tracks of $p_T > 1$ GeV within an annulus of outer (inner) radius $\delta R = 0.50$ (0.15) around the direction of the tau candidate.

4.3.1 Trigger efficiency

The precision with which the efficiency of the $\tau_{\text{had}} + E_T^{\text{miss}}$ trigger is modeled by the Monte Carlo simulation is verified by comparison to data. The efficiency of τ_{had} and E_T^{miss} conditions in the "cross–channel" trigger are checked independently, using different event samples. It can be verified by Monte Carlo studies that the efficiency for a $W \to \tau\nu$ event to pass the $\tau_{\text{had}} + E_T^{\text{miss}}$ trigger factorizes into independent terms for the τ_{had} and E_T^{miss} legs.

The efficiency of a τ_{had} to pass the τ_{had} requirements of the trigger is checked using a sample of $Z \to \tau^+\tau^- \to \mu\tau_{\text{had}}$ events, triggered by single muon trigger. The efficiency to pass the E_T^{miss} conditions is measured in samples of $W \to e\nu$ events, triggered by single electron trigger and in QCD events, triggered by jet triggers. The trigger efficiencies of τ_{had} and E_T^{miss} legs measured in data are compared to Monte Carlo expectations in Fig. 4.1.

As the comparison of trigger efficiencies in data and Monte Carlo simulation indicates no difference, the trigger efficiency for $W \to \tau\nu$ events is estimated by Monte Carlo simulation.

The uncertainty on the efficiency of the $\tau_{\text{had}} + E_T^{\text{miss}}$ "cross–channel" trigger is dominated by the statistical uncertainty of the $Z \to \tau^+\tau^- \to \mu\tau_{\text{had}}$ sample selected in data. We propagate the statistical uncertainties of individual calo–jet p_T bins into an uncertainty on the $W \to \tau\nu$ trigger efficiency by fitting the efficiency measured in data by a Gaussian error function. The resulting fit parameter values plus uncertainties are used to compute upper and lower bounds for the τ_{had} trigger efficiency as a function of calo–jet p_T. The uncertainty on the $W \to \tau\nu$ trigger efficiency is then obtained by taking the difference between upper and lower bounds to the central value of the fit, averaged over the calo–jet p_T distribution, expected for $W \to \tau\nu$ signal events after all analysis cuts are applied. The value obtained amounts to about 15%. The same procedure is applied to estimate the uncertainty on the trigger efficiency of the E_T^{miss} leg. The event statistics of the $W \to e\nu$ and QCD samples is sufficiently large to yield small uncertainties, amounting to about 2%. Performed fits are illustrated in Fig. 4.2.

Additional component of the uncertainty on the $\tau_{\text{had}} + E_T^{\text{miss}}$ trigger efficiency is related to the choice of binning plus fitting function. The corresponding uncertainties are estimated by repeating the fit using a different binning and replacing the Gaussian

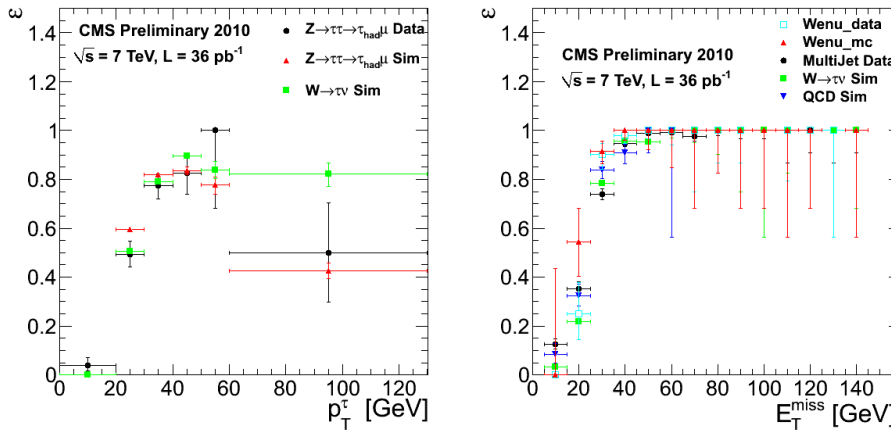

Figure 4.1: Efficiencies of τ_{had} (left) and E_T^{miss} (right) legs of the $\tau_{\text{had}} + E_T^{\text{miss}}$ "cross–channel" trigger. The trigger efficiency of the τ_{had} (E_T^{miss}) leg is parametrized by the p_T of the offline reconstructed calorimeter jet corresponding to the tau–jet candidate (offline reconstructed calo–E_T^{miss}).

error function by the integral of the Crystal ball function. The effect of using a different binning (fitting function) amounts to about 2%. Adding all described uncertainties in quadrature gives a combined relative uncertainty on the trigger efficiency of 15%.

4.4 Event Selection

$W \to \tau_{\text{had}}\nu$ candidate events are selected by requiring:

- The event to pass the $\tau + E_T^{\text{miss}}$ trigger path described in section 4.3.
- An event vertex with $\geq$ 4 DoF, reconstructed within $-24 < z_{vtx} < +24$ cm and $|\rho| < 2$ cm, where ρ denotes the distance between reconstructed vertex and beam–spot position in the transverse plane.
- A τ_{had} candidate with $p_T^{\tau} > 30$ GeV and $|\eta_{\tau}| < 2.3$, reconstructed by the HPS tau identification algorithm, and passing the HPS "medium" isolation discriminator: no charged hadrons of $p_T > 0.8$ GeV and no photons of $E_T > 0.8$ GeV, reconstructed by the PF algorithm and not identified as hadronic tau decay products, are required within a cone of size $\Delta R = 0.5$ around the τ_{had} direction. Additionally, the τ_{had} candidate is required to contain at least one charged hadron of $p_T > 15$ GeV and to pass the discriminators against muons and electrons [48].

In case of choosing separate W^+ and W^- samples, a cut fixing the tau charge is added.

- The missing transverse energy reconstructed in the event to satisfy PF–$E_T^{\text{miss}} > 30$ GeV. We add Calo–$E_T^{\text{miss}} > 25$ GeV requirement in order to ensure that a tighter selection is applied offline than at the trigger level.

- The event not to contain any muon or electron of $p_T^{\ell} > 15$ GeV. An identified muon is required to be within the geometrical acceptance of $|\eta| < 2.4$, to be identified as a global muon and to be isolated. An identified electron is required to satisfy $|\eta| < 2.5$, a set of electron identification criteria detailed in [49] and isolation requirement.

  The isolation of electrons and muons is computed by summing the transverse momenta of tracks reconstructed in the silicon pixel plus strip detectors and the energy measured in the electromagnetic and hadronic calorimeters of CMS. The sum is computed within a cone of size $\Delta R = \sqrt{(\Delta\eta)^2 + (\Delta\phi)^2} = 0.3$ around the lepton direction:

$$I = \frac{\sum_{\text{tracks}} p_T + \sum_{\text{ECAL}} E_T + \sum_{\text{HCAL}} E_T}{p_T^{\ell}},$$

  wher ℓ is an electron or muon. Electrons (muons) are considered isolated if $I < 0.09(0.2)$. Energy deposits and track associated with the lepton itself are excluded from the isolation sum.

- The ratio of p_T of the τ_{had} candidate to the scalar sum of transverse momenta of the jets with $p_T > 15$ GeV and $|\eta| < 3$ reconstructed in the event (R_{HT}) to satisfy $R_{\text{HT}} < 0.65$.

- The transverse mass, M_T, of τ_{had} candidate plus missing transverse energy:

$$M_T = \sqrt{(P_T^{\tau} + E_T^{miss})^2 - \left((P_x^{\tau} + E_x^{miss})^2 + (P_y^{\tau} + E_y^{miss})^2\right)}$$

  to satisfy $M_T > 40$ GeV.

The aim of the cuts on R_{HT} and M_T is to remove QCD background.

4.5 Background Estimation

Background contributions to the sample of $W \to \tau_{\text{had}}\nu$ candidate events passing the selection criteria described in section 4.4 are due to QCD multi–jet events and electroweak (EWK) backgrounds: $W \to e\nu$, $W \to \mu\nu$ and $Z \to \tau^+\tau^-$. The estimate for the dominant background, QCD, which is also the background most difficult to model by the Monte Carlo simulation, is obtained from data by combining two complementary methods: the "template method" and the "ABCD" method. The contribution of EWK backgrounds is obtained by the Monte Carlo simulation.

4.5.1 QCD Background Estimation by Template Method

The idea of the template method is to determine the contribution of signal plus background processes to the sample of $W \to \tau_{\mathrm{had}}\nu$ candidate events selected in data via a fit of distributions observed in data with a set of "template" histograms. Each template histogram is normalized to unit area and represents the shape of the distribution expected for one particular signal or background processes. The contributions of signal plus background processes to the event sample selected in data is then obtained by the normalization factors obtained by the best fit of all template shapes to the distribution observed in data.

The choice of observable which gets used in the template fit is made based on the level of discrimination between the signal and background processes provided by the observable: Good separation between the template shapes causes the normalization factors to be well constrained by the fit, yielding small uncertainties on the signal and background contributions to the event sample selected in data.

We have chosen *MET-topology* to be the template fit observable used in the $W \to \tau_{had}\nu$ analysis. *MET-topology* is defined as the ratio between the P_T sum of PF–candidates projected in the E_T^{miss} direction to the P_T sum of PF–candidates projected opposite to the direction of E_T^{miss}. For signal events we expect very little activity in direction of E_T^{miss} and thus small values of *MET-topology*. QCD multi–jet background events have usually higher values of *MET-topology*, even after passing a PF–$E_T^{miss} >$ 30 GeV cut, as QCD events are intrinsically balanced and the reconstructed E_T^{miss} typically results from a mismeasurement of one (or more) of the jets in the event.

The shape templates for the $W \to \tau_{\mathrm{had}}\nu$ signal and EWK background processes are taken from the Monte Carlo simulation. The template for the QCD background is obtained from data, using a control region. The control region is chosen such that a high purity QCD sample is acquired, while the shape of the *MET-topology* distribution in the control region represents the distribution of QCD events passing the selection criteria described in section 4.4.

With respect to the selection of $W \to \tau_{\mathrm{had}}\nu$ candidate events, the QCD enriched control region is defined by inverting the isolation requirement of the τ_{had} candidate. The independence of the *MET-topology* template shape to such change is illustrated in Figure. 4.3, where *MET-topology* distributions after passing or failing the τ_{had} isolation requirement are compared in the QCD enriched region, which is chosen by loosening the cuts by $R_{\mathrm{HT}} > 0.6$ and $E_T^{\mathrm{miss}} > 25$ GeV.

The vetos against additional electrons or muons in the event are tightened by lowering the p_T^{ℓ} threshold to 8 GeV . We extract the QCD background contribution by independent fits both for the inclusive $W \to \tau_{\mathrm{had}}\nu$ event selection and separately for $W^+ \to \tau^+_{\mathrm{had}}\nu$ and $W^- \to \tau^-_{\mathrm{had}}\nu$ selection. The number of events in the selected QCD enriched templates and contamination expected from EWK backgrounds and the $W \to \tau_{\mathrm{had}}\nu$ signal are given in Tab. 4.1. The purity of QCD events selected in the QCD enriched control region is expected to be about 70%.

The signal and background yields obtained by fitting the *MET-topology* shapes for

Process	Contribution		
	W selection	W^+ selection	W^- selection
Data	1274	697	577
$W \to e\nu$	30.7	17.0	13.7
$W \to \mu\nu$	20.2	10.3	9.9
$Z \to \tau^+\tau^-$	24.9	12.4	12.5
$W \to \tau\nu$	317.8	178.3	139.5

Table 4.1: Number of events selected in the QCD enriched control sample and expected contamination from EWK backgrounds and the $W \to \tau^{\pm}_{\rm had}\nu$ signal for $W^+ \to \tau^+_{\rm had}\nu$, $W^- \to \tau^-\nu$ and inclusive $W \to \tau_{\rm had}\nu$ event selection.

$W \to \tau_{had}\nu$, QCD and EWK backgrounds to the *MET-topology* distribution observed in data are given in Tab.4.2. A Gaussian constraint is used in the fit, constraining the normalization factors for EWK backgrounds to values within ±50% with respect to the yield expected from Monte Carlo simulation.

Process	Estimate		
	W fit	W^+ fit	W^- fit
QCD	165 ± 24[1]	93± 19[2]	102±19[3]
$W \to e\nu$	52 ± 24	33±14	15 ± 10
$W \to \mu\nu$	4.8 ± 2.4	3.1±1.5	1.8 ± 0.9
$Z \to \tau\tau$	55 ± 25	28±12	23± 14
$\sum$ backgrounds	277	157	121

Before applying the correction detailed in section 4.5.1 of the appendix:
[1] 231 ± 28 events.
[2] 130 ± 21 events.
[3] 136 ± 23 events.

Table 4.2: Normalization factors for background processes obtained by the template fit.

The sum of signal and background templates scaled by the normalization factors

obtained by the fit is compared to the *MET-topology* distribution observed in the sample of $W \to \tau_{\mathrm{had}}\nu$ candidate events selected in data in Fig. 4.4. The distributions observed in data are fitted well by the sum of templates.

Correcting the QCD Yield Obtained by the Template Fit

The contamination from EWK background and from the $W \to \tau_{had}\nu$ signal process to the control region from which the shape template for the QCD multi–jet background is obtained causes the estimate for the QCD background contribution obtained by the fit to be biased and needs to be corrected for.

The basic idea for deriving the correction formula is to relate the "true" QCD event yield, N_{QCD}, in the signal region from which the cross–section is extracted to the normalization factor $N_{\mathrm{QCD}}^{\mathrm{fit}}$ obtained by the template fit, taking the purity p of the QCD shape template into account:

$$N_{\mathrm{QCD}} = N_{\mathrm{QCD}}^{\mathrm{fit}} \cdot p. \tag{4.3}$$

The true purity p is given by

$$p = \frac{N_{\mathrm{QCD}}^{\mathrm{C}}}{N_{\mathrm{QCD}}^{\mathrm{C}} + N_{\mathrm{EWK}}^{\mathrm{C}} + N_{W\to\tau\nu}^{\mathrm{C}}} \tag{4.4}$$

where $N_{\mathrm{QCD}}^{\mathrm{C}}$, $N_{\mathrm{EWK}}^{\mathrm{C}}$ and $N_{W\to\tau\nu}^{\mathrm{C}}$ denote the contribution to the control region from QCD, EWK backgrounds and the $W \to \tau_{\mathrm{had}}\nu$ signal, respectively. $N_{\mathrm{QCD}}^{\mathrm{C}}$ is determined by subtracting from the number of data events selected in the control region the expected contributions from EWK backgrounds and the $W \to \tau_{\mathrm{had}}\nu$ signal:

$$p = 1 - \frac{N_{\mathrm{EWK}}^{\mathrm{C}} + N_{W\to\tau\nu}^{\mathrm{C}}}{N_{\mathrm{data}}^{\mathrm{C}}}. \tag{4.5}$$

$N_{\mathrm{EWK}}^{\mathrm{C}}$ is taken from the Monte Carlo simulation. The difficulty is that $N_{W\to\tau\nu}^{\mathrm{C}}$ needs to be assumed unknown, since the $W \to \tau\nu$ cross–section is what we wish to measure.

The $N_{W\to\tau\nu}^{\mathrm{C}}$ can be related to the $W \to \tau\nu$ event yield, $N_{W\to\tau\nu}$, in the signal region:

$$N_{W\to\tau\nu}^{\mathrm{C}} = r \cdot N_{W\to\tau\nu}, \tag{4.6}$$

where the extrapolation factor r represents the ratios of $W \to \tau\nu$ selection efficiencies in control region to signal region. r does not depend on the $W \to \tau_{had}\nu$ cross–section and is taken from the Monte Carlo simulation.

Substituting relation (4.6) first into equation (4.5) and then equation (4.5) into (4.3), and expressing the $W \to \tau\nu$ event yield in the signal region by $N_{W\to\tau\nu} = N_{\mathrm{data}} - (N_{\mathrm{QCD}} + N_{\mathrm{EWK}})$, we obtain:

$$N_{\mathrm{QCD}} = N_{\mathrm{QCD}}^{\mathrm{fit}} \cdot \left(1 - \frac{N_{\mathrm{EWK}}^{\mathrm{C}} + r \cdot (N_{\mathrm{data}} - (N_{\mathrm{QCD}} + N_{\mathrm{EWK}}))}{N_{\mathrm{data}}^{\mathrm{C}}}\right). \tag{4.7}$$

Solving this equation for N_{QCD} yields the formula which we use for correcting the QCD background estimate obtained by the template fit:

$$N_{\mathrm{QCD}} = N_{\mathrm{QCD}}^{\mathrm{fit}} \cdot \frac{N_{\mathrm{data}}^{\mathrm{C}} - N_{\mathrm{EWK}}^{\mathrm{C}} - r \cdot (N_{\mathrm{data}} - N_{\mathrm{EWK}})}{N_{\mathrm{data}}^{\mathrm{C}} - r \cdot N_{\mathrm{QCD}}^{\mathrm{fit}}}. \tag{4.8}$$

The corrected value for the QCD background contribution to the sample of $W \to \tau_{\mathrm{had}}\nu$ candidate events passing the selection criteria described in section 4.4 amounts to 165 ± 24 events for inclusive $W \to \tau_{\mathrm{had}}\nu$ sample. The EWK background contributions determined by the template fit are in agreement with the Monte Carlo expectation. The full results are summarized in table 4.2

4.5.2 QCD Background Estimation by ABCD Method

ABCD method provides a very useful tool for data-driven background estimation. In case we are able to find two uncorrelated observables x and y for background events, information from three background enriched sideband regions can be used to estimate the background contribution in the signal region. This means that the probability density function of the background $\rho(x, y)$ can be factorized:

$$\rho(x, y) = f(x)g(y). \tag{4.9}$$

It can be shown that the expectation values of the four regions fulfill the relation:

$$\frac{\lambda_A}{\lambda_B} = \frac{\lambda_C}{\lambda_D}, \tag{4.10}$$

where λ_X can be interpreted as parameters of the Poisson distributions. For just one measurement λ_X can be estimated by the event counts $\lambda_X = N_X$ in the corresponding regions and the estimation of background events in the signal region becomes straightforward:

$$N_A = N_B \cdot \frac{N_C}{N_D}. \tag{4.11}$$

The contribution of QCD multi–jet background to the sample of $W \to \tau_{had}\nu$ candidate events (signal region A) is estimated via extrapolation of event yields measured in three sidebands (B, C and D). The method utilizes two uncorrelated observables, E_T^{miss} and R_{HT} and define the four regions by:

- signal region A: $R_{\mathrm{HT}} > 0.65$, $E_T^{\mathrm{miss}} > 30$ GeV .
- sideband B: $R_{\mathrm{HT}} > 0.65$, $E_T^{\mathrm{miss}} < 30$ GeV
- sideband C: $R_{\mathrm{HT}} < 0.65$, $E_T^{\mathrm{miss}} < 30$ GeV
- sideband D: $R_{\mathrm{HT}} < 0.65$, $E_T^{\mathrm{miss}} > 30$ GeV .

Provided that there is no correlation between E_T^{miss} and R_{HT}, the number of QCD events contributing to the signal region A can be estimated from Eq. (4.11). Fig. 4.5 demonstrates that the correlation between E_T^{miss} and R_{HT} is indeed low.

Equation 4.11 can be used directly to estimate the QCD background contribution in signal region A, in case the contributions from EWK backgrounds and from the $W \to \tau_{\text{had}}\nu$ signal in the sidebands B, C and D is zero. Monte Carlo simulation predicts that the sum of contributions from EWK backgrounds plus $W \to \tau_{\text{had}}\nu$ signal amounts to about 1% in region C, 6% in region B and 15% in region D, respectively, *cf.* Tab. 6.2. The expected contributions of processes other than QCD are subtracted from the number of events selected in the regions B, C and D before equation 4.11 is applied. The resulting estimate for the QCD event yield in signal region A is $N_A = 203 \pm 26$ events for inclusive $W \to \tau_{\text{had}}\nu$ event selection, $N_A = 105.2 \pm 14.9$ events for $W^+ \to \tau^+_{\text{had}}\nu$ event selection and $N_A = 100.2 \pm 12.3$ events for $W^- \to \tau^-_{\text{had}}\nu$ event selection. These results are compatible with the estimates obtained via the template method.

	Data	$W \to \tau_{\text{had}}\nu$	$W \to \mu\nu$	$W \to e\nu$	$Z \to \tau\tau$
region A	764 ±27.6	531.3 ±5.7	6.4 ±0.7	41.1 ±1.6	52.7 ±1.3
region B	2248 ±47.4	94.3 ±2.4	0.3 ±0.1	5.4 ±0.6	18.7 ±0.8
region C	35460 ±188.3	181.8 ±3.3	1.3 ±0.3	7.2 ±0.7	74.4 ±1.6
region D	4020 ±63.4	465.2 ±5.3	7.1 ±0.7	27.6 ±1.3	71.4 ±1.5

Table 4.3: Number of events observed in signal region A and sidebands B, C and D for data, $W \to \tau_{\text{had}}\nu$ signal and EWK backgrounds

The quoted uncertainty represents the sum of statistical plus systematic uncertainties, added in quadrature. The systematic uncertainties have been obtained by varying the amount of EWK background subtracted from regions B, C and D by 40% and varying the amount of subtracted $W \to \tau_{\text{had}}\nu$ signal by $^{+25.8}_{-25.1}\%$ *cf.* section 4.6.

4.5.3 Combined Estimate of Background Contributions

The QCD background estimates obtained by template and ABCD method are compatible within uncertainties. As discussed, the uncertainties of both template and ABCD method are composed of statistical and systematic uncertainties. Since the control regions that are used by the two methods are chosen based on different variables, the statistical uncertainties can be considered to be uncorrelated. The systematic uncertainties of the two methods are correlated however, and we have conservatively assumed full correlation.

The 2×2 covariance matrix for the two measurements can be written as follows:

$$(V)_{ij} = \langle \delta N_i \delta N_j \rangle, \tag{4.12}$$

where δN_i and δN_j are the standard deviations of the number of QCD events, predicted by template method or ABCD method.

The best estimate of the combined QCD background contribution along with its standard deviation are given in general form as:

$$\begin{aligned} \overline{N} &= \sum_i \omega_i N_i, \\ \sigma^2_{\overline{N}} &= \omega_i \omega_j (V)_{ij}, \end{aligned} \tag{4.13}$$

where ω_i denotes the weight of a particular measurement and satisfies a relation $\sum_i \omega_i = 1$.

Minimizing σ^2 yields the solution of the weights for the two QCD estimates as follows:

$$\omega_i = \frac{\sum_k (V^{-1}_{\overline{N}})_{ik}}{\sum_{jk} (V^{-1}_{\overline{N}})_{jk}}. \tag{4.14}$$

Substituting equation 4.14 back to relations 4.13 gives the best estimate for the combined QCD background contribution. The results for the samples of $W \to \tau_{\mathrm{had}}\nu$, $W^+ \to \tau^+_{\mathrm{had}}\nu$ and $W^- \to \tau^-_{\mathrm{had}}\nu$ candidate events are given in Tab. 4.4, together with the Monte Carlo predictions for EWK background contributions.

Channel	QCD	$\sum$ EWK	Total
$W \to \tau\nu$	187 ± 20	110 ± 22	297 ± 30
$W^+ \to \tau^+\nu$	101 ± 14	59 ± 12	160 ± 18
$W^- \to \tau^-\nu$	101 ± 12	55 ± 12	155 ± 17

Table 4.4: Estimates for QCD background and EWK background contributions.

4.6 Systematic Uncertainties

Systematic uncertainties affecting the measurement of the $W \to \tau\nu$ cross–section are due to uncertainties on the efficiency of the $\tau_{\mathrm{had}} + E_T^{\mathrm{miss}}$ trigger, the τ_{had} identification efficiency, uncertainties on the energy scale of tau–jets and other jets in the event, theoretical uncertainties and uncertainties on the integrated luminosity of the analyzed dataset.

The trigger efficiency is measured with an uncertainty of 15%, as described in section 4.3.1.

The efficiency for identifying hadronic tau decays is measured from a fit to a $Z \to \tau\tau$ sample with an uncertainty of 7% [46].

The energy scale of tau–jets is known with an uncertainty of 3% [48]. The energy scale of quark and gluon jets is determined from an analysis of the p_T balance between photons and recoil jets in γ + jets events [50]. Jet energy scale uncertainties depend on jet p_T and η and are applied to jets of $p_T > 10$ GeV . Jets of $p_T < 10$ GeV and particles of low p_T which are not included in any jet ("unclustered energy") are attributed a more conservative uncertainty of 10%.

Signal efficiency and acceptance are determined using $W \to \tau\nu$ Monte Carlo simulated events. The effect of energy scale uncertainties on the efficiency to pass the event selection criteria is estimated by varying the energy of tau–jets, quark/gluon jets and the "unclustered energy" within their respective uncertainties, re–reconstructing the event after each variation and reevaluating all event selection criteria. The event yield is compared to the nominal value and the difference is taken as systematic uncertainty. The effect of the 3% tau–jet energy scale uncertainty on the $W \to \tau\nu$ event yield amounts to $^{+16.0}_{-14.8}$%. The effect is rather large, as an upward (downward) variation of the tau–jet energy scale simultaneously increases (decreases) the efficiency to pass $\tau_{\rm had}$ p_T, $E_T^{\rm miss}$ and $R_{\rm HT}$ cuts. Variation of the jet energy scale has the opposite effect: an upward (downward) variation decreases (increases) the efficiencies to pass the E_T^{miss} and $R_{\rm HT}$ cuts. We conservatively assume that $\tau_{\rm had}$ and jet energy scales are uncorrelated and obtain an uncertainty on the $W \to \tau\nu$ event yield due to the jet energy scale uncertainty of $^{+10.0}_{-10.1}$%, which we add in quadrature to the effect of the τ_{had} energy scale uncertainty.

Theoretical uncertainties due to parton–distribution functions (PDFs), that are used during the Monte Carlo simulation, are estimated following the PDF4LHC recommendations [51] and amount to 4%.

The integrated luminosity of the analyzed dataset is measured with an uncertainty of 4% [52].

The systematic uncertainties on the QCD background estimate via template method are determined by varying the shape templates of the $W \to \tau_{\rm had}\nu$ signal and of EWK backgrounds within the tau and jet energy scale uncertainties, and by varying the yields of EWK backgrounds when accounting for the 30% expected impurity in the control region from which the QCD shape template is obtained. The combined uncertainty on the background contributions amounts to about 10%, as discussed in Sect. 4.5.

The uncertainties on the electroweak background contributions obtained from the Monte Carlo simulation are estimated by varying the trigger efficiency by 15%, the energy scale of jets within the jet energy scale uncertainty, the $e \to \tau_{had}$ fake–rate by 20% [48] and the $\mu \to \tau_{had}$ fake–rate by 75%. The resulting relative uncertainty is 29% (38%) for $W \to e\nu$ ($W \to \mu\nu$) events and 30% for $Z \to \tau\tau$ events. The quoted uncertainties include the uncertainties on the $W \to \ell\nu$ and $Z \to \ell\ell$ cross sections measured by CMS [53].

For the measurement of $W^+ \to \tau^+_{\rm had}\nu$ and $W^- \to \tau^-_{\rm had}\nu$ cross–sections, which depend on the reconstruction of the tau charge, we consider $W \to \tau_{\rm had}\nu$ events in which the τ_{had} charge is misidentified as background. The charge misidentification amounts to about

1%. The τ_{had} charge misidentification uncertainty is measured using $Z \to \tau\tau$ candidate events.

Tab. 4.5 summarizes the systematic uncertainties considered in the $W \to \tau\nu$ cross section measurement.

Source	Uncertainty
Trigger efficiency	15%
Tau–jet energy scale	$^{+16.0}_{-14.8}$%
Jet energy scale	$^{+10.0}_{-10.1}$%
PDF	4%
Luminosity	4%
Background contributions	10.1%
$\sum$ Systematic Uncertainties	$^{+25.8}_{-25.1}$%

Table 4.5: Effect of systematic uncertainties on the $W \to \tau\nu$ cross section measurement.

4.7 Cross–section Extraction

The cross–section for $W \to \tau_{\text{had}}\nu$ production is determined by the number of signal events N_{sig}, the integrated luminosity $\mathcal{L}$ of the analyzed dataset, signal acceptance A and signal selection efficiency ε according to the following relation:

$$\sigma = \frac{N_{\text{sig}}}{\mathcal{L} \cdot A \cdot \varepsilon}. \tag{4.15}$$

The number of signal events N_{sig} is determined by subtracting the expected contribution of EWK plus QCD backgrounds from the number of $W \to \tau_{\text{had}}\nu$ candidate events, passing the selection criteria described in section 4.4.

The signal acceptance is defined to be the fraction of $W \to \tau_{\text{had}}\nu$ signal events in which the W boson decays into a tau–jet with $p_T > 30$ GeV and $|\eta| < 2.3$ plus a neutrino with $p_T > 30$ GeV on generator level. An additional generator level cut fixing the charge of τ_{had} is applied for defining the individual acceptances with respect to $W^+ \to \tau^+_{\text{had}}\nu$ and $W^- \to \tau^-_{\text{had}}\nu$ datasets. The signal acceptance is obtained from the Monte Carlo simulation and is quoted relative to the branching fraction for tau leptons to decay hadronically [17]:

$$BR(\tau \to \tau_{\text{had}}) = 0.648. \tag{4.16}$$

The signal selection efficiency ε is defined as a fraction of $W \to \tau_{had}\nu$ events within signal acceptance that pass the selection criteria described in section 4.4 and it is

obtained from the Monte Carlo simulation. The values of acceptance and efficiency are summarized in Table 4.6 separately for inclusive W, W^+ and W^- hadronic tau decays.

Channel	A/BR	ε
$W \to \tau_{\rm had}\nu$	0.0790± 0.0002(stat.)	0.0332 ± 0.0006(stat.)
$W^+ \to \tau^+_{\rm had}\nu$	0.0773 ± 0.0004(stat.)	0.0333 ± 0.0009(stat.)
$W^- \to \tau^-_{\rm had}\nu$	0.0820 ± 0.0004(stat.)	0.0331± 0.0009(stat.)

Table 4.6: Efficiency and acceptance.

The τ_{had} identification efficiency predicted by the Monte Carlo simulation depends on the hadronization model used. We have compared signal acceptance and selection efficiency for $D6T$ and $Z2$ tunes of the hadronization model implemented in PYTHIA and find the difference to be within the 7% systematic uncertainty discussed in section 4.6. The quoted signal acceptance and selection efficiency represent the average of $D6T$ and $Z2$ values.

4.8 Results

The number of observed $W \to \tau\nu$ candidate events ($N_{\rm obs}$) and the estimated number of signal events ($N_{\rm sig}$), obtained by subtracting QCD and EWK background contributions, are presented in Tab. 4.7.

Fig. 4.6 shows the transverse mass observed in the sample of $W \to \tau_{\rm had}\nu$ candidate events compared to the expected sum of signal plus background processes. Distributions of various kinematic observables reconstructed in the selected events are displayed in the Appendix.

Channel	$N_{\rm obs}$	$N_{\rm sig}$
$W \to \tau_{\rm had}\nu$	793	496 ± 30
$W^+ \to \tau^+_{\rm had}\nu$	444	284 ± 18
$W^- \to \tau^-_{\rm had}\nu$	349	194 ± 17

Table 4.7: Number of $W \to \tau\nu$ candidate events passing the selection criteria described in Sect. 4.4 and estimated number of signal events obtained by subtraction of the background contributions given in Tab. 4.4.

The measured cross–sections for $W \to \tau\nu$, $W^+ \to \tau^+\nu$ and $W^- \to \tau^-\nu$ production in pp collisions at $\sqrt{s} = 7$ TeV center–of–mass energy are given in Tab. 4.8 and are in agreement with theory predictions, computed at next–to–next–to–leading order (NNLO), and with the $W \to e\nu$ and $W \to \mu\nu$ cross–sections measured by CMS [53].

Channel	$\sigma(pp \to WX) \times \mathcal{B}$ (nb)	NNLO (nb)
$W \to \tau\nu$	$8.96 \pm 0.51(\text{stat.})^{+2.32}_{-2.26}(\text{syst.}) \pm 0.36(\text{lumi.})$	10.44 ± 0.52
$W^+ \to \tau^+\nu$	$5.26 \pm 0.39(\text{stat.})^{+1.36}_{-1.29}(\text{syst.}) \pm 0.21(\text{lumi.})$	6.15 ± 0.29
$W^- \to \tau^-\nu$	$3.40 \pm 0.33(\text{stat.})^{+0.92}_{-0.93}(\text{syst.}) \pm 0.14(\text{lumi.})$	4.29 ± 0.23

Table 4.8: Production cross section measurements and theoretical predictions

The ratio of $W^+ \to \tau^+\nu$ to $W^- \to \tau^-\nu$ cross–sections is measured to be:

$$R_{+/-} = \frac{\sigma(pp \to WX) \times \mathcal{B}(W^+ \to \tau^+\nu)}{\sigma(pp \to WX) \times \mathcal{B}(W^- \to \tau^-\nu)} = 1.55 \pm 0.19(\text{stat.})^{+0.11}_{-0.13}(\text{syst.}), \qquad (4.17)$$

which is in agreement with the NNLO theory prediction of 1.43 ± 0.04 based on various parton distribution functions [54, 55].

Examples of the event displays of the $W \to \tau\nu$ candidate events in the CMS detector are shown in Figs. 4.7 and 4.8 for one-prong and three-prong τ_{had} candidates, respectively.

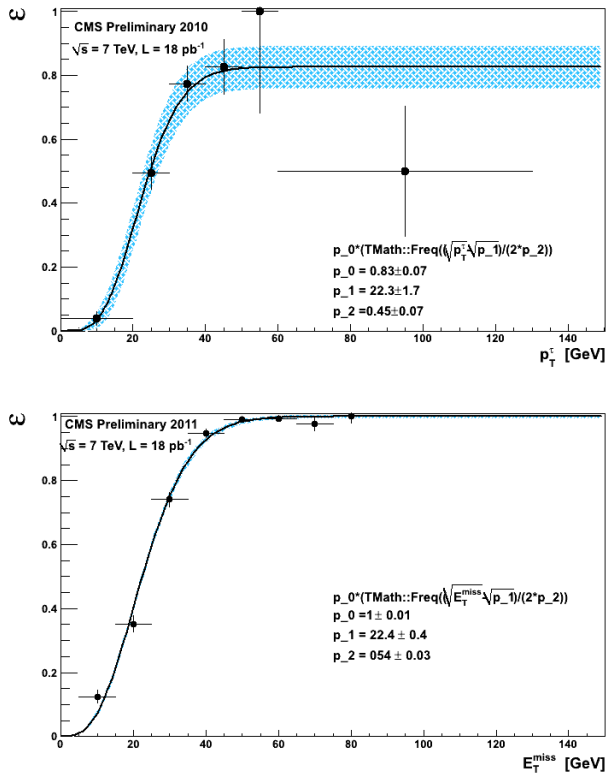

Figure 4.2: Top: Efficiency of the τ_{had} leg measured in $Z \to \tau^+\tau^- \to \mu\tau_{\text{had}}$ events selected in data compared to the fit by a Gaussian error function. The shaded area indicates uncertainties on the trigger efficiency arising from limited event statistics in the $Z \to \tau^+\tau^- \to \mu\tau_{\text{had}}$ sample. Bottom: Efficiency of the E_T^{miss} leg measured in QCD events. Uncertainties on the trigger efficiency are illustrated by a shaded area. In case of the E_T^{miss} leg, the error band is too narrow to be visible.

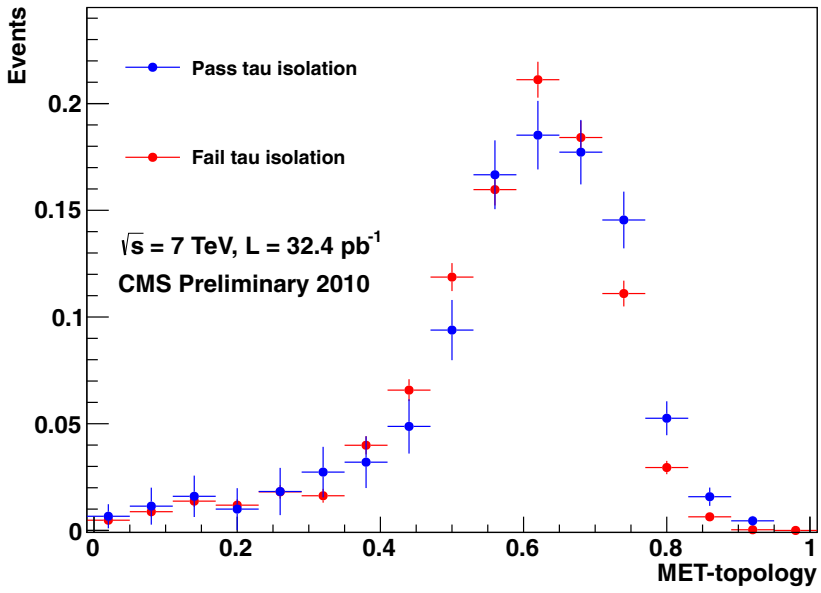

Figure 4.3: The comparison of *MET-topology* shape distributions observed in data in the QCD-enriched region after passing(failing) the τ_{had} isolation requirement.

(a)

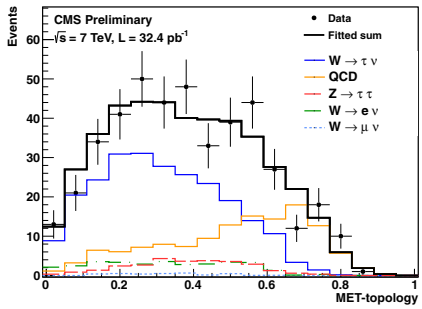

(b)

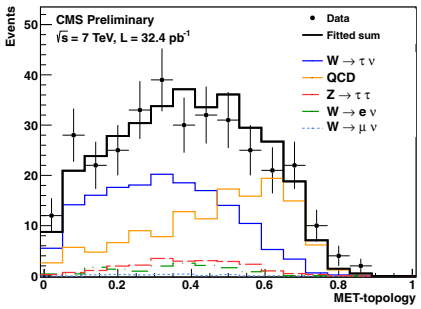

(c)

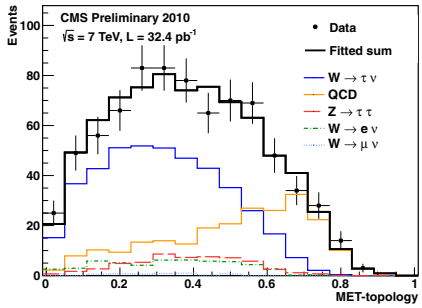

Figure 4.4: *MET-topology* distribution observed in data compared to sum of shape templates scaled by normalization factors determined by the fit for $W^+ \to \tau^+_{\mathrm{had}}$ selection (a), $W^- \to \tau^-_{\mathrm{had}}\nu$ selection (b) and inclusive $W \to \tau_{\mathrm{had}}\nu$ selection (c).

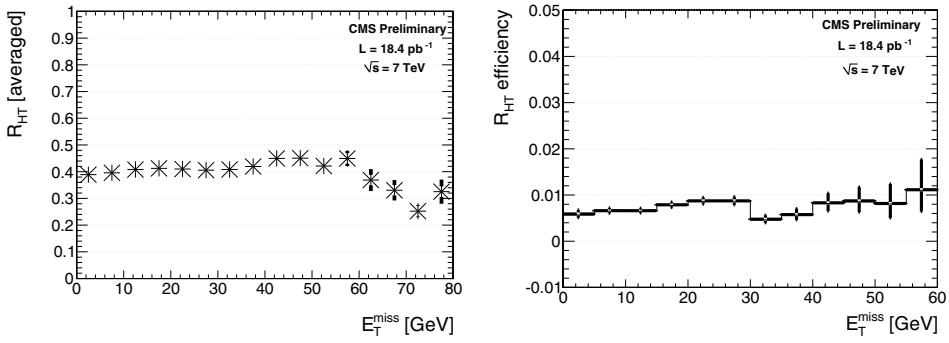

Figure 4.5: Average value of R_{HT} (left) and fraction of events passing $R_{\mathrm{HT}} > 0.65$ cut (right) in different bins of E_T^{miss}. The events shown in the plots are selected in data and are required to pass all selection criteria described in section 4.4, except E_T^{miss} and R_{HT}, which are both not applied.

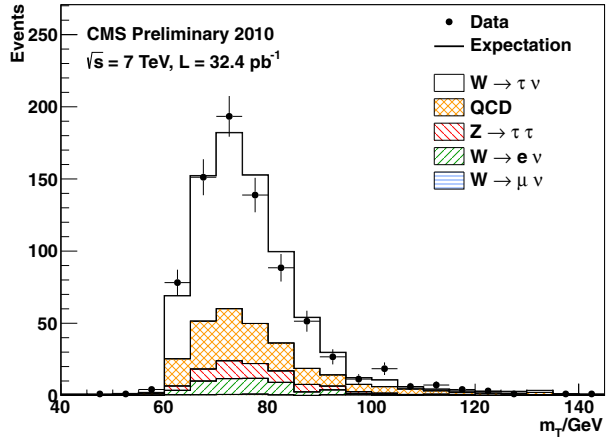

Figure 4.6: Distribution of transverse mass in the selected $W \to \tau_{\mathrm{had}}\nu$ candidate events compared to the expected sum of signal and background processes. The $W \to \tau_{\mathrm{had}}\nu$ signal is scaled according to the measured cross–section, EWK backgrounds according to the Monte Carlo expectation and QCD background to the yield determined from data.

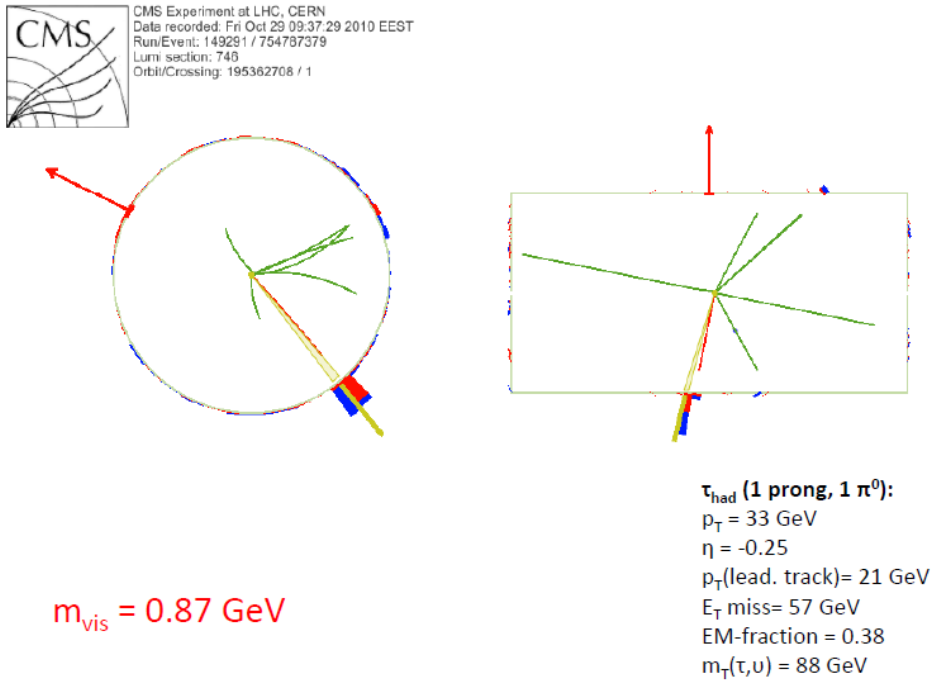

Figure 4.7: A selected one-prong τ_{had} candidate

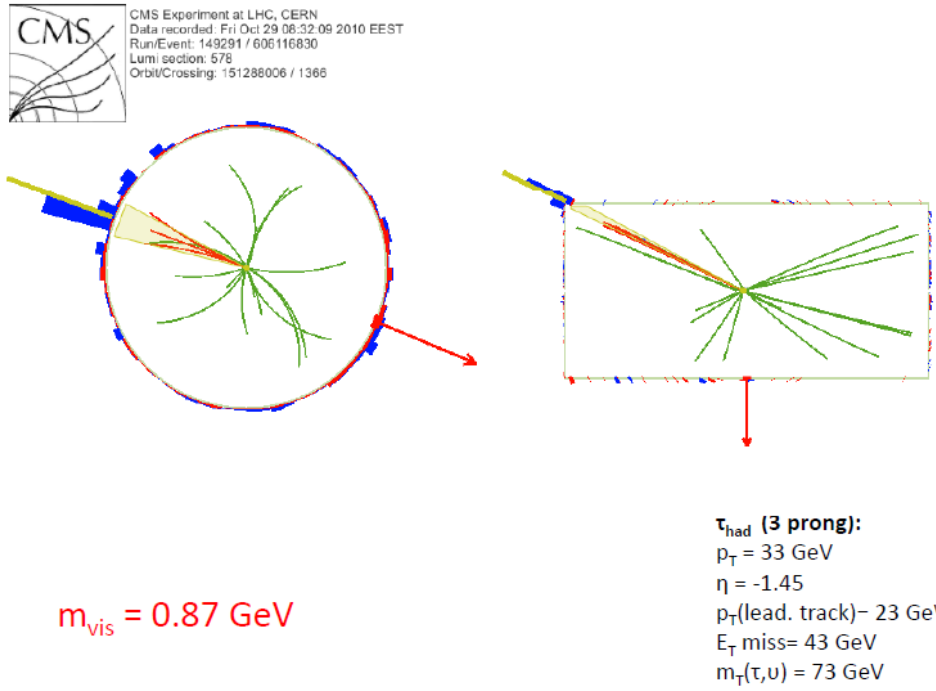

Figure 4.8: A selected three-prong τ_{had} candidate

Chapter 5

Search for a Doubly Charged Higgs Boson – Motivation and Phenomenology

5.1 Introduction

The existence of non-zero neutrino masses is a firmly established signal of physics beyond the standard model. Despite intense efforts over many decades, the origin of neutrino masses is still unknown. One of the best motivated neutrino mass mechanisms is the type II seesaw model [56, 57, 58, 59], which is realized with a triplet scalar field with the $SU(2)_L \times U(1)_Y$ quantum numbers $\Phi \sim (3, 2)$. The triplet scalar field contains a doubly charged component $\Phi^{\pm\pm}$ that can be pair-produced at particle colliders. The production cross section is determined from gauge interactions and is limited only by the $\Phi^{\pm\pm}$ mass and not by the Yukawa couplings. Thus the experimental tests of this model are limited only by the collision energy. Neutrino masses in this scenario are Majorana type and the Yukawa couplings to the triplet may be sizable, being constrained only by the non-observation of lepton flavor violating interactions.

The observation of a doubly charged scalar particle in the LHC experiment would establish the see-saw mechanism of type II as the most promising framework generating mass to neutrinos.

5.2 Phenomenological Setup

In the type II seesaw model a complex scalar $SU(2)_L$ triplet field Φ is added to the SM Lagrangian. In the 2×2 representation Φ can be written in a form

$$\Phi = \begin{pmatrix} \Phi^+/\sqrt{2} & \Phi^{++} \\ \Phi^0 & -\Phi^+/\sqrt{2} \end{pmatrix}, \tag{5.1}$$

where Φ^0, $\Phi^\pm$ and $\Phi^{\pm\pm}$ are the neutral, singly charged and doubly charged scalar fields, respectively.

The most general $SU(2)_L \times U(1)_Y$ invariant Higgs potential involving the SM Higgs doublet field φ and the Higgs triplet field Φ has a form [60]

$$V = \mu^2(\varphi^\dagger\varphi) + \lambda(\varphi^\dagger\varphi) + M_\Phi^2 \mathrm{Tr}(\Phi^\dagger\Phi) + \lambda_1[\mathrm{Tr}(\Phi^\dagger\Phi)]^2 + \lambda_2 \mathrm{Det}(\Phi^\dagger\Phi)^2 \qquad (5.2)$$
$$+\lambda_3(\varphi^\dagger\varphi)\mathrm{Tr}(\Phi^\dagger\Phi) + \lambda_4(\varphi^\dagger\tau_i\varphi)\mathrm{Tr}(\Phi^\dagger\tau_i\Phi) + \left(\frac{1}{\sqrt{2}}\mu_1(\varphi^T i\tau_2\Phi^\dagger\varphi) + \mathrm{h.c}\right),$$

where M_Φ is the mass of the triplet scalar fields and the choice $\mu^2 < 0$ ensures the spontaneous electroweak symmetry breaking, as discussed in Section 1.1.5. The minimization of the potential in Eq. (5.2) leads nonzero vacuum expectation value of the scalar triplet

$$v_\Phi \simeq \frac{\mu_1 v^2}{2M_\Delta^2 + (\lambda_3+\lambda_4)v^2}, \quad \text{for} \quad v_\Phi \ll v. \qquad (5.3)$$

Φ couples to leptons via the Lagrangian

$$\mathcal{L} = u\bar{\ell}_{Li}^C \tau_2 Y_\Phi^{ij}(\tau\cdot\Phi)\ell_{Li} + h.c., \qquad (5.4)$$

where $(Y_\Phi)_{ij}$ are the Yukawa couplings of the triplet to the lepton generations $i,j = e,\mu,\tau$. When Φ is assigned two units of the lepton number $L = 2$, the presence of the term $\mu_1(\varphi^T i\tau_2\Phi^\dagger\varphi)$ in the Lagrangian explicitly breaks the lepton number conservation.

The scalar potential in Eq. (5.2) and the triplet Yukawa interaction term Eq. (5.4) give a working model of neutrino mass generation: when the neutral component of the scalar triplet acquires a non-zero vacuum expectation value v_Φ, the neutrino mass matrix is generated by

$$(m_\nu)_{ij} = 2(Y_\Phi)_{ij} v_\Phi. \qquad (5.5)$$

The Lagrangian (5.2) gives rise to seven physical Higgs fields. Two doubly charged fields coincide with the doubly charged components of the scalar triplet $\Phi^{\pm\pm}$. Two singly charged fields $H^\pm$ and three neutral fields H^0, A^0 and h^0 are in general mixtures of doublet and triplet fields with the mixing parameter proportional to the ratio v_Φ/v. Due to the smallness of v_Φ/v, the mixing is negligibly small and the fields $H^\pm, H^0$ and A^0 are predominantly composed of the triplet fields, while h^0 corresponds to the SM Higgs boson. The masses of the triplet scalar fields are of the order M_Φ with mass splittings of the order $\lambda_4 v_\Phi$.

5.3 $\Phi^{\pm\pm}$ Production and Decay Channels

$\Phi^{\pm\pm}$ couples to charged leptons, electroweak vector-bosons (W and Z), and other components of the scalar triplet (Φ^0 and $\Phi^\pm$). At hadron colliders, such as the LHC, $\Phi^{\pm\pm}$ can be produced via Drell-Yan pair-production ($pp \to \Phi^{++}\Phi^{--}$) or associated production along with the singly charged component of the triplet scalar ($pp \to \Phi^{\pm\pm}\Phi^{\mp}$).

$\Phi^{\pm\pm}$ can decay either to two same-charge leptons, to a pair of same-charge W-bosons or to a $\Phi^{\pm}$ and a W-boson. The latter two are kinematically limited, as the mass of $\Phi^{\pm\pm}$ has to be at least as large as the sum of its decay products. Thus the decay to a pair of W-bosons would require the mass of $\Phi^{\pm\pm}$ to be at least about 160 GeV and the decay $\Phi^{\pm\pm} \to W^{\pm}\Phi^{\pm}$ is kinematically allowed only if the mass separation between $\Phi^{\pm\pm}$ and $\Phi^{\pm}$ is sufficiently large. $W^{\pm}\Phi^{\pm}$ final state is not considered further, as it is natural to assume that the masses of the triplet components are nearly degenerate.

The decay widths for the leptonic decay channels depend only on the Yukawa couplings and the doubly charged Higgs boson mass:

$$\Gamma_{ij} \equiv \Gamma(\Phi^{\pm\pm} \to \ell_i^{\pm}\ell_j^{\pm}) = \begin{cases} \frac{1}{8\pi}|(Y_\Phi)_{ii}|^2 m_{\Phi^{\pm\pm}} & i = j, \\ \\ \frac{1}{4\pi}|(Y_\Phi)_{ij}|^2 m_{\Phi^{\pm\pm}} & i \neq j, \end{cases} \tag{5.6}$$

where $i, j = e, \mu\tau$ denote the lepton generations. The decay width to WW channel is proportional to the scalar triplet vacuum expectation value

$$\begin{aligned} \Gamma_{WW} &\equiv \Gamma(\Phi^{\pm\pm} \to W^{\pm}W^{\pm}) \\ &= \frac{2v_\Phi^2 m_{\Phi^{\pm\pm}} m_{W^{\pm}}^2}{\pi v_0^4}\left(\frac{3m_{W^{\pm}}^2}{m_{\Phi^{\pm\pm}}^2} + \frac{m_{\Phi^{\pm\pm}}^2}{4m_{W^{\pm}}^2} - 1\right)\left(1 - \frac{4m_{W^{\pm}}^2}{m_{\Phi^{\pm\pm}}^2}\right)^{1/2} \\ &= k v_\Phi^2. \end{aligned} \tag{5.7}$$

The branching fractions of the $\Phi^{\pm\pm}$ are given by

$$\begin{aligned} \mathrm{BR}(\Phi^{\pm\pm} \to \ell_i^{\pm}\ell_j^{\pm}) &= \frac{\Gamma_{ij}}{\Gamma_{\mathrm{tot}}}, \\ \mathrm{BR}(\Phi^{\pm\pm} \to W^{\pm}W^{\pm}) &= \frac{\Gamma_{WW}}{\Gamma_{\mathrm{tot}}}. \end{aligned} \tag{5.8}$$

where $\Gamma_{tot} = \sum_{ij}\Gamma_{ij} + \Gamma_{WW}$.

The branching fraction to WW channel depends on v_Φ and the mass of the scalar triplet. v_Φ is constrained to have a value between 1 eV and 1 GeV, where the lower bound comes from the naturalness of neutrino masses and the upper bound from the precision measurements of the ρ-parameter. Figure 5.1 illustrates the relative contributions of $\Phi^{\pm\pm}$ branching fractions to leptonic and WW channels for different $\Phi^{\pm\pm}$ masses. Up to v_Φ values of about 10^{-5} GeV the leptonic decay modes dominate. This is followed by a smooth increase of the WW decay mode contribution. Starting from about $v_\Phi \approx 10^{-3}$ GeV $\Phi^{\pm\pm}$ decays to WW channel are dominant.

Feynman diagrams for Drell-Yan pair-production and associated production, assuming $\Phi^{\pm\pm}$ to decay leptonically, are shown in Figure 5.2.

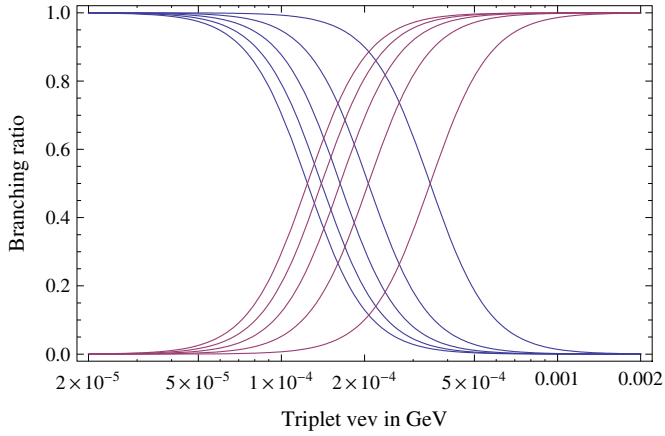

Figure 5.1: $\Phi^{\pm\pm}$ branching fractions for different values of $\Phi^{\pm\pm}$ mass and v_Φ. The blue lines represent leptonic decays and the red lines the decay to the WW channel. Different lines denote various values of $\Phi^{\pm\pm}$ masses (lower mass corresponds to higher v_Φ for transition)

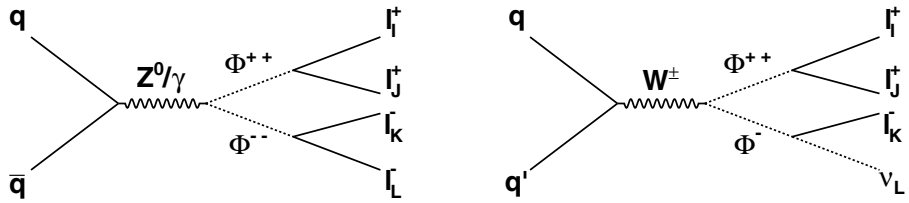

Figure 5.2: Feynman diagrams for pair and associated production of $\Phi^{\pm\pm}$,

5.4 $\Phi^{\pm\pm}$ Leptonic Branching Fractions and Neutrino Parameters

The $\Phi^{\pm\pm}$ decays to same-charge lepton pairs $\Phi^{\pm\pm} \to \ell\ell'$, $\ell, \ell' = e, \mu, \tau$ provide a clear signal at LHC. In addition, the flavor dependence of leptonic decays is directly related to the Majorana mass matrix of the neutrinos, thus providing an interesting possibility to acquire information about neutrino parameters by measuring the $\Phi^{\pm\pm}$ leptonic branching fractions.

If we assume relatively small values of v_Φ and degenerate masses of triplet components, then the branching fractions to $\Phi^{\pm}W^{\pm}$ and $W^{\pm}W^{\pm}$ channels are negligible and the connection between leptonic branching fractions and the neutrino mass matrix can

be derived from Eqs. (5.5), (5.6) and (5.8)

$$\mathrm{BR}(\Phi^{\pm\pm} \to \ell^{\pm}\ell'^{\pm}) = \frac{|(m_\nu)_{ij}|^2}{\sum_{i\geq j}|(m_\nu)_{ij}|^2}. \tag{5.9}$$

The Majorana mass matrix m_ν has ten free parameters: two mass differences Δm^2_{12} and Δm^2_{23}, sign(Δm_{23}), which determines the neutrino mass hierarchy, mass of the lowest neutrino mass eigenstate m_0, three mixing angles θ_{12}, θ_{23} and θ_{13} and three CP-violating phases α_1, α_2 and δ. The neutrino mass differences Δm^2_{12} and Δm^2_{23} have been measured with a good precision in the neutrino oscillation experiments. The values of the mixing angles have larger uncertainties and in the following we have chosen to fix them according to the tribimaximal model [61]. It has been proposed that the existing data from neutrino oscillations approximately point to a specific form of the lepton mixing matrix with effective bimaximal mixing of ν_μ and ν_τ and effective trimaximal mixing between ν_e and ν_μ. The tribimaximal mixing predicts

$$\sin^2\theta_{12} = \frac{1}{3}, \qquad \sin^2\theta_{23} = \frac{1}{2}, \qquad \sin^2\theta_{13} = 0. \tag{5.10}$$

The recent measurement of the non-zero value of θ_{13} [62, 63] only applies a small correction to the structure of the branching fractions.

After fixing the values of the mass differences and mixing angles, we can write an equation system of six independent equations that relates branching fractions of six different $\Phi^{\pm\pm}$ leptonic decay channels with unknown neutrino parameters,

$$\mathrm{BR}_{ij} = f_k(m_0, \mathrm{sign}(\Delta m_{23}), \alpha_1, \alpha_2, \delta). \tag{5.11}$$

In order to make the reasoning independent of possible contributions from $\Phi^{\pm\pm} \to W^{\pm}W^{\pm}$ and $\Phi^{\pm\pm} \to H^{\pm}W^{\pm}$ decay channels, the ratios of branching fractions are considered instead of their absolute values, reducing the number of independent equations to five.

For neutrino mass hierarchy and the lowest neutrino mass determination a dimensionless parameter can be derived from the equation system (5.8) that connects $\Phi^{\pm\pm}$ leptonic branching fractions to neutrino masses and is independent of the Majorana phases,

$$C \equiv \frac{2\mathrm{BR}_{\mu\mu} + \mathrm{BR}_{\mu\tau} + \mathrm{BR}_{ee}}{\mathrm{BR}_{ee} + \mathrm{BR}_{e\mu}} = \frac{-m_1^2 + m_2^2 + 3m_3^2}{2m_1^2 + m_2^2}. \tag{5.12}$$

The mass hierarchy is determined by the measurement of C as follows:

- $C > 1$ – normal mass hierarchy,
- $C < 1$ – inverted mass hierarchy,
- $C \approx 1$ – degenerate masses.

The lowest neutrino mass m_0 can be determined after the mass hierarchy measurement by substituting the mass differences to Eq. (5.12). Determination is limited by the experimental sensitivity for very small and nearly degenerate masses.

Figure 5.3 illustrates the dependency of $\Phi^{\pm\pm}$ branching fractions on the lightest neutrino mass for the normal and inverted mass hierarchies. A real mixing matrix has been assumed, fixing the Majorana phases α_1 and α_2 to zero. Majorana phases mainly influence the contribution of the $e\mu$ and $e\tau$ channels, that have only vanishingly small contributions for $\alpha_1 = \alpha_2 = 0$ and can considerably increase with the nonzero values. The branching fraction to the ee channel is the best characteristic for the mass hierarchy determination that varies greatly depending on the mass hierarchy and the lowest neutrino mass. The ee branching fraction is negligible in the case of normal mass hierarchy, while it is the dominant decay channel for the inverted mass hierarchy. If the mass of the lightest state increases, both the normal and inverted hierarchies lead almost the same distribution of branching ratios, $\Phi^{\pm\pm}$ decays to the ee, $\mu\mu$ and $\tau\tau$ channels with nearly equal probabilities while the decays to other channels are negligible. This indicates degenerate masses.

The measurement of Majorana phases depends on the neutrino mass hierarchy. Three characteristic scenarios can be considered:

- Normal mass hierarchy with $m_1 = 0$. $\Phi^{\pm\pm}$ branching fractions are independent of α_1, α_2 can be determined.
- Inverted mass hierarchy with $m_3 = 0$. $\Phi^{\pm\pm}$ branching fractions are independent of absolute values of Majorana phases, $\Delta\alpha = |\alpha_1 - \alpha_2|$ can be determined.
- Degenerate masses $m_1 \approx m_2 \approx m_3 \equiv m$.

In the case of normal mass hierarchy, all $\Phi^{\pm\pm}$ decay channels that involve electrons (ee, $e\mu$ and $e\tau$) are negligible. The distribution of branching fractions is shown in Figure 5.4. Nonzero α_2 only causes a small increase in the $\mu\tau$ decay channel, while decays to the $\mu\mu$ and $\tau\tau$ channels are proportionally reduced. The changes in branching fractions are symmetrical with respect to $\alpha_2 = \pi$

For inverted mass hierarchy the $\Phi^{\pm\pm}$ branching fractions as functions of $\Delta\alpha$ are presented in Figure 5.5. Nonzero $\Delta\alpha$ induces branching fractions to $e\mu$ and $e\tau$ channels, that can occupy more than 80% of all leptonic decays in the case of $\Delta\alpha = \pi$ and are absent in the case of $\Delta\alpha = 0$.

In the case of nearly degenerate neutrino masses $m_1 \approx m_2 \approx m_3 \equiv m$ the $\Phi^{\pm\pm}$ branching fractions are independent of m and the expressions that relate neutrino parameters and $\Phi^{\pm\pm}$ branching fractions significantly simplify. The requirement of tri-bimaximal mixing angles can be dropped. Small values of θ_{13} are assumed, only considering the leading order terms in the expansion. The behavior of $\Phi^{\pm\pm}$ branching fractions is illustrated in Figure 5.6 that shows the results for both $\alpha_1 = 0$ and $\alpha_1 = \alpha_2$.

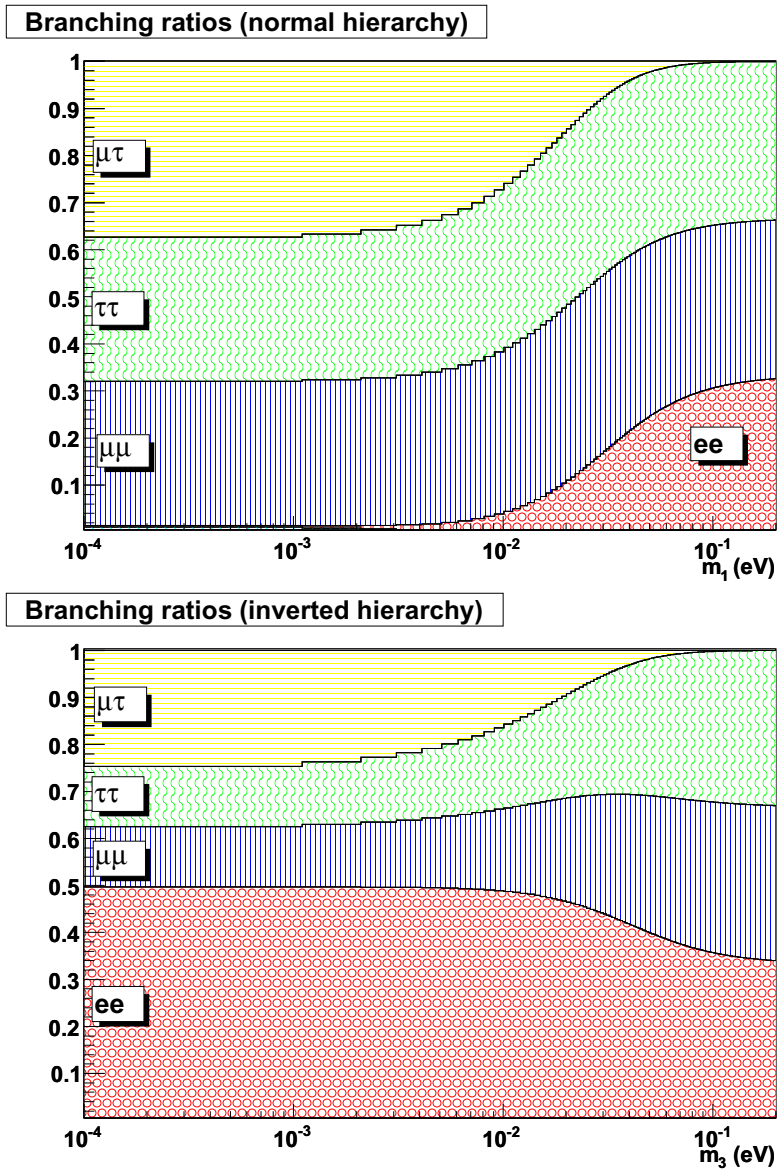

Figure 5.3: Distribution of the $\Phi^{\pm\pm}$ leptonic branching ratios as a function of the lightest neutrino mass. The left (right) panel corresponds to the normal (inverted) mass hierarchy. For nearly degenerate masses the two possibilities imply almost the same result.

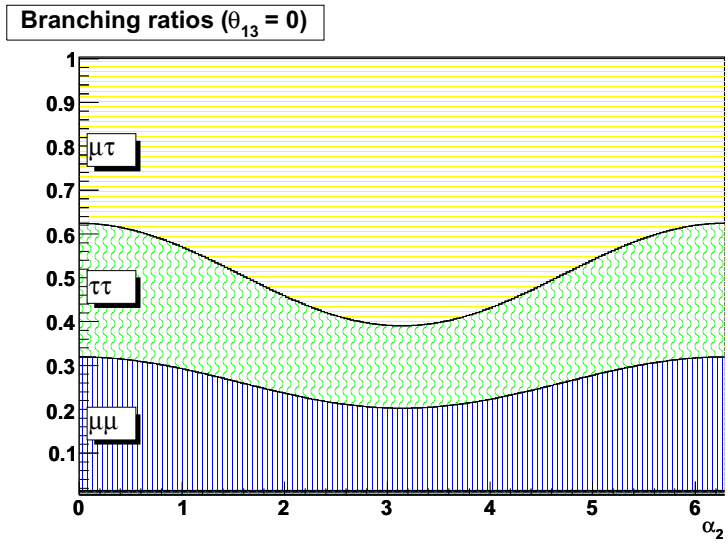

Figure 5.4: Distribution of the $\Phi^{\pm\pm}$ leptonic branching fractions as a function of α_2. Normal mass hierarchy, $m_1 = 0$ and tri-bimaximal neutrino mixing angles are assumed

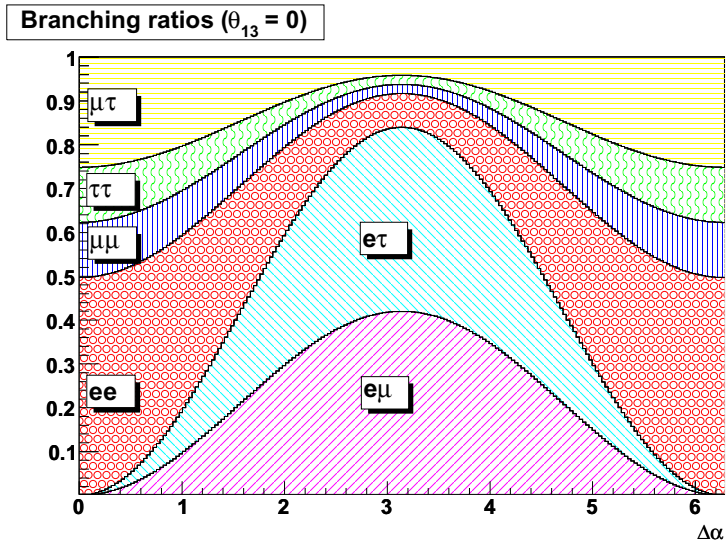

Figure 5.5: Distribution of the $\Phi^{\pm\pm}$ leptonic branching ratios as a function of $\Delta\alpha$. Inverted mass hierarchy, $m_3 = 0$ and tri-bimaximal neutrino mixing angles are assumed

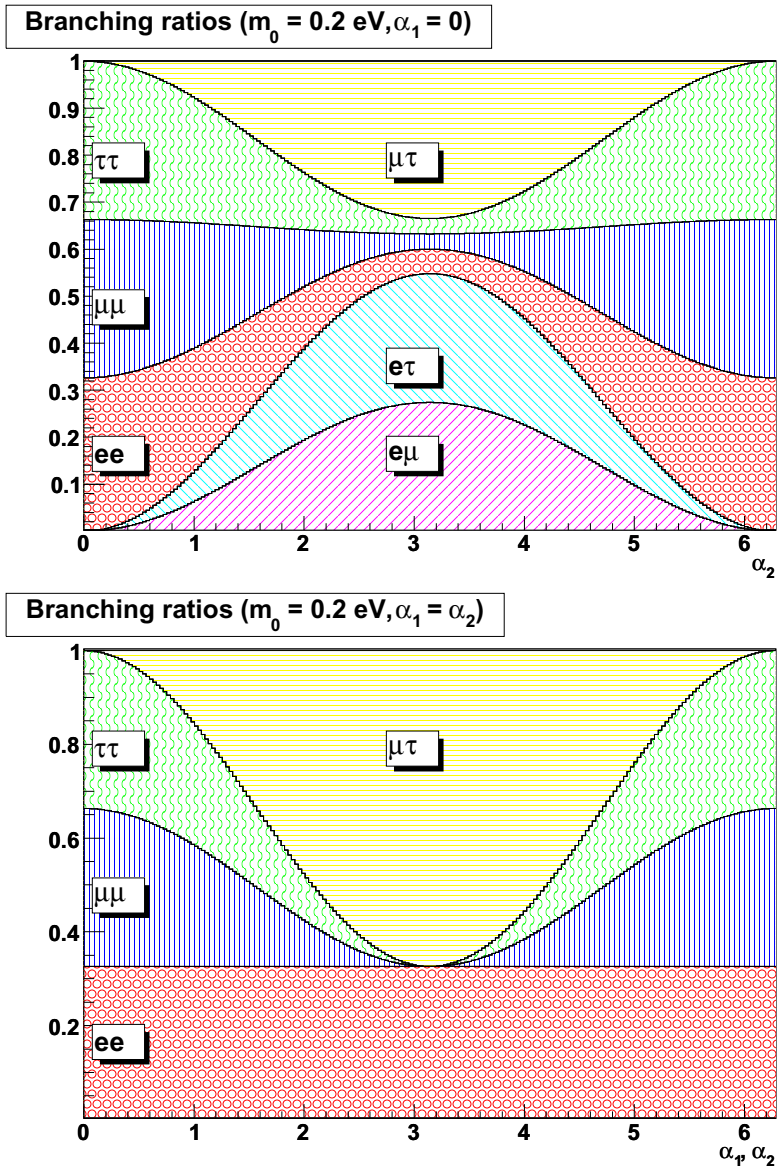

Figure 5.6: Distribution of the $\Phi^{\pm\pm}$ leptonic branching fractions for $\alpha_2 = 0$ (up) and $\alpha_1 = \alpha_2$ (down). Degenerate mass hierarchy and tri-bimaximal neutrino mixing angles are assumed

Chapter 6

Search for a Doubly Charged Higgs boson in $\Phi^{\pm\pm} \to \tau\tau$ Decay Channel

6.1 Introduction

The $\Phi^{\pm\pm}$ has been searched previously in various leptonic decay channels by LEP and Tevatron experiments and in 4μ final state in the ATLAS experiment. The lower limits on the $\Phi^{\pm\pm}$ mass were set between 112 GeV and 355 GeV, depending on the decay channel [64, 65, 66]. The mass limit for the $\Phi^{\pm\pm} \to \tau\tau$ decay channel is the least constrained, since the analysis is affected by the presence of multiple neutrinos in the final state.

An inclusive and most recent search for a doubly-charged Higgs boson in all leptonic decay channels has been performed at CMS experiment [67]. Part of the inclusive search – the analysis of $\Phi^{\pm\pm} \to \tau\tau$ decay channel – is summarized in detail in this chapter. The search is based on data corresponding to an integrated luminosity of 4.93 ± 0.11 fb^{-1} that was collected during the 2011 running period. Both the pair-production process $pp \to \Phi^{\pm\pm}\Phi^{\pm\pm} \to \ell^{\pm}\ell^{\pm}\ell^{\mp}\ell^{\mp}$ [68, 69] and the associated production process $pp \to \Phi^{\pm\pm}\Phi^{\mp} \to \ell^{\pm}\ell^{\pm}\ell^{\mp}$ [70] are studied. The mass degeneracy of $\Phi^{\pm\pm}$ and $\Phi^{\pm}$ is assumed; however, this requirement impacts only the cross section, as long as the mass splitting is such that the cascade decays are kinematically disfavored. The production cross sections at LHC are shown in Figure 6.1.

The search strategy is to identify an excess of events in same-charge pairs of leptons. Final states containing three or four charged leptons are considered, including at most one and two hadronically-decaying τ-leptons (τ_{had}), respectively. $\Phi^{\pm\pm} \to W^{\pm}W^{\pm}$ decays are assumed to be suppressed.

6.2 MC Simulation

The multi-purpose Monte Carlo (MC) event generator PYTHIA6 [71] is used for the simulation of signal and background processes, either to generate a given hard pro-

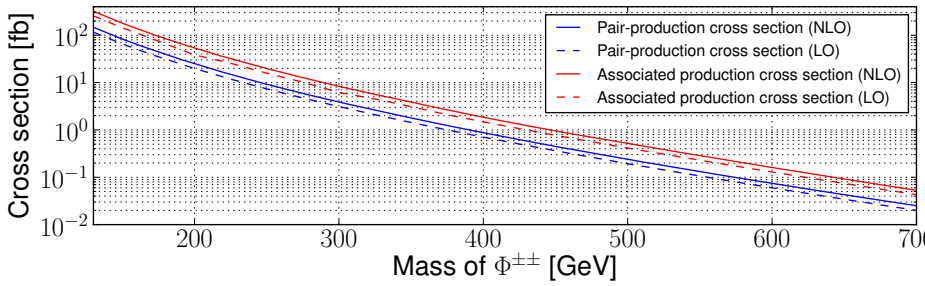

Figure 6.1: Production cross sections for pair and associated production processes of $\Phi^{\pm\pm}$ at $\sqrt{s} = 7$ TeV [69].

cess at leading order (LO), or for the simulation of showering and hadronization in cases where the hard processes are generated at next-to-leading order (NLO). The TAUOLA [72] program is interfaced to PYTHIA 6 for the correct treatment of the τ decay and polarization. Signal samples in the associated production mode are generated using CALCHEP [73]. VV+jets and Drell–Yan events are generated using MADGRAPH [74] and TAUOLA. Samples of $t\bar{t}$+jets and single top production are generated by using POWHEG [75, 76, 77] and PYTHIA 6. All other samples are generated directly within PYTHIA 6.

6.3 Lepton Reconstruction and Identification

6.3.1 Muons

Muon candidates are reconstructed using two algorithms. The first matches tracks in the silicon detector to segments in the muon chambers. The second performs a combined fit using hits in both the silicon tracker and the muon systems [78]. All muon candidates are required to be successfully reconstructed by both algorithms. In addition the following quality requirements are imposed: normalized χ^2 of the global-muon track fit to be less than 10; at least one muon chamber hit to be included in the final track fit; the silicon track to be matched to muon segments in at least two muon stations; and the silicon track to have more than 10 hits, including at least one pixel hit. Finally, muons are required to have $p_T > 5$ and $|\eta| < 2.4$

6.3.2 Electrons

The electron reconstruction uses a cut-based approach in order to reject electrons faked by jets or resulting from conversions. Due to the high magnetic field, as well as the large amount of material in front of the ECAL, electron candidates are separated into

categories according to the amount of bremsstrahlung. During the bremsstrahlung recovery procedure the objects called superclusters are created, which are groups of clusters that collect energy released both by the electron and the emitted photons. Transverse energy (E_T) and η-dependent selections are applied, since the shapes of the discriminating variables depend on both the E_T and η of the electron [79].

Selection criteria for electrons include the following steps: geometrical matching between the position of the energy deposition in the ECAL and the direction of the corresponding electron track; requirements on shower shape; a maximum impact parameter of the electron track; isolation of the electron; and selection criteria to reject photon conversions. Additionally electrons must pass a charge triple check, based on two different track curvature fitting algorithms and the supercluster-pixel angle. Agreement is required between these methods. Additionally, electrons are required to have $p_T > 15$ GeV and $|\eta| < 2.5$

6.3.3 Lepton Isolation

Event selection is based on the relative isolation variable, defined as the sum of the p_T of the tracks in the tracker and the energy from the calorimeters within the isolation cone, divided by the lepton p_T. A typical LHC bunch-crossing at high instantaneous luminosity typically results in many overlapping proton-proton collisions ("pile-up" events). Such pile-up events influence the energy that is deposited within the isolation cone. This effect is compensated using the FastJet energy-density algorithm [80, 81].

6.3.4 Taus

Hadronic tau candidates (τ_{had}) are reconstructed using the HPS algorithm and required to have $p_T > 15$ GeV and $|\eta| < 2.1$. A τ_{had} candidate has to pass the "HPS-medium" isolation discriminator: no charged hadrons of $p_T > 0.8$ GeV and no photons of $E_T > 0.8$ GeV, reconstructed by the PF algorithm and not identified as hadronic tau decay products, are required within a cone size of $\Delta R = 0.5$ around the τ_{had} direction. Additional selection criteria are applied to discriminate against electrons and muons, since these particles could fake 1-prong taus.

6.4 Event Selection

The characteristic signature of $\Phi^{\pm\pm} \to \tau^{\pm}\tau^{\pm}$ is the presence of two same-charge light leptons or tau-jets with a resonant structure in their invariant mass spectrum. The reconstructed mass peak has a relatively large width due to the presence of multiple neutrinos in the final state.

Same-charge backgrounds arise from various SM processes, including di-boson events, Z+jets and $t\bar{t}$ with leptonic W decays. W+jets and QCD multi-jet backgrounds have very large production cross sections, thus a few events might survive the final event

selection criteria. However, the requirement of multiple high-p_T leptons in the final state efficiently suppresses their contribution.

6.4.1 Trigger

Double-lepton (ee, $e\mu$, $\mu\mu$) triggers are used for the initial event selection. p_T thresholds 17 and 8 GeV are applied on two leptons for ee and $e\mu$ triggers for all analyzed events. In the case of the $\mu\mu$ trigger, the muon p_T threshold changed along with the rapid increase of the instantaneous luminosity during the data-taking period. The threshold $p_T > 7$ GeV was applied on each muon for the first few hundred pb^{-1}. The thresholds were first raised to 13 and 8 GeV on the two muons and finally to 17 and 8 GeV, which coincides with the thresholds of other double-lepton triggers. The trigger efficiency is in excess of 99.5% for the events passing the final event selection criteria defined below.

6.4.2 Pre-selection Requirements

In order to select events from well-measured collisions, a primary vertex pre-selection is applied, requiring the number of degrees of freedom for the vertex fit to be greater than 4, and the distance of the vertex from the center of the CMS detector to be less than 24 cm along the beam line and less than 2 cm in the transverse plane. In case of multiple primary vertex candidates, the one with the highest value of the scalar sum of the total transverse momentum of the associated tracks is selected [82].

Recorded and simulated events are preselected by requiring at least two final-state leptons, with $p_T > 20$ GeV and $p_T > 10$ GeV, respectively. If pairs of leptons with invariant mass less than 12 GeV are reconstructed, neither of the particles are considered in the subsequent steps of the analysis. This requirement rejects low-mass resonances and leptons from b-quark decays. Additional background suppression is achieved by requiring the two least well isolated leptons (e and μ) to have summed relative isolation ($\sum RelIso$) less than 0.25.

6.4.3 Final Event Selection

The event sample is divided into two subsets, based on the total number of final state candidate leptons (three or four leptons). The search is performed in various final state light lepton and τ_{had} configurations for a set of pre-determined mass hypotheses of $\Phi^{\pm\pm}$.

A following set of selection criteria is considered for suppressing the background processes:

- A requirement on the scalar p_T sum of the final state light leptons or τ_{had} ($\sum p_T$).
- Rejection of events that contain a leptonically decaying Z-boson by applying a veto on the opposite-sign same-flavor combinations of light leptons, requiring $|m(\ell^+\ell^-) - m_Z| > 80$ GeV if such a combination exists.

- An upper bound on the opening angle, $\Delta\varphi$, between the same-charge light leptons or τ_{had}. Background processes such as the production of a Z-boson recoiling from a jet that is misidentified as lepton yield leptons with a large opening angle with respect to those originating from the Z-boson decay. For a decay of the signal particle, we expect the pair of leptons to be boosted and have smaller opening angle.

- A loose requirement of missing transverse energy E_T^{miss} in three-lepton final state, that helps to further reduce the background contributions, especially Drell-Yan processes.

- A mass window, applied in the three-lepton final state and defined as $[m_\Phi/2 - 20\text{ GeV}; 1.1 \cdot m_\Phi]$

Three-Lepton Final State Including up to One τ_{had}

At the pre-selection level three light leptons or two light leptons and one τ_{had} are required, passing the selection criteria described in Section 6.3. Sizable background contributions survive after applying this selection, including Drell-Yan processes, $t\bar{t}$ and di-boson production. The distributions of the main observables after the preselection are illustrated in Figure 6.2.

The applied selection criteria are summarized in Table 6.1. A wide mass window has been defined in order to keep the signal efficiency high and a mass dependent cut on $\sum p_T$ is applied in order to maximize the signal significance for different mass points. The final di-lepton mass distributions for $m_{\Phi^{\pm\pm}} = 130$ GeV and $m_{\Phi^{\pm\pm}} = 200$ GeV are illustrated in Figure 6.3.

Four-Lepton Final State Including up to Two τ_{had}

Four leptons comprising up to two τ_{had} are required, passing the preselection criteria. The background contributions after the preselection are expected to be considerably smaller, since the requirement of four leptons efficiently reduces the SM backgrounds. The distributions of the main observables after the preselection are illustrated in Figure 6.4.

In order to keep high signal efficiency, the mass window is not defined and all selection criteria are mass-independent. The applied selection criteria are summarized in Table 6.1. Clean signal can be extracted from the backgrounds using the MC simulation and no data events pass the final event selection. The final di-lepton mass distribution for $m_{\Phi^{\pm\pm}} = 200$ GeV is illustrated in Figure 6.5.

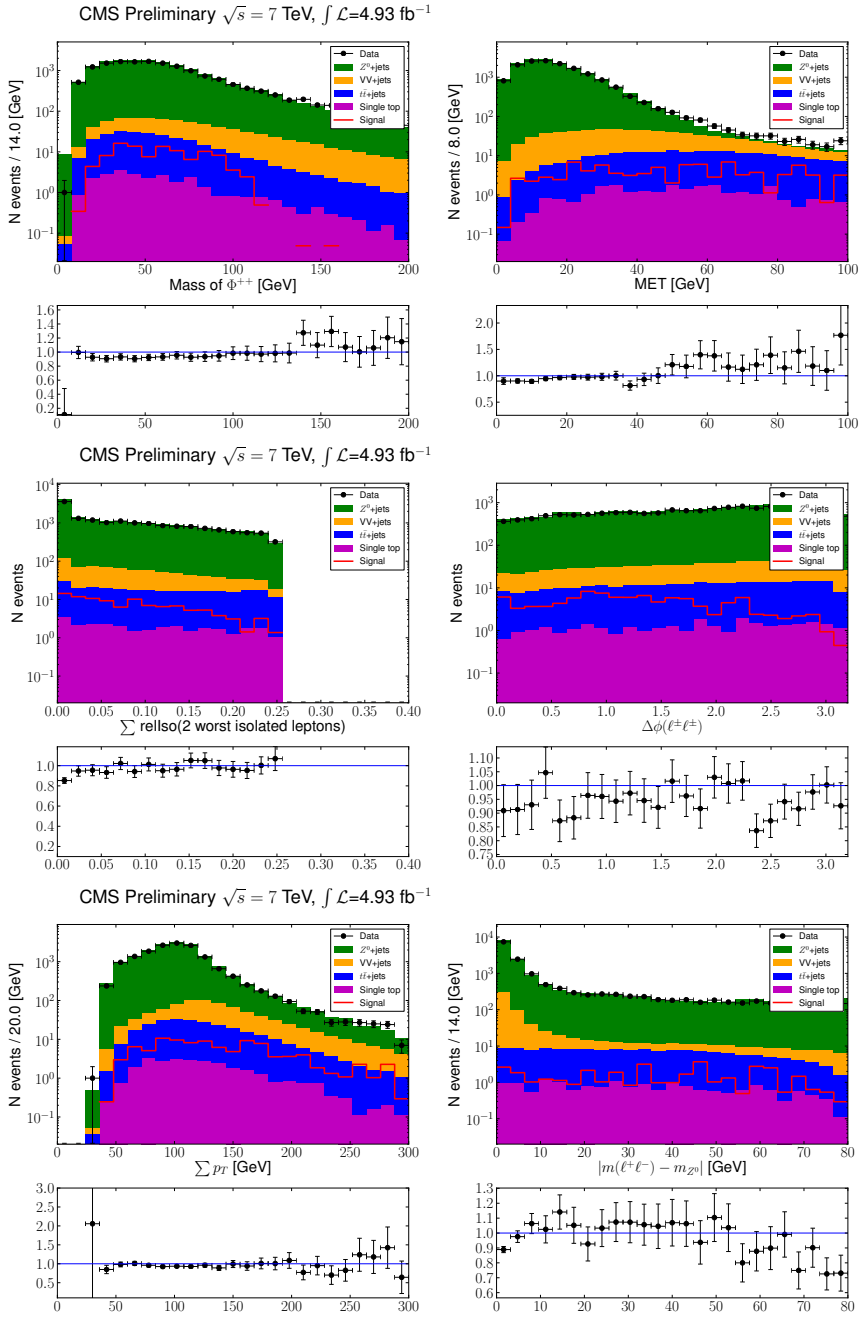

Figure 6.2: Distributions of the relevant observables for background contributions and signal at $m_{\Phi}^{\pm\pm} = 130$ GeV after the preselection requirements for 3-τ analysis.

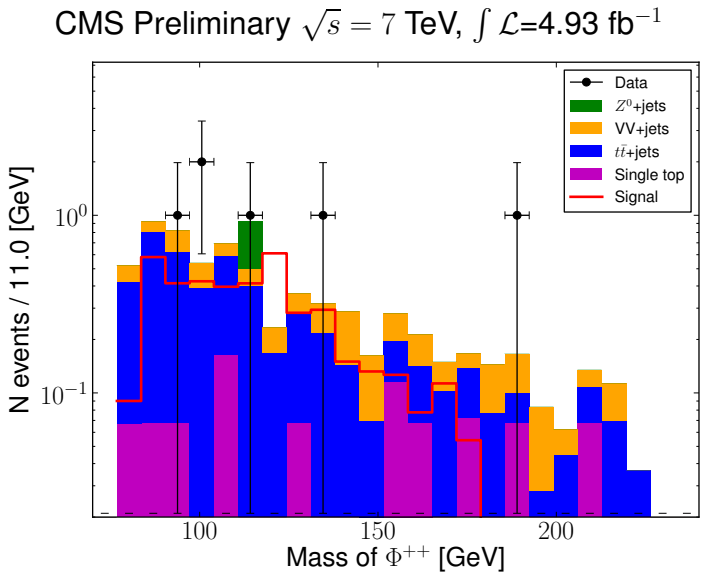

Figure 6.3: Di-lepton invariant mass distributions for background contributions and signal at $m_{\Phi}^{\pm\pm} = 200$ GeV after the final event selection.

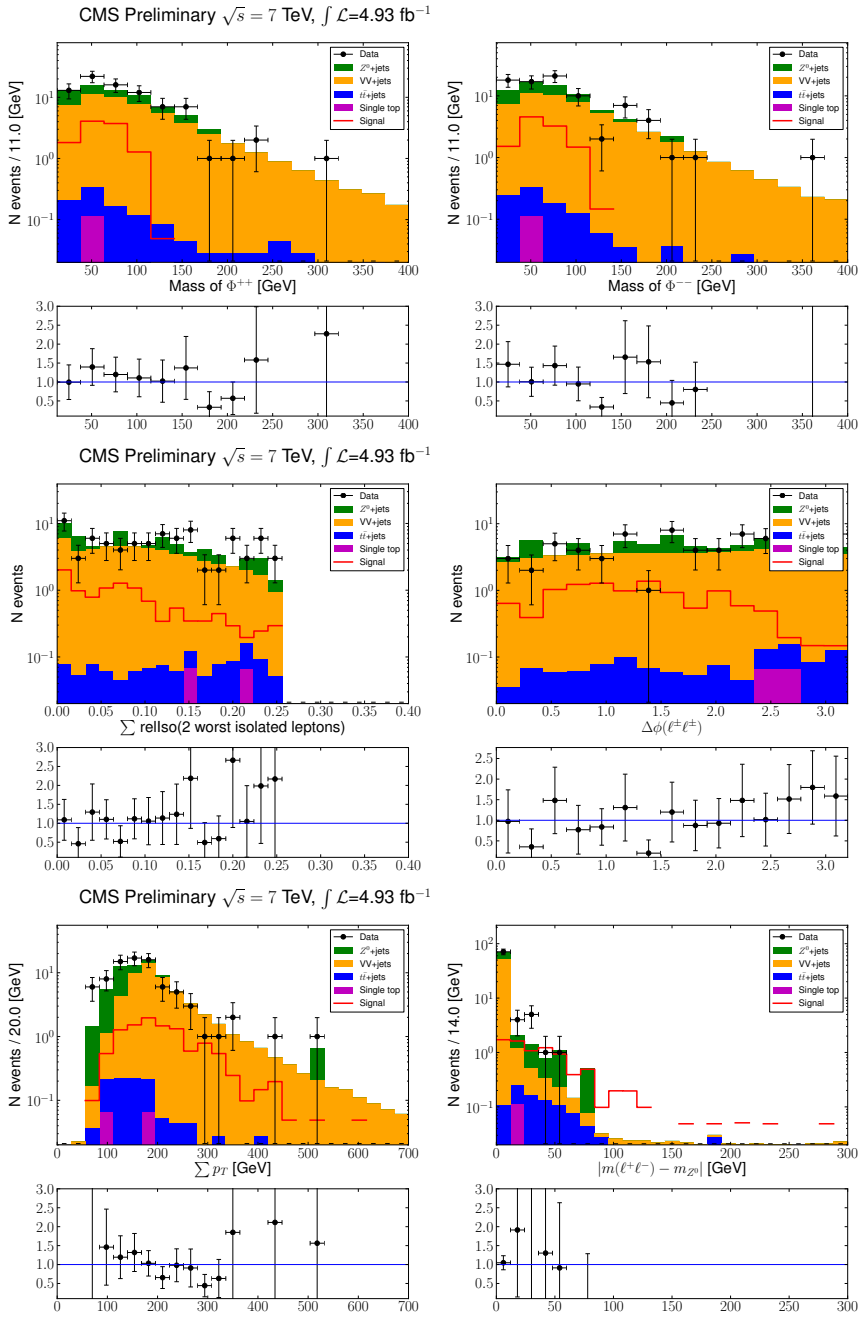

Figure 6.4: Distributions of the relevant observables for background contributions and signal at $m_{\Phi}^{\pm\pm} = 130$ GeV after the preselection requirements for 4-τ analysis.

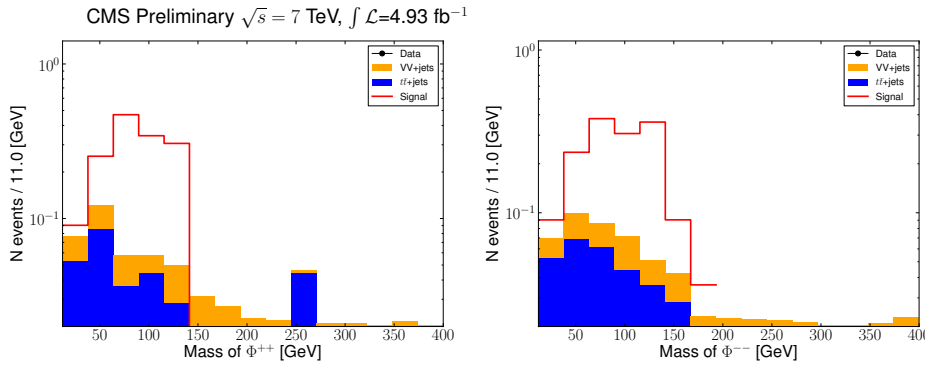

Figure 6.5: Di-lepton invariant mass distributions for signal at $m_{\Phi}^{\pm\pm} = 200$ GeV after the final event selection.

Table 6.1: Selections applied in three- and four-lepton final states

Variable	3 τ-leptons	4 τ-leptons
$\sum p_T$	$> m_{\Phi} - 10$ GeV or > 200 GeV	> 120 GeV
$\lvert m(\ell^+\ell^-) - m_{\mathrm{Z}} \rvert$	> 50 GeV	> 50 GeV
$\Delta\varphi$	< 2.1	< 2.5
E_T^{miss}	> 40 GeV	none
Mass window	$[m_{\Phi}/2 - 20$ GeV$; 1.1 \cdot m_{\Phi}]$	none

6.5 Background Estimation

6.5.1 ABCD method

For the 4τ analysis and 3τ analysis with mass hypothesis $m_{\Phi^{\pm\pm}} < 200$ GeV the "ABCD" background estimation method is used, which estimates the number of background events after the final event selection (signal region A) by extrapolating the event yields in three sidebands. The methodology of the ABCD method is described in detail in Section 4.5.2.

Two sets of variables are chosen considering their low correlation and available amount of data events in the sideband regions. The variables $\sum RelIso$ and $\lvert m(\ell^+\ell^-) - m_{\mathrm{Z}} \rvert$ for 3τ analysis and $\sum RelIso$ and $\sum p_T$ for 4τ analysis are used. It can be shown that both pairs of variables have low correlation, which is illustrated in Figure 6.6, that compares the distribution of the lepton isolation variable for both selection scenarios.

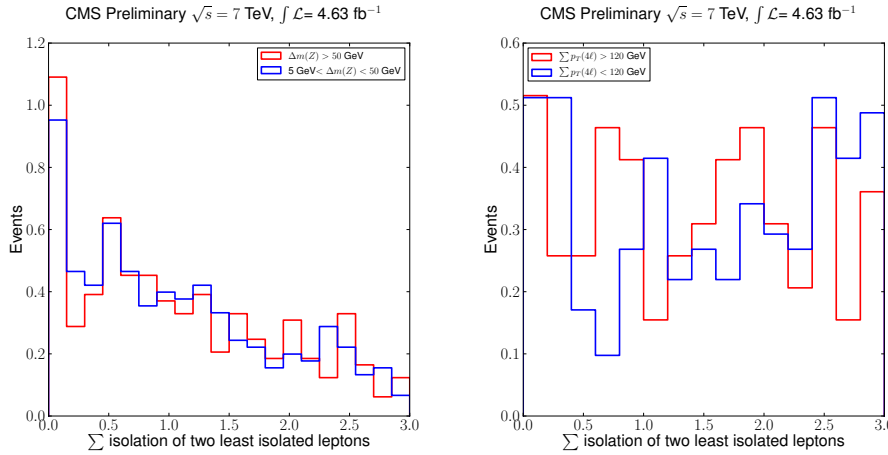

Figure 6.6: Normalized distributions of sum of relative lepton isolation for different cuts on $\Delta m(Z)$ for 3τ analysis (left) and for passed or fa iled $\sum p_T(4\ell)$ selection for 4τ analysis (right).

In order to extract the background contributions for 3τ final state for $\Phi^{\pm\pm}$ masses up to 200 GeV, the signal region and three background enriched sidebands are defined after applying all analysis cuts instead of the Z veto and lepton isolation:

- Signal region A: $\sum RelIso$ <0.25, $|m(\ell^+\ell^-) - m_{Z^0}| > 50$ GeV
- Region B: $\sum RelIso > 0.25$, $|m(\ell^+\ell^-) - m_{Z^0}| > 50$ GeV
- Region C: $\sum RelIso > 0.25$, 5GeV $< |m(\ell^+\ell^-) - m_{Z^0}| < 50$ GeV
- Region D: $\sum RelIso < 0.25$, 5 GeV< $|m(\ell^+\ell^-) - m_{Z^0}| < 50$ GeV

The number of data events in different regions (A,B,C,D) along with the background contribution predicted by the ABCD method (A-estimated) are summarized in Table 6.2. For $m_{\Phi}^{\pm\pm} > 200$ GeV the ABCD method is limited by the low statistics in the control regions and better results are obtained by the sideband method, described in Section 6.5.2.

Since 4τ final state analysis is mass independent, only one background estimate needs to be extracted. The final event selection has very low background contribution and it is challenging to define the sidebands with sufficient amount of available data events. The best result is obtained by combining the lepton isolation variable and $\sum p_T$ in four regions as follows:

- Signal region A: $\sum RelIso$ <0.25, $\sum p_T > 120$ GeV

$m_{\Phi}^{\pm\pm}$	region B	region C	region D	region A	A-estimated
130	47.0 ±6.8	187 ±14	193 ±14	37.0 ±6.1	48.5 ±8.7
150	24.0 ±4.9	102 ±10	104 ±10	21.0 ±4.6	24.4 ±6.1
170	13.0 ±3.6	48.0 ±6.9	52 ±7.2	12.0 ±3.5	14.1 ±4.8
200	8.0 ±2.8	21.0 ±4.6	24.0 ±4.9	6.0 ±2.4	9.1 ±4.2

Table 6.2: Number of events observed in signal region A and sidebands B, C and D and predicted number of background events in signal region A-estimated for 3τ analysis.

- Region B: $\sum RelIso > 0.25$, $\sum p_T > 120$ GeV
- Region C: $\sum RelIso > 0.25$, $\sum p_T < 120$ GeV
- Region D: $\sum RelIso < 0.25$, $\sum p_T < 120$ GeV.

The statistical uncertainties are sizable and the obtained background estimate is 0.15 ± 0.16, which agrees well with the Monte Carlo prediction.

6.5.2 Sideband Method

A sideband method is used to estimate the background contribution for 3τ analysis of $m_{\Phi^{\pm\pm}} > 200$ GeV. In this region the ABCD method is limited by the small statistics in the control regions. However, sideband method alone would not work for smaller $\Phi^{\pm\pm}$ masses or for 4τ analysis, due to the large mass window that comprises too large an area in the background region.

The sideband content is determined by using same-charge di-leptons with invariant mass in two regions: (12 Gev, $m_{\Phi^{\pm\pm}}/2 - 20$ GeV) and ($1.1 \cdot m_{\Phi^{\pm\pm}}$, 500 GeV). In the case of the 4τ analysis, the sidebands comprise the Φ^{++} and Φ^{--} two-dimensional mass plane in the same region. The upper bound is chosen due to the negligible expected yields for signal and background at higher masses, given the current integrated luminosity.

For each $\Phi^{\pm\pm}$ mass hypothesis the ratio of events in the signal region to the events in sidebands is estimated from the MC simulation by

$$\alpha = \frac{N_{SR}}{N_{SB}}, \tag{6.1}$$

where N_{SR} and N_{SB} are the event yields in the signal and sideband regions, respectively. Additional modifications are imposed to handle very low event counts:

- if $N_{SB} = 0$, then $\alpha = N_{SR}$ is assumed
- if N_{SR} is less than the statistical uncertainty, then the statistical uncertainty of the simulated samples is used as an estimate for the signal region.

When one observes $N_{\mathrm{SB}}^{\mathrm{Data}}$ in a sideband, the probability density function for the expected event rate can be described by a Gamma distribution with mean $(N_{\mathrm{SB}}^{\mathrm{Data}}+1)$ and dispersion $\sqrt{N_{\mathrm{SB}}^{\mathrm{Data}}+1}$ [83]. Therefore the predicted background rate in a signal region has a mean of

$$N_{\mathrm{BGSR}} = \alpha \cdot (N_{\mathrm{SB}}^{\mathrm{Data}}+1), \tag{6.2}$$

and a relative error of $1/\sqrt{N_{\mathrm{SB}}^{\mathrm{Data}}+1}$, where N_{BGSR} is the number of background events in the signal region estimated from data, $N_{\mathrm{SB}}^{\mathrm{Data}}$ is the total number of data events in the sidebands. If the background estimate in the signal region is less than the statistical uncertainty of the MC prediction, then it is assumed that the background estimate is equal to its statistical uncertainty.

6.6 Systematic Uncertainties

The impact on the selection efficiency of the uncertainties related to the electron and muon identification and isolation algorithms and the relevant mis-identification rates, detailed in [79, 78, 84, 85, 86], are studied using a standard "tag-and-probe" method that relies upon $\mathrm{Z} \to \ell^+\ell^-$ decays to provide an unbiased and high-purity sample of leptons. A "tag" lepton is required to satisfy stringent criteria on reconstruction, identification, and isolation, while a "probe" lepton is used to measure the efficiency of a particular selection by using the Z mass constraint. The ratio of the overall efficiencies as measured in data and simulated events is used as a correction factor for the efficiency determined through simulation, and is propagated to the final result.

The τ_{had} reconstruction and identification efficiency via the HPS algorithm is also derived from data and simulations, using the tag-and-probe method with $\mathrm{Z} \to \tau^+(\to \mu^+ + \bar{\nu}_\mu + \nu_\tau)\tau^-(\to \text{hadronic} + \nu_\tau)$ events [85]. The uncertainty of the measured efficiency of the τ algorithms is 6% [85]. Estimation of the τ energy-scale uncertainty is also performed with data in the $Z \to \tau\tau \to \mu + \tau_{\mathrm{had}}$ final state, and is found to be less than 3%. The τ_{had} charge misidentification rate is measured to be less than 3%.

The theoretical uncertainty in the signal cross section, which has been calculated to NLO, is about 10-15%, and arises because of its sensitivity to the QCD scale and parton distribution functions (PDF) [69].

The ratio α used to estimate the background contribution in the signal region is affected by two main uncertainties. The first is based on the uncertainty of the ratio of the simulated event yields in the sideband and the signal regions, and is related to the size of the kinematic region defined by the selection criteria. This uncertainty is dominated by the PDF and QCD scale sensitivity, in addition to the lepton energy scales. The combined uncertainty is 5% [87]. The other component comes from the statistical uncertainty due to the small event content of the sidebands. This uncertainty is as high as 100% if no events are observed in data. The luminosity uncertainty is estimated to be 2.2% [88].

The systematic uncertainties are summarized in Table 6.3. Correlations of systematic uncertainties within and between different decay modes are taken into account in the limit calculations.

Table 6.3: Source of systematic uncertainties and impact on the full selection efficiency

Lepton (e or μ) ID and isolation	2%
τ_{had} ID and isolation	6%
τ_{had} misidentification rate	3%
Trigger and primary vertex finding	1.5%
Signal cross section	10%
Luminosity (for signal only)	2.2%
Ratio used in background estimation	5-100%
Statistical uncertainty of observed data events in sideband	10-100%
Statistical uncertainty of signal samples	1-7%

6.7 Results

A CLs method [89] is used to calculate an upper limit for the $\Phi^{\pm\pm}$ cross section, assuming $\text{BR}(\Phi^{\pm\pm} \to \tau\tau) = 100\%$. The method includes the effect of systematic uncertainties summarized in Table 6.3. The limits are interpolated between the consecutive mass points linearly. The event yields after the final event selection are shown in Table 6.4.

No evidence for the existence of the $\Phi^{\pm\pm}$ decaying to τ-leptons has been found and a new cross section limit is set, which allows us to improve the previously published lower bound on the $\Phi^{\pm\pm}$ mass from 128 GeV [65] to 204 GeV as a combined result of associated and pair production. The new limit for pair production is 169 GeV. The results of the exclusion-limit calculations are reported in Figure 6.7.

Table 6.4: The number of background events estimated from MC and data, the number of events observed in data and expected signal yields for pair production and associated production.

Mass	Decay ch.	Background (MC)	Background (data)	Obs.	Pair-production	Asso. production
130 GeV	3τ	32.4 ± 0.95	48.5 ± 8.7	37	9.7 ± 1.1	13.0 ± 1.3
130 GeV	4τ	0.32 ± 0.45	0.15 ± 0.16	0	4.37 ± 0.46	0.0
150 GeV	3τ	22.1 ± 0.78	24.4 ± 6.1	21	6.55 ± 0.53	6.29 ± 0.95
150 GeV	4τ	0.32 ± 0.45	0.15 ± 0.16	0	2.87 ± 0.36	0.0
170 GeV	3τ	13.6 ± 0.73	14.1 ± 4.8	12	4.03 ± 0.39	4.70 ± 0.61
170 GeV	4τ	0.32 ± 0.45	0.15 ± 0.16	0	1.98 ± 0.27	0.08 ± 0.05
200 GeV	3τ	6.91 ± 0.53	9.1 ± 4.2	6	1.99 ± 0.19	2.21 ± 0.36
200 GeV	4τ	0.32 ± 0.45	0.15 ± 0.16	0	1.5 ± 0.16	0.0
225 GeV	3τ	4.71 ± 0.50	$4.38 \pm 0.46 \pm 0.04$	4	1.41 ± 0.13	1.82 ± 0.32
225 GeV	4τ	0.32 ± 0.45	0.15 ± 0.16	0	1.16 ± 0.12	0.0

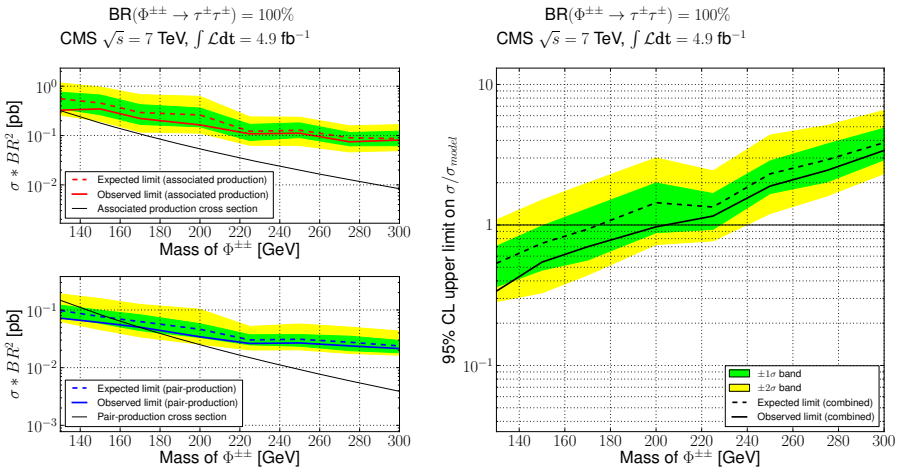

Figure 6.7: Lower bound on $\Phi^{\pm\pm}$ mass at 95% CL for 100% branching fraction to $\tau\tau$.

Appendix I

$W \to \tau\nu$ Final Event Selection Control Plots

The distribution of τ_{had} p_T, η, ϕ and of the transverse momentum of the highest p_T ("leading") charged hadron within the tau–jet in the sample of 793 $W \to \tau_{\text{had}}\nu$ candidate events passing the selection criteria described in section 4.4 are shown in Fig. 6.8. Fig. 6.9 presents the distributions of kinematic quantities reconstructed in the events. The $W \to \tau_{\text{had}}\nu$ signal is scaled according to the measured cross–section, EWK backgrounds according to the Monte Carlo expectation and QCD background to the yield determined from data. The expected shapes are taken from the Monte Carlo simulation, except for the QCD background, which is obtained from a control region in data, as described in section 4.5.

(a) (b)

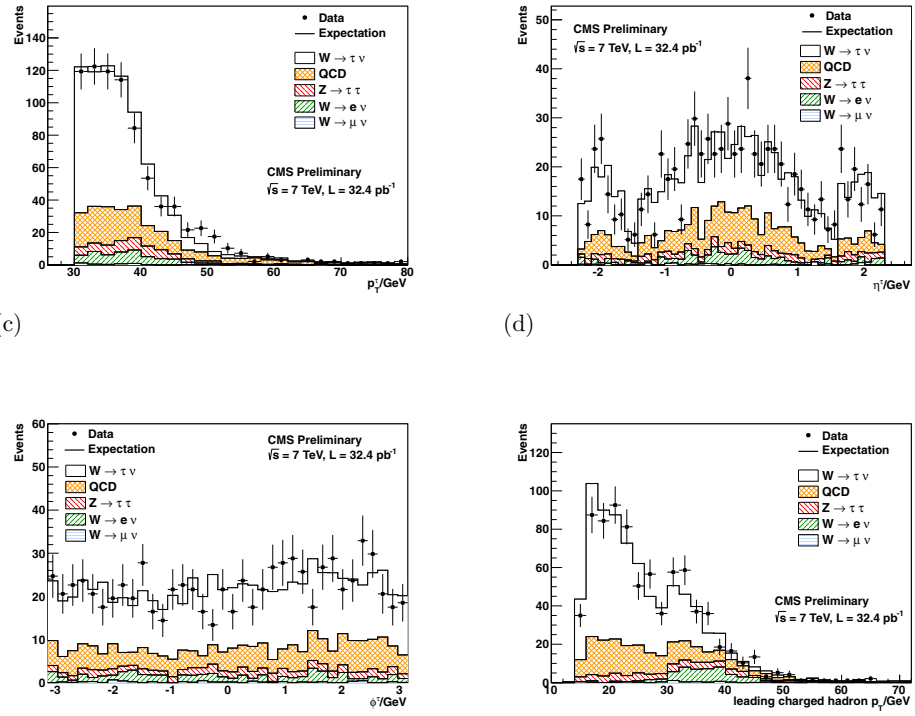

(c) (d)

Figure 6.8: Distributions of τ_{had} p_T (a), η (b), ϕ (c) and of the transverse momentum of the highest P_T ("leading") charged hadron within the tau–jet (d) in the sample $W \to \tau_{\text{had}}\nu$ candidate events compared to the expected sum of signal plus background processes.

(a) (b)

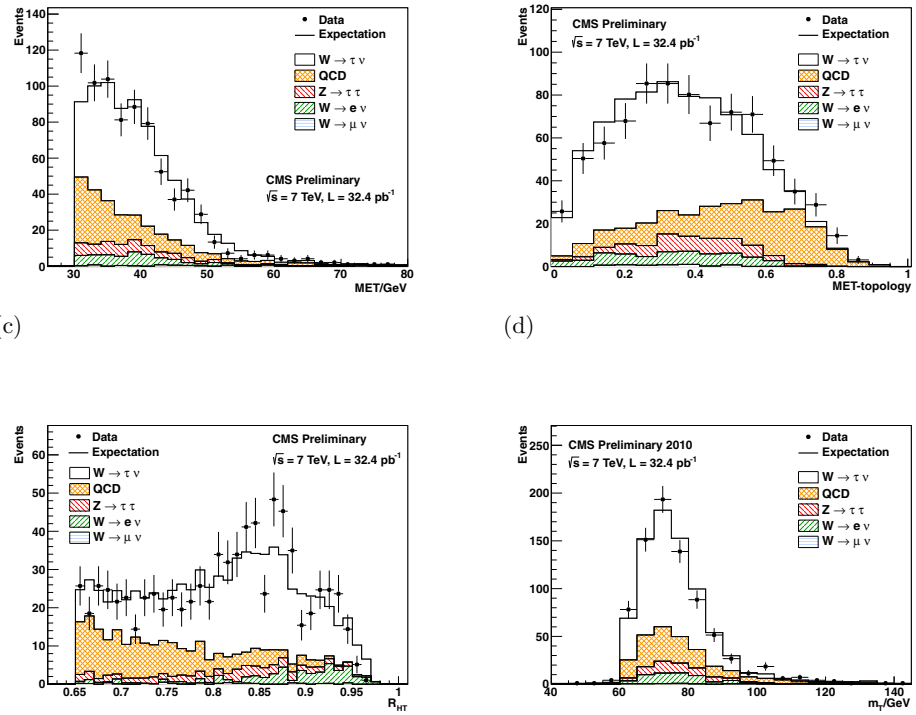

(c) (d)

Figure 6.9: Distributions of PF–E_T^{miss} (a), *MET-topology* (b) R_{HT} (c) and M_T (d) in the sample $W \to \tau_{\text{had}}\nu$ candidate events compared to the expected sum of signal plus background processes.

Chapter 7

Summary

This thesis is a summary of a set of publications, comprising $W \to \tau\nu$ cross section measurement and the search for a doubly charged Higgs boson that decays to τ-leptons. Both analyses are based on data collected by the CMS experiment at LHC. In addition, theoretical motivation for the existence of a doubly charged Higgs boson is given in the framework of the type II seesaw model and the connection between doubly charged Higgs boson leptonic branching fractions and neutrino parameters is established.

The study of $W \to \tau\nu$ is both a test of the standard model and a contribution to tau–physics studies at the LHC. A clear signal of $W \to \tau\nu$ candidate events is observed and the measured cross section is $\sigma(pp \to WX) \times \mathcal{B} = 8.96 \pm 0.51(\text{stat.})^{+2.32}_{-2.26}(\text{syst.}) \pm 0.36(\text{lumi.})$ pb. The ratio of $W^+ \to \tau^+\nu$ to $W^- \to \tau^-\nu$ cross–sections is measured to be $R_{+/-} = 1.55 \pm 0.19(\text{stat.})^{+0.11}_{-0.13}(\text{syst.})$. The results agree well with the theory predictions.

The search for a doubly charged scalar particle is motivated by the type II seesaw mechanism, that is one of the best studied frameworks for generating the small neutrino masses. The type II seesaw model is realized with an additional scalar field Φ that is a triplet under $SU(2)_L$ and carries $U(1)_Y$ hypercharge $Y = 2$. The doubly charged component of the scalar triplet $\Phi^{\pm\pm}$ can decay to same-sign lepton pairs, including lepton flavor violating combinations. The $\Phi^{\pm\pm}$ Yukawa coupling matrix is proportional to the light neutrino mass matrix, indicating that the measurement of the $\Phi^{\pm\pm}$ leptonic branching fractions would provide information about the neutrino parameters.

A search for a doubly charged Higgs boson decaying to τ-leptons is performed considering the final states with three or more isolated charged leptons or τ-jets. No excess is observed in comparison to the standard model prediction and an upper limit at the 95% confidence level is set on the $\Phi^{\pm\pm}$ production cross section assuming $\text{BR}(\Phi \to \tau\tau) = 100\%$. Lower bound on the $\Phi^{\pm\pm}$ mass is established at 204 GeV, providing a significantly more stringent constraint than the previously published limit.

The thesis starts with a short theoretical overview of the standard model and neutrino masses in Chapter 1. The LHC and the CMS experiment are described in Chapter 2. Chapter 3 gives an overview of computer simulations that are used for modeling high-energy particle collisions and explains the way physics objects are reconstructed from the raw output data of the detector. Chapter 4 summarizes the $W \to \tau\nu$ cross

section measurement. Chapter 5 and 6 cover the phenomenology of the type II seesaw mechanism and the search for a doubly charged Higgs boson, respectively.

Peatükk 8

Kokkuvõte

$W \to \tau\nu$ ristlõike mõõtmine ja τ-leptoniteks laguneva topeltlaetud Higgsi bosoni otsimine CMSi eksperimendis

Elementaarosakeste standardmudel on olnud erakordselt edukas ning on viimaste aastakümnete jooksul leidnud rohket eksperimentaalset kinnitust. Samas on põhjust arvata, et standardmudel ei ole fundamentaalne alus-teooria, vaid pigem jäänuk üldisemast füüsikast, mis avaldub kõrgematel energiatel.

Üheks kindlaks viiteks standardmudeli-järgse füüsika kohta on neutriinode nullist erinevad massid, mis on võrreldes teiste standardmudeli osakeste massidega väga väikesed. Neutriinode massi seletamiseks on loodud mitmeid teooriaid, millest üheks paremini motiveerituks on nn. kiigelauamehhanism: standardmudelile lisatakse juurde uued rasked osakesed, mille välja integreerimine annabki neutriinodele laetud leptonitega võrreldes oluliselt madalama massiskaala. Kiigelauamehhanismi on kolme tüüpi: I tüüp sisaldab raskeid paremakäelisi neutriinosid, II tüüp skalaarset tripletti ning III tüüp fermiontripletti. II tüüpi kiigelauamehhanism on eksperimentaalse kiirendi-füüsika seisukohast eriti huvitav, kuna skalaarse tripleti topeltlaetud komponent e. topeltlaetud Higgsi boson annab leptoniteks lagunedes väga selge eksperimentaalse signaali.

LHC on maailma suurim elementaarosakeste kiirendi, mis töötab kõrgemal energial kui ükski varasem eksperiment. Kiirendi paikneb 27 km pikkuses ringikujulises tunnelis, mis asub 100 m sügavusel maa all. Kiirenditoru koosneb magnetitest, milles ringlevad kaks vastassuunalist prooton-kiirt. Prootonid põrkuvad neljas interaktsioonipunktis, milles paiknevad osakeste-detektorid: ATLAS, CMS, LHCb ja ALICE. Neist ATLAS ja CMS on suured üldotstarbelised eksperimendid, milles saab uurida väga mitmesuguseid osakestefüüsika protsesse. LHCb on optimeeritud b-kvarkide füüsika uurimiseks ning ALICE raskete ioonide põrgeteks. Käesolevas doktoritöös käsitletud analüüsid põhinevad CMSi eksperimendi andmetel. LHC kiirendi üldisteks eesmärkideks on nii uue füüsika ja Higgsi bosoni otsimine kui ka standardmudeli protsesside uurimine ja

täppis-mõõtmised.

Käesoleva doktoritöö võib tinglikult jagada kolmeks osaks. Esimene osa võtab kokku esmaste CMSi eksperimendi andmete baasil teostatud τ-leptoniks ja neutriinoks laguneva W-bosoni ristlõike mõõtmise. Analüüsi käigus võrreldakse eksperimentaalsete andmete baasil rekonstrueeritud signaali teoorias standardmudeli poolt ennustatuga. Ühtlasi on tegemist olulise panusega τ-leptonite rekonstrueerimisega seotud füüsikast paremaks arusaamiseks CMSi eksperimendis. Järgnevalt on võetud kokku fenomenoloogiline uurimustöö topeltlaetud Higgsi bosoni võimalikest signatuuridest elementaarosakeste kiirendi eksperimentides ning topeltlaetud Higgsi bosoni lagunemiskanalite seosest neutriinoparameetritega. Eelnevale põhinedes on viidud läbi τ-leptoniteks laguneva topeltlaetud Higgsi bosoni otsing CMSi eksperimendi andmetest, mille eelduseks on nii hea arusaamine τ-leptonite identifitseerimisest kui ka läbi viidud fenomenoloogiline uurimustöö, mille tulemused muuhulgas rõhutavad topletlaetud Higgsi bosoni τ-leptoneid sisaldavate lagunemiskanalite olulisust.

τ-lepton on raskeim lepton ning tema eluiga on väga lühike. Seetõttu on osakestedetektoris võimalik näha ainult τ-leptoni lagunemisel tekkivaid kergemaid osakesi: elektroni, müüonit või hadronite kimpu, mis on tekkinud τ-leptoni lagunemisel u- ja d-kvarkideks. τ-leptoni lagunemisel tekkivad neutriinod ei jäta detektorisse mingit jälge ning nende olemasolu on võimalik kaudselt hinnata ainult osakeste põrke energiabilansist puuduoleva energia kaudu. Nendel põhjustel on protsesse, kus lõppolekus on τ-leptoneid, oluliselt keerulisem analüüsida kui protsesse kergete leptonitega, mis detektoris ei lagune. Samas on τ-leptonid oluliseks lagunemiskanaliks mitmete uue füüsika protsesside puhul, nagu Higgsi boson, supersümmeetria või lisadimensioonid. Standardmudeli protsessides tekivad τ-leptonid kõige sagedamini raskete vektorbosonite Z ja W lagunemisel.

W-boson on üks elektronõrki interaktsioone edasikandvatest rasketest kalibratsioonibosonitest, mis võib laguneda hadroniteks või laetud leptoniks ja neutriinoks. $W \to \tau\nu$ protsessi analüüs CMSi eksperimendi andmetega annab olulise panuse τ-leptoni füüsikast paremaks arusaamiseks. Teine tähtis standardmudeli protsess – Z bosoni lagunemine kaheks τ-leptoniks – annab küll lihtsamini rekonstrueeritava signaali, kuid selle protsessi toimumise tõenäosus on terve suurusjärgu võrra väiksem.

CMSi eksperimendi andmetes on nähtav selge $W \to \tau\nu$ protsessi signaal mõõdetud ristlõikega $\sigma(pp \to WX) \times \mathcal{B} = 8.96 \pm 0.51(\text{stat.})^{+2.32}_{-2.26}(\text{syst.}) \pm 0.36(\text{lumi.})$ pb. $W^+ \to \tau^+\nu$ ja $W^- \to \tau^-\nu$ mõõdetud ristlõigete suhe on $R_{+/-} = 1.55 \pm 0.19(\text{stat.})^{+0.11}_{-0.13}(\text{syst.})$. Tulemused ühtivad hästi standardmudeli poolt ennustatuga

Taudeks laguneva topeltlaetud Higgsi bosoni otsing põhineb kahel protsessil: $\Phi^{++}\Phi^{--} \to \tau^+\tau^+\tau^-\tau^-$ ja $\Phi^{++}\Phi^- \to \tau^+\tau^+\tau^-$. Analüüsi käigus rekonstrueeritakse kahe samamärgilise leptoni paarid, vaadeldes kolme või nelja leptoni lõppolekuid, millest vähemalt kaks peavad olema kerged leptonid (elektronid või müüonid). Analüüsitud eksperimentaalsed andmed on standardmudeliga kooskõlas ning analüüs annab topeltlaetud Higgsi bosoni massile uue alumise piiri, 204 GeV, mis parandab oluliselt eelmist Tevatroni kiirendis saadud tulemust.

Bibliography

[1] Chen-Ning Yang and Robert L. Mills. Conservation of isotopic spin and isotopic gauge invariance. *Phys. Rev.*, 96:191–195, 1954.

[2] Stephen L. Adler. Axial vector vertex in spinor electrodynamics. *Phys. Rev.*, 177:2426–2438, 1969.

[3] E. Fermi. An attempt of a theory of beta radiation. 1. *Z. Phys.*, 88:161–177, 1934.

[4] C.Š. Wu, E. Ambler, R. W. Hayward, D. D. Hoppes, and R. P. Hudson. Experimental Test of Parity Conservation in Beta Decay. *Phys. Rev.*, 105:1413–1414, 1957.

[5] E. C. G. Sudarshan and R. e. Marshak. Chirality invariance and the universal Fermi interaction. *Phys. Rev.*, 109:1860–1860, 1958.

[6] R. P. Feynman and Murray Gell-Mann. Theory of the Fermi interaction. *Phys. Rev.*, 109:193–198, 1958.

[7] S. L. Glashow. Partial Symmetries of Weak Interactions. *Nucl. Phys.*, 22:579–588, 1961.

[8] Abdus Salam. Weak and Electromagnetic Interactions. Originally printed in *Svartholm: Elementary Particle Theory, Proceedings Of The Nobel Symposium Held 1968 At Lerum, Sweden*, Stockholm 1968, 367-377.

[9] Steven Weinberg. A Model of Leptons. *Phys. Rev. Lett.*, 19:1264–1266, 1967.

[10] F. Englert and R. Brout. Broken symmetry and the mass of gauge vector mesons. *Phys. Rev. Lett.*, 13:321–323, 1964.

[11] G.Š. Guralnik, C. R. Hagen, and T. W. B. Kibble. Global conservation laws and massless particles. *Phys. Rev. Lett.*, 13:585–587, 1964.

[12] Peter W. Higgs. Broken symmetries and the masses of gauge bosons. *Phys. Rev. Lett.*, 13:508–509, 1964.

[13] Y. Ashie et al. A measurement of atmospheric neutrino oscillation parameters by Super-Kamiokande I. *Phys. Rev.*, D71:112005, 2005.

[14] E. Aliu et al. Evidence for muon neutrino oscillation in an accelerator-based experiment. *Phys. Rev. Lett.*, 94:081802, 2005.

[15] S. N. Ahmed et al. Measurement of the total active B-8 solar neutrino flux at the Sudbury Neutrino Observatory with enhanced neutral current sensitivity. *Phys. Rev. Lett.*, 92:181301, 2004.

[16] T. Araki et al. Measurement of neutrino oscillation with KamLAND: Evidence of spectral distortion. *Phys. Rev. Lett.*, 94:081801, 2005.

[17] K. Nakamura et al. Review of particle physics. *J. Phys.*, G37:075021, 2010.

[18] Ettore Majorana. Theory of the Symmetry of Electrons and Positrons. *Nuovo Cim.*, 14:171–184, 1937.

[19] LHC Project. http://lhc.web.cern.ch/lhc.

[20] CERN Web Communications. http://public.web.cern.ch.

[21] ALICE Collaboration. http://aliceinfo.cern.ch.

[22] ATLAS Collaboration. http://atlas.web.cern.ch/Atlas.

[23] CMS Collaboration. The CMS Experiment at the CERN LHC. *Journal of Instrumentation*, 3:S08004, 2008.

[24] LHCb Collaboration. http://lhcb.web.cern.ch/lhcb.

[25] LHCf Collaboration. The LHCf detector at the CERN LHC. *Journal of Instrumentation*, 3:S08006, 2008.

[26] TOTEM Collaboration. http://totem.web.cern.ch/Totem.

[27] P. Azzuri et al. Track Reconstruction Performance in CMS. *Technical Report*, CMS-CR-2008-110, 2008.

[28] LHC Experiments Committee. The CMS Electromagnetic Calorimeter project: Technical Design Report. *CMS Technical Design Report*, 1997.

[29] LHC Experiments Committee. The CMS Hadron Calorimeter Project: Technical Design Report. *CMS Technical Desing Report*, 1997.

[30] LHC Experiments Committee. The CMS Muon Project: Technical Design Report. *CMS Technical Desing Report*, 1997.

[31] S. Cittolin, A. Racz, and P.Šphicas. CMS Trigger and Data-aquisition Project:Technical Design Report. *CMS Technical Design Report*, 2002.

[32] T. Virdee, A. Petrilli, and A. Ball. CMS High Level Trigger. *Technical Report*, 2007.

[33] M.A. Dobbs et al. Les Houches Guidebook to Monte Carlo Generators for Hadron Collider Physics. 2004.

[34] P. Nason. A New Method for Combining NLO QCD with Shower Monte Carlo Algorithms. *JHEP*, 0411:040, 2004.

[35] M.L. Mangano, M. Monetti, F. Piccinini, et al. ALPGEN, a Generator for Hard Multiparton Processes in Hadronic Collisions. *JHEP*, 07:001, 2002.

[36] J. Alwall, P. Demin, S. Visscher, et al. MadGraph/MadEvent v4: The New Web Generation. *JHEP*, 09:028, 2007.

[37] B. Andersson, G. Gustafson, G. Ingelman, and T.Štjostrand. Parton Fragmentation and String Dynamics. *Physics Reports*, 97:31–145, 1983.

[38] S.Šjostrand, S. Mrenna, and P.Z. Skands. PYTHIA 6.4 Physics and Manual. *JHEP*, 05:026, 2006.

[39] Z. Was et al. TAUOLA the library for τ lepton decay. *Nucl.Phys.Proc.Suppl.*, 98:96, 2001.

[40] S. Agostinelli et al. GEANT4: A Simulation Toolkit. *Nucl. Instrum. Meth.*, A506:250–303, 2003.

[41] CMS Collaboration. CMS Tracking Performance Results From Early LHC Operation. *The European Physical Journal C - Particles and Fields*, 70:1165–1192, 2010.

[42] R. Fruehwirth, W. Wolfgang, and P. Vanlaer. Adaptive vertex fitting. *Technical Report*, CMS-NOTE-2007-008, 2007.

[43] S. Van der Meer. Calibration of the effective beam hegith in the ISR. *Internal CERN Report*, ISR-PO/68-31, 1968.

[44] Commissioning of the Particle-Flow reconstruction in Minimum-Bias and Jet Events from pp Collisions at 7 TeV. *CMS PAS*, PFT-10-002, 2010.

[45] Tau commissioning with 7 TeV data. *CMS PAS*, PFT-10-004, 2010.

[46] CMS Collaboration. Measurement of the inclusive Z cross section via decays to tau pairs in *pp* Collisions at $\sqrt{s} = 7$ TeV. *JHEP*, 1108:117, 2011.

[47] CMS Collaboration. CMS technical design report, volume II: Physics performance. *J. Phys.*, G34:995–1579, 2007.

[48] CMS Collaboration. Performance of tau reconstruction algorithms in 2010 data collected with CMS. *CMS PAS*, TAU-11-001, 2011.

[49] CMS Collaboration. Measurement of inclusive W and Z cross sections in pp collisions at $\sqrt{s} = 7$ TeV. *CMS PAS*, EWK-10-002, 2010.

[50] CMS Collaboration. Jet Energy Corrections determination at $\sqrt{s} = 7$ TeV. *CMS PAS*, JME-10-010, 2010.

[51] PDF4LHC Working Group. http://www.hep.ucl.ac.uk/pdf4lhc/PDF4LHCrecom.pdf.

[52] CMS Collaboration. Absolute luminosity normalization. *CMS DPS*, DPS-2011-002, 2011.

[53] CMS Collaboration. Measurement of inclusive W and Z cross sections in pp collisions at $\sqrt{s} = 7$ TeV. *JHEP*, 01:080, 2011.

[54] A.D. Martin, W.J. Stirling, R.S. Thorne, et al. Parton Distributions for the LHC. *Eur. Phys. J.*, C63:189–285, 2009.

[55] H.-L. Lai et al. New parton distributions for collider physics. *Phys. Rev.*, D82:074024, 2010.

[56] M. Magg and C. Wetterich. Neutrino Mass Problem and Gauge Hierarchy. *Phys. Lett.*, B94:61, 1980.

[57] J.Šchechter and J. W. F. Valle. Neutrino Masses in SU(2) x U(1) Theories. *Phys. Rev.*, D22:2227, 1980.

[58] Rabindra N. Mohapatra and Goran Senjanovic. Neutrino Masses and Mixings in Gauge Models with Spontaneous Parity Violation. *Phys. Rev.*, D23:165, 1981.

[59] G. B. Gelmini and M. Roncadelli. Left-Handed Neutrino Mass Scale and Spontaneously Broken Lepton Number. *Phys. Lett.*, B99:411, 1981.

[60] Ernest Ma, Martti Raidal, and Utpal Sarkar. Verifiable model of neutrino masses from large extra dimensions. *Phys. Rev. Lett.*, 85:3769–3772, 2000.

[61] P. F. Harrison, D. H. Perkins, and W. G. Scott. A redetermination of the neutrino mass-squared difference in tri-maximal mixing with terrestrial matter effects. *Phys. Lett.*, B458:79–92, 1999.

[62] F.P. An et al. Observation of electron-antineutrino disappearance at Daya Bay. 2012.

[63] J.K. Ahn et al. Observation of Reactor Electron Antineutrino Disappearance in the RENO Experiment. 2012.

[64] T. Aaltonen et al. Search for new physics in high p_T like-sign dilepton events at CDF II. *Phys.Rev.Lett.*, 107:181801, 2011.

[65] Victor Mukhamedovich Abazov et al. Search for doubly-charged Higgs boson pair production in ppbar collisions at sqrts = 1.96 TeV. *Phys. Rev. Lett.*, 108:021801, 2012.

[66] Georges Aad et al. Search for anomalous production of prompt like-sign muon pairs and constraints on physics beyond the Standard Model with the ATLAS detector. *Phys. Rev.*, D88:032004, 2012.

[67] A search for a doubly charged Higgs boson in pp collisions at $\sqrt{s} = 7$ TeV. *EPJ C*, (accepted for publication), 2012.

[68] K. Huitu, J. Maalampi, A. Pietila, and M. Raidal. Doubly charged Higgs at LHC. *Nucl. Phys.*, B487:27–42, 1997.

[69] Margarete Muhlleitner and Michael Spira. A note on doubly-charged Higgs pair production at hadron colliders. *Phys. Rev.*, D68:117701, 2003.

[70] A. G. Akeroyd, Cheng-Wei Chiang, and Naveen Gaur. Leptonic signatures of doubly charged Higgs boson production at the LHC. *JHEP*, 11:005, 2010.

[71] Torbjorn Sjostrand, Stephen Mrenna, and PeterŽ. Skands. PYTHIA 6.4 Physics and Manual. *JHEP*, 0605:026, 2006.

[72] S. Jadach, Z. Was, R. Decker, and Johann H. Kuhn. The tau decay library TAUOLA: Version 2.4. *Comput.Phys.Commun.*, 76:361–380, 1993.

[73] A. Pukhov. Calchep 2.3: MSSM, structure functions, event generation, 1, and generation of matrix elements for other packages. 2004.

[74] Johan Alwall, Pavel Demin, Simon de Visscher, Rikkert Frederix, Michel Herquet, et al. MadGraph/MadEvent v4: The New Web Generation. *JHEP*, 0709:028, 2007.

[75] Simone Alioli, Paolo Nason, Carlo Oleari, and Emanuele Re. NLO single-top production matched with shower in POWHEG: s- and t-channel contributions. *JHEP*, 0909:111, 2009.

[76] Paolo Nason. A New method for combining NLO QCD with shower Monte Carlo algorithms. *JHEP*, 0411:040, 2004.

[77] Stefano Frixione, Paolo Nason, and Carlo Oleari. Matching NLO QCD computations with Parton Shower simulations: the POWHEG method. *JHEP*, 0711:070, 2007.

[78] Performance of muon identification in pp collisions at $\sqrt{s} = 7$ TeV. *CMS PAS*, MUO-10-002, 2010.

[79] Electron reconstruction and identification at $\sqrt{s} = 7$ TeV. *CMS PAS*, EGM-10-004, 2010.

[80] Matteo Cacciari, Gavin P. Salam, and Gregory Soyez. The catchment area of jets. *JHEP*, 04:005, 2008.

[81] Matteo Cacciari and Gavin P. Salam. Pileup subtraction using jet areas. *Phys. Lett.*, B659:119–126, 2008.

[82] Tracking and primary vertex results in first 7 TeV collisions. *CMS PAS*, TRK-10-005, 2010.

[83] Robert D. Cousins, James T. Linnemann, and Jordan Tucker. Evaluation of three methods for calculating statistical significance when incorporating a systematic uncertainty into a test of the background-only hypothesis for a Poisson process. *Nucl. Instrum. Meth.*, A595:480–501, 2008.

[84] Serguei Chatrchyan et al. Search for neutral MSSM Higgs bosons decaying to tau pairs in pp Collisions at $\sqrt{s} = 7$ TeV. *Phys. Rev. Lett.*, 106:231801, 2011.

[85] S. Chatrchyan. Performance of tau-lepton reconstruction and identification in CMS. *JINST*, 7:P01001, 2012.

[86] S. Chatrchyan and others. Search for the standard model higgs boson in the decay channel h$\rightarrow$ zz$\rightarrow$ 4l in *pp* collisions at $\sqrt{s} = 7$ tev. *Phys. Rev. Lett.*, 108:111804, Mar 2012.

[87] Serguei Chatrchyan et al. Measurement of the Inclusive Z Cross Section via Decays to Tau Pairs in pp Collisions at $\sqrt{s} = 7$ TeV. *JHEP*, 08:117, 2011.

[88] CMS Collaboration. Absolute calibration of the luminosity measurement at cms: Winter 2012 update. CMS Physics Analysis Summary CMS-PAS-SMP-12-008, 2012.

[89] Alexander L. Read. Presentation of search results: The CL(s) technique. *J. Phys.*, G28:2693–2704, 2002.

Attached original publication

Curriculum Vitae

Address : Liis Rebane

Date of birth : 16.11.1981

Nationality : Estonian

Telephone : +372 5205737

e-mail : liis.rebane@cern.ch

Education

2006-2012 : Tartu University (physics), Ph.D. studies

2006 : Tallinn University of Technology (engineering physics), M.Sc.

2004 : Tallinn University of Technology (engineering physics), B.Sc.

2000 : Tallinna Reaalkool, secondary school

Employment

2006 - : National Institute of Chemical Physics and Biophysics, researcher

2005-2006 : Institute of Cybernetics at Tallinn University of Technology, engineer

Fields of research

Experimental particle physics, neutrino physics

Professional development

2008-2009: Particle physics Ph.D. lecture programme, SISSA, Trieste, Italy

06/2008: European School of High-Energy Physics, Herbeumont-sur-Semois, Belgium

07/2006-08/2006 : CERN summer student programme, Geneva

2005, 2006 : Studies and research at Institute of Photonic Sciences (ICFO) and Universitat Polytécnica de Catalunya, Barcelona

01/2004 : Winter school, Electromagnetic Fields and Their Effects (1 week), Chalmers University, Gothenburg

2002-2003 : Studies and research at University of Electro-Communications, Tokyo

Administrative responsibilities

2006 - : Member of the CMS experiment at LHC, CERN

2006-2010: Baltic Grid project

Teaching

09/2006-01/2007 : Calculus I (Tallinn University of Technology)

09/2006-01/2007 : Modern physics (Tallinn University of Technology)

Publications

1. CMS Collaboration. A search for a doubly charged Higgs boson in pp collisions at $\sqrt{s} = 7$ TeV. EPJ C (accepted for publication). arXiv:1207.2666 [hep-ex] (2012)

2. CMS Collaboration. Measurement of the $W \to \tau\nu$ cross-section in pp collisions at $\sqrt{s} = 7$ TeV. CMS Physics Analysis Summary EWK-11-019 (2011).

3. CMS Collaboration. Observation of $W \to \tau\nu$ production in pp collisions at $\sqrt{s} = 7$ TeV. CMS Physics Analysis Summary EWK-11-002 (2011).

4. Kadastik, M; Raidal, M; Rebane, L. Direct determination of neutrino mass parameters at future colliders. Physical Review D, 77, 115023 (2008)

5. Hektor, A.; Kadastik, M.; Müntel, M.; Raidal, M.; Rebane, L. Testing neutrino masses in little Higgs models via discovery of doubly charged Higgs at LHC. Nuclear Physics B, 787, 198 - 210 (2007)

6. Hektor, A. ; Kadastik, M.; Müntel, M.; Raidal, M. ; Rebane, L. Direct tests of neutrino masses in little Higgs models via discovery of doubly charged Higgs at LHC. CERN "Yellow" Reports, 124 - 126 (2007)

7. Hektor, A.; Kadastik, M.; Müntel, M.; Raidal, M.; Rebane, L. Low scale triplet Higgs neutrino mass scenarios in Little Higgs models. CERN "Yellow" Reports, 73 - 74 (2007)

8. Molina-Terriza, G.; Rebane, L.; Perez-Torres, J.; Torner, L.; Carrasco, S. Probing canonical geometrical objects by digital spiral imaging . Journal of the European Optical Society:Rapid publications, 2, 07014 (2007)

Elulookirjeldus

Nimi : Liis Rebane

Sünniaeg : 16.11.1981

Kodakondsus : eestlane

Telefoninumber : +372 5205737

e-post: liis.rebane@cern.ch

Haridus

2006-2012 : Tartu Ülikool (füüsika) doktorant

2006 : Tallinna Tehnikaülikool (tehniline füüsika), loodusteaduste magister

2004 : Tallinna Tehnikaülikool (tehniline füüsika), loodusteaduste bakalaureus

2000 : Tallinna Reaalkool, keskharidus

Teenistuskäik

2006 - : Keemilise ja Bioloogilise Füüsika Instituut, teadur

2005-2006 : Tallinna Tehnikaülikooli Küberneetika Instituut, tehnik

Teadustöö põhisuunad

Eksperimentaalne osakestefüüsika, neutriinofüüsika

Erialane enesetäiendus

2008-2009: Osakestefüüsika doktorantide loenguprogramm, SISSA, Trieste, Itaalia

06/2008: Suvekool, European School of High-Energy Physics, Herbeumont-sur-Semois, Belgia

07/2006-08/2006 : CERN-i suvetudnegite programm, Genf

2005, 2006 : Õpingud ja uurimustöö, ICFO teaduskeskus (Institut de Ciéncies Fotóniques) ja Universitat Polytécnica de Catalunya, Barcelona

01/2004 : Talvekursus, Electromagnetic Fields and Their Effects (kestvusega 1 nädal), Chalmersi ülikool, Göteborg

2002-2003 : Õpingud ja uurimustöö, University of Electro-Communications, Tokyo

Teadusorganisatsiooniline ja administratiivne tegevus

2006 - : Osalemine CMS eksperimendi töös

2006-2010 : Osalemine Baltic Gridi projektis

Õpetamine

09/2006-01/2007 : Matemaatiline analüüs I (Tallinna Tehnikaülikool)

09/2006-01/2007 : Kaasaegne füüsika (Tallinna Tehnikaülikool)

Publikatsioonid

1. CMS Collaboration. A search for a doubly charged Higgs boson in pp collisions at $\sqrt{s} = 7$ TeV. EPJ C (avaldamiseks vastuvõetud). arXiv:1207.2666 [hep-ex] (2012)

2. CMS Collaboration. Measurement of the $W \to \tau\nu$ cross-section in pp collisions at $\sqrt{s} = 7$ TeV. CMS Physics Analysis Summary EWK-11-019 (2011).

3. CMS Collaboration. Observation of $W \to \tau\nu$ production in pp collisions at $\sqrt{s} = 7$ TeV. CMS Physics Analysis Summary EWK-11-002 (2011).

4. Kadastik, M; Raidal, M; Rebane, L. Direct determination of neutrino mass parameters at future colliders. Physical Review D, 77, 115023 (2008)

5. Hektor, A.; Kadastik, M.; Müntel, M.; Raidal, M.; Rebane, L. Testing neutrino masses in little Higgs models via discovery of doubly charged Higgs at LHC. Nuclear Physics B, 787, 198 - 210 (2007)

6. Hektor, A.; Kadastik, M.; Müntel, M.; Raidal, M.; Rebane, L. Direct tests of neutrino masses in little Higgs models via discovery of doubly charged Higgs at LHC. CERN "Yellow" Reports, 124 - 126 (2007)

7. Hektor, A.; Kadastik, M.; Müntel, M.; Raidal, M.; Rebane, L. Low scale triplet Higgs neutrino mass scenarios in Little Higgs models. CERN "Yellow" Reports, 73 - 74 (2007)

8. Molina-Terriza, G.; Rebane, L.; Perez-Torres, J.; Torner, L.; Carrasco, S. Probing canonical geometrical objects by digital spiral imaging . Journal of the European Optical Society:Rapid publications, 2, 07014 (2007)

DISSERTATIONES PHYSICAE UNIVERSITATIS TARTUENSIS

1. **Andrus Ausmees.** XUV-induced electron emission and electron-phonon interaction in alkali halides. Tartu, 1991.
2. **Heiki Sõnajalg.** Shaping and recalling of light pulses by optical elements based on spectral hole burning. Tartu, 1991.
3. **Sergei Savihhin.** Ultrafast dynamics of F-centers and bound excitons from picosecond spectroscopy data. Tartu, 1991.
4. **Ergo Nõmmiste.** Leelishalogeniidide röntgenelektronemissioon kiiritamisel footonitega energiaga 70–140 eV. Tartu, 1991.
5. **Margus Rätsep.** Spectral gratings and their relaxation in some low-temperature impurity-doped glasses and chrystals. Tartu, 1991.
6. **Tõnu Pullerits.** Primary energy transfer in photosynthesis. Model calculations. Tartu, 1991.
7. **Olev Saks.** Attoampri diapasoonis voolude mõõtmise füüsikalised alused. Tartu, 1991.
8. **Andres Virro.** AlGaAsSb/GaSb heterostructure injection lasers. Tartu, 1991.
9. **Hans Korge.** Investigation of negative point discharge in pure nitrogen at atmospheric pressure. Tartu, 1992.
10. **Jüri Maksimov.** Nonlinear generation of laser VUV radiation for high-resolution spectroscopy. Tartu, 1992.
11. **Mark Aizengendler.** Photostimulated transformation of aggregate defects and spectral hole burning in a neutron-irradiated sapphire. Tartu, 1992.
12. **Hele Siimon.** Atomic layer molecular beam epitaxy of A^2B^6 compounds described on the basis of kinetic equations model. Tartu, 1992.
13. **Tõnu Reinot.** The kinetics of polariton luminescence, energy transfer and relaxation in anthracene. Tartu, 1992.
14. **Toomas Rõõm.** Paramagnetic H^{2-} and F^+ centers in CaO crystals: spectra, relaxation and recombination luminescence. Tallinn, 1993.
15. **Erko Jalviste.** Laser spectroscopy of some jet-cooled organic molecules. Tartu, 1993.
16. **Alvo Aabloo.** Studies of crystalline celluloses using potential energy calculations. Tartu, 1994.
17. **Peeter Paris.** Initiation of corona pulses. Tartu, 1994.
18. **Павел Рубин.** Локальные дефектные состояния в CuO_2 плоскостях высокотемпературных сверхпроводников. Тарту, 1994.
19. **Olavi Ollikainen.** Applications of persistent spectral hole burning in ultrafast optical neural networks, time-resolved spectroscopy and holographic interferometry. Tartu, 1996.
20. **Ülo Mets.** Methodological aspects of fluorescence correlation spectroscopy. Tartu, 1996.
21. **Mikhail Danilkin.** Interaction of intrinsic and impurity defects in CaS:Eu luminophors. Tartu, 1997.

22. **Ирина Кудрявцева.** Создание и стабилизация дефектов в кристаллах KBr, KCl, RbCl при облучении ВУФ-радиацией. Тарту, 1997.
23. **Andres Osvet.** Photochromic properties of radiation-induced defects in diamond. Tartu, 1998.
24. **Jüri Örd.** Classical and quantum aspects of geodesic multiplication. Tartu, 1998.
25. **Priit Sarv.** High resolution solid-state NMR studies of zeolites. Tartu, 1998.
26. **Сергей Долгов.** Электронные возбуждения и дефектообразование в некоторых оксидах металлов. Тарту, 1998.
27. **Kaupo Kukli.** Atomic layer deposition of artificially structured dielectric materials. Tartu, 1999.
28. **Ivo Heinmaa.** Nuclear resonance studies of local structure in $RBa_2Cu_3O_{6+x}$ compounds. Tartu, 1999.
29. **Aleksander Shelkan.** Hole states in CuO_2 planes of high temperature superconducting materials. Tartu, 1999.
30. **Dmitri Nevedrov.** Nonlinear effects in quantum lattices. Tartu, 1999.
31. **Rein Ruus.** Collapse of 3d (4f) orbitals in 2p (3d) excited configurations and its effect on the x-ray and electron spectra. Tartu, 1999.
32. **Valter Zazubovich.** Local relaxation in incommensurate and glassy solids studied by Spectral Hole Burning. Tartu, 1999.
33. **Indrek Reimand.** Picosecond dynamics of optical excitations in GaAs and other excitonic systems. Tartu, 2000.
34. **Vladimir Babin.** Spectroscopy of exciton states in some halide macro- and nanocrystals. Tartu, 2001.
35. **Toomas Plank.** Positive corona at combined DC and AC voltage. Tartu, 2001.
36. **Kristjan Leiger.** Pressure-induced effects in inhomogeneous spectra of doped solids. Tartu, 2002.
37. **Helle Kaasik.** Nonperturbative theory of multiphonon vibrational relaxation and nonradiative transitions. Tartu, 2002.
38. **Tõnu Laas.** Propagation of waves in curved spacetimes. Tartu, 2002.
39. **Rünno Lõhmus.** Application of novel hybrid methods in SPM studies of nanostructural materials. Tartu, 2002.
40. **Kaido Reivelt.** Optical implementation of propagation-invariant pulsed free-space wave fields. Tartu, 2003.
41. **Heiki Kasemägi.** The effect of nanoparticle additives on lithium-ion mobility in a polymer electrolyte. Tartu, 2003.
42. **Villu Repän.** Low current mode of negative corona. Tartu, 2004.
43. **Алексей Котлов.** Оксианионные диэлектрические кристаллы: зонная структура и электронные возбуждения. Tartu, 2004.
44. **Jaak Talts.** Continuous non-invasive blood pressure measurement: comparative and methodological studies of the differential servo-oscillometric method. Tartu, 2004.
45. **Margus Saal.** Studies of pre-big bang and braneworld cosmology. Tartu, 2004.

46. **Eduard Gerškevitš.** Dose to bone marrow and leukaemia risk in external beam radiotherapy of prostate cancer. Tartu, 2005.
47. **Sergey Shchemelyov.** Sum-frequency generation and multiphoton ionization in xenon under excitation by conical laser beams. Tartu, 2006.
48. **Valter Kiisk.** Optical investigation of metal-oxide thin films. Tartu, 2006.
49. **Jaan Aarik.** Atomic layer deposition of titanium, zirconium and hafnium dioxides: growth mechanisms and properties of thin films. Tartu, 2007.
50. **Astrid Rekker.** Colored-noise-controlled anomalous transport and phase transitions in complex systems. Tartu, 2007.
51. **Andres Punning.** Electromechanical characterization of ionic polymer-metal composite sensing actuators. Tartu, 2007.
52. **Indrek Jõgi.** Conduction mechanisms in thin atomic layer deposited films containing TiO_2. Tartu, 2007.
53. **Aleksei Krasnikov.** Luminescence and defects creation processes in lead tungstate crystals. Tartu, 2007.
54. **Küllike Rägo.** Superconducting properties of MgB_2 in a scenario with intra- and interband pairing channels. Tartu, 2008.
55. **Els Heinsalu.** Normal and anomalously slow diffusion under external fields. Tartu, 2008.
56. **Kuno Kooser.** Soft x-ray induced radiative and nonradiative core-hole decay processes in thin films and solids. Tartu, 2008.
57. **Vadim Boltrushko.** Theory of vibronic transitions with strong nonlinear vibronic interaction in solids. Tartu, 2008.
58. **Andi Hektor.** Neutrino Physics beyond the Standard Model. Tartu, 2008.
59. **Raavo Josepson.** Photoinduced field-assisted electron emission into gases. Tartu, 2008.
60. **Martti Pärs.** Study of spontaneous and photoinduced processes in molecular solids using high-resolution optical spectroscopy. Tartu, 2008.
61. **Kristjan Kannike.** Implications of neutrino masses. Tartu, 2008.
62. **Vigen Issahhanjan.** Hole and interstitial centres in radiation-resistant MgO single crystals. Tartu, 2008.
63. **Veera Krasnenko.** Computational modeling of fluorescent proteins. Tartu, 2008.
64. **Mait Müntel.** Detection of doubly charged higgs boson in the CMS detector. Tartu, 2008.
65. **Kalle Kepler.** Optimisation of patient doses and image quality in diagnostic radiology. Tartu, 2009.
66. **Jüri Raud.** Study of negative glow and positive column regions of capillary HF discharge. Tartu, 2009.
67. **Sven Lange.** Spectroscopic and phase-stabilisation properties of pure and rare-earth ions activated ZrO_2 and HfO_2. Tartu, 2010.
68. **Aarne Kasikov.** Optical characterization of inhomogeneous thin films. Tartu, 2010.

69. **Heli Valtna-Lukner.** Superluminally propagating localized optical pulses. Tartu, 2010.
70. **Artjom Vargunin.** Stochastic and deterministic features of ordering in the systems with a phase transition. Tartu, 2010.
71. **Hannes Liivat.** Probing new physics in e+e− annihilations into heavy particles via spin orientation effects. Tartu, 2010.
72. **Tanel Mullari.** On the second order relativistic deviation equation and its applications. Tartu, 2010.
73. **Aleksandr Lissovski.** Pulsed high-pressure discharge in argon: spectroscopic diagnostics, modeling and development. Tartu, 2010.
74. **Aile Tamm.** Atomic layer deposition of high-permittivity insulators from cyclopentadienyl-based precursors. Tartu, 2010.
75. **Janek Uin.** Electrical separation for generating standard aerosols in a wide particle size range. Tartu, 2011.
76. **Svetlana Ganina.** Hajusandmetega ülesanded kui üks võimalus füüsikaõppe efektiivsuse tõstmiseks. Tartu, 2011
77. **Joel Kuusk.** Measurement of top-of-canopy spectral reflectance of forests for developing vegetation radiative transfer models. Tartu, 2011.
78. **Raul Rammula**. Atomic layer deposition of HfO_2 – nucleation, growth and structure development of thin films. Tartu, 2011.
79. **Сергей Наконечный.** Исследование электронно-дырочных и интерстициал-вакансионных процессов в монокристаллах MgO и LiF методами термоактивационной спектроскопии. Тарту, 2011.
80. **Niina Voropajeva.** Elementary excitations near the boundary of a strongly correlated crystal. Tartu, 2011.
81. **Martin Timusk.** Development and characterization of hybrid electro-optical materials. Tartu, 2012, 106 p.
82. **Merle Lust.** Assessment of dose components to Estonian population. Tartu, 2012, 84 p.
83. **Karl Kruusamäe.** Deformation-dependent electrode impedance of ionic electromechanically active polymers. Tartu, 2012, 128 p.